Structures cohérentes dans des écoulements turbulents

Quentin Chevalier

INSTITUT POLYTECHNIQUE DE PARIS

NNT : 2023IPPAX157

Thèse de doctorat

ÉCOLE POLYTECHNIQUE

IP PARIS

Coherent structures in turbulent flows

Thèse de doctorat de l'Institut Polytechnique de Paris
préparée à l'École polytechnique

École doctorale n°626, Ecole doctorale de l'Institut Polytechnique de Paris (IPP)

Spécialité : Ingénieurie, Mécanique et Energie

Thèse soutenue à Palaiseau, le 30 Novembre 2023, par

QUENTIN CHEVALIER

Jury :

Yongyun Hwang *Imperial College* (Department of Aeronautics)	Rapporteur
Frédéric Alizard *École Centrale de Lyon* (Laboratoire de Mécanique des Fluides et d'Acoustique)	Rapporteur
Jean-Christophe Robinet *Arts et Métiers ParisTech* (DYNFLUID)	Président
Stefania Cherubini *Politecnico do Bari* (Macchine a fluido)	Examinateur
Lutz Lesshafft *École polytechnique* (LadHyX)	Directeur de thèse
Vincent Plana *Direction Générale de l'Armement* (Essai Propulseurs)	Invité

Acknowledgements

This thesis is my work and that of Lutz Lesshafft, my advisor. For all his commitment to my thesis, he clearly deserves the first round of applause. Difficult to imagine a more perfect match for me, or to give him too little credit for his immense contribution to all positive aspects of my PhD. Otherworldly rigorous and professional, he looked out for me at every turn, yet always took care to let me grow and think on my own. Crucially, he has a great ability to forgive, even when I barged through his counsel to make my own mistakes. Dedicated head of the lab, his oratory skills made even lab general assemblies entertaining. Lutz was alternatively wise sage, witty reviewer and German shepherd when I needed him to be. Not afraid to contradict himself, always there to lend a hand, he took in a boy - or worse, a boy persuaded to be more than a boy - and made him something of a scientist.

My thesis took a U-turn with the arrival of Christopher Douglas in the team. Ever available, always constructive even when confronted with the worst science tainted with bad faith, he pretty much carried me on by sheer example. I could not have achieved what I did manage to achieve and cross the PhD desert were it not for his help and keen advice. Unbelievably knowledgeable when it comes to papers, we quickly developed a working relationship where he pointed to publications and I recommended films. He was an excellent office pal I am honoured to call a friend, and I wish for every PhD student out there to have such an incredible post-doc - soon to be tenured professor - in his or her team.

I had the pleasure of being office mate with Chuhan Wang for the beginning of my PhD. In fact, I carried the torch of his previous code to the best of my ability. Chuhan was a helpful friend that I'm glad to have shared a desk with. Ever in high spirits even when confronted to catastrophe, he had an uncanny ability to extend his hand and connect with people that I very much envy.

Johann Moulin from *ONERA* was another uplifting figure throughout my PhD. I feel like I bonded incredibly fast with this upbeat scientist, so much so that we often communicated in half-sentences, which made group meetings all the more confusing for anyone else involved and entertaining for us. It was very refreshing to meet another young engineer turned researcher on the same wavelength as me, which made for very close perspectives on a number of issues.

As part of Lutz's team, I came into contact with Herman Mak as he was starting his thesis and I was squarely in the middle of mine. I strived to help him as much as others had helped me. Getting to share experience and technical know-how also helped me grow in a way, not to mention he brought to the table a different perspective to problems and creative solutions. He's a dedicated PhD student who did not hesitate to call out my mistakes, which is the best kind of collaborator to wish for.

The most recent addition to the team at the time of writing is Antoine Jouin. So recent an addition in fact, that we had but a few months to interact with one another. The loss is mine. Constructive, *débrouillard* and very creative, my code is in good hands with him.

André Cavalieri was my closest collaborator from aboard. I remember fondly him explaining painstakingly to me over the course of several emails fundamentals that I was pestering him about at the start of my thesis. Patient and very pedagogical, he was also very approachable and a valued contributor to all of my work.

As is typical of my generation, the moment I encountered a difficulty with my code I went and looked it up online. I found Jørgen Schartum Dokken, a pillar of the `FEniCsX` library that I used daily. I am very grateful for his time and patience, not to mention his quality tutorials or very detailed answers to the most mundane questions. Many of the snippets he provided ended up in my code.

Over the course of my PhD I had the chance to interact with many researchers at *LadHyX*, sometimes about science but mostly about anything but. Blaise Delmotte who treated us to excellent seminars and was always present for an early lunch, Camille Duprat who used to race to her office and back in order not to make us wait when we would leave, Sébastien Michelin more often than not at the pool, Paul Billant and his critical insight on swirling flows, Jean-Marc Chomaz who has his very own approach to science, Christophe Clanet and his incredible sense of both formality and humour mingled together, Etienne Jambon-Puillet that I would have all to myself when I went to fetch him at noon, Christophe Josserand who was never short of sharp institutional insights, Gabriel Amselem and his ever-present smile, Sophie Ramananarivo ringing her characteristic laugh, Marie-Jean Thoraval who quickly picked up non-verbal communication with me. Let's not forget Avin Babataheri and her disturbing talent for judging character.

Of course, the people doing the most actual work in any lab at any given time are usually not tenured researchers, and *LadHyX* is no exception in that regard. Over the years, I got to know Tom Marzin

and his ravaging sense of humour, Pierre-Antoine Maes who put as much dedication into his work as he did into holding the junior staff of the lab together, Prathmesh Vinze with whom I share a vested interest in geopolitics, Ursy Makanga, one of the most driven person I've met so far, Antoine Tatin and his fondness for barbecues, Agathe Schmider whose most agreeable ringtone made my day every time, Olivier Marchand, a man with style, vision and talent, Mathilde Tavares with whom I would go to the pool as often as possible, Pierre Van de Welde who was simply nice beyond belief, Francesco Picella the most over-the-top Italian imaginable, Rishabh Nain the fluet French-speaker, Enrico Lorenzetti, the nicest person to share a server with, Aude Sagnimorte and Hassan Madkour, quality lab representatives if there ever were any, Samy Lakhal, albeit somewhat briefly. I was even entreated to share the company of Rodolphe Grivet and Alice Boillet once more, only to be awed a second time at their strength of character.

Many thanks to all the lab staff who make all the difference between a lab powering through like a well-oiled machine or a gripping, ageing mechanism that simply refuses to budge. I have mostly interacted with Sandrine Laguerre and Daniel Guy who also played their part in converting enthusiasm and time into scientific results over the years.

A special salute to all my friends, especially the *faëriX* band. The Second Tower was a great place to have barbecues and unending board game nights, not to mention the great times we had campaigning together. So many of you are doing PhDs themselves it should come as no surprise that you turned out to be dependable pals across the experience, in times of chill or duress alike.

I have especially been given the chance to share a flat during my whole PhD with the most incredible room-mates, Geoffrey Magda and Martin Guillot, two of my closest friends. It was a great chance to come home for three years to comrades of the finest sort. Our time together has bonded us greatly, and it is now strange for me to imagine living alone bereft of Geoffrey's ever-ringing laugh or Martin's delicious cooking.

To be fair, there were more than three room-mates in the flat. My cat Katioucha graciously leased me her bed or chair from time to time, and graced me with no shortage of purrs every time I put my paws on her. She was a great stress relief and companion before, during and after confinement.

Of all the thanks I have to give, my parents Thierry and Hélène deserve more than a few. They raised me like few people ever have the chance, with kindness, goodwill, and love. Without them I would not be of this world, and without their guidance I would have had a hard time even writing these lines in a second language. They have always supported me in my craziest endeavours and played a role in every step of the realisation of any of my dreams. Their hard work put me on the track that I still follow today, and I certainly hope to make them proud.

A flourish is also due to my beloved little sister Laure, who had an important role in keeping my ego in check throughout my existence, and helped me grow up as slightly less of an insufferable brat. I'm glad and honoured to be her bro. All my wishes of courage to her, as I hope to read similar lines in her own manuscript soon.

It took growing up to realise how much of an amazing family I was born in. I don't want to leave anyone out, so let it be known that my aunt and uncle are great, and my cousins wonderful people. Especially the favourite one. My grandmothers are all awesome forces of nature. I have the privilege of having an extended family that is supportive and enterprising. This is not something to be ever taken for granted, as my grandfathers' passing sourly reminded me. A heartfelt blessing to all of you.

This section wouldn't be complete without Marie Wybrecht, whom I met at the very end of my PhD and changed my life forever. Your smile and kindness are always something to look forward to, no matter how often you grace me with them. You were very accommodating with the constraints that came with dating a PhD student in his final run, and I hope to get the chance to make that up to you for the rest of our lives.

List of acronyms

CFD	Computational Fluid Dynamics
NSE	Navier-Stokes Equations
DNS	Direct Numerical Simulations
LES	Large Eddy Simulations
RANS	Reynolds-Averaged Navier-Stokes
RSM	Reynolds Stress Model
ROM	Reduced Order Modelling
LTSA	Local Temporal Stability Analysis
LSSA	Local Spatial Stability Analysis
LSTSA	Local Spatio-Temporal Stability Analysis
GTSA	Global Temporal Stability Analysis
SVD	Singular Value Decomposition
SPOD	Spectral Proper Orthogonal Decomposition
OSS	Orr-Sommerfield-Squire
ECS	Exact Coherent States
SA	Spalart-Allmaras
KH	Kelvin Helmholtz
LU	Lift-up
C	Centrifugal
YAJ	Yet Another Jet code
`SPY`	Swirling Parallel Yaj
`SPYB`	`SPY` Baseflow
`SPYP`	`SPY` Perturbations
PhD	Philosophiae Doctor

List of symbols

i	Complex number $i^2 = -1$
δ_i^j	Kronicker delta, 1 if $i = j$, 0 else
$\Re$	Real part
$\Im$	Imaginary part
$\mathbb{C}$	Space of complex numbers
$\mathbb{R}$	Space of real numbers
$\mathbb{R}^+$	Space of real positive numbers
$\mathbb{N}$	Space of positive integers
$\underline{\cdot}$	Vector
$\underline{\underline{\cdot}}$	Tensor
$\underline{e}_i$	Unit vector in direction i
$\cdot^T$	Transpose
$\cdot^H$	Hermitian
$\cdot^*$	Complex conjugate
$\lvert\cdot\rvert$	Module $\lvert x\rvert = \sqrt{xx^*}$
∂_i	Partial derivative with respect to i
$\cdot\rvert_a$	Quantity evaluated at fixed a
$\underline{\nabla}\cdot$	Divergence $[\nabla \cdot A]_i = \partial_j A_{ij}$
$\underline{\nabla(\cdot)}$	Gradient $[\nabla f]_i = \partial_i f$
$\underline{\underline{\nabla(\cdot)}}$	Jacobian $[\nabla Q]_{ij} = \partial_j Q_i$
$\underline{\nabla} \times \underline{\cdot}$	Rotational
Δ	Laplacian - divergent of gradient
$\overline{\cdot}$	Ensemble average
$\mathtt{q}$	Total dimensionless quantity $\mathtt{q} = Q + q$
$\underline{\mathtt{q}}$	Total dimensionless state vector $\underline{\mathtt{q}} = \left[\underline{\mathtt{u}}^T \ \mathtt{p}\right]^T$
$\underline{\mathtt{u}}$	Total dimensionless velocity $\underline{\mathtt{u}} = \underline{U} + \underline{u}$
$\mathtt{p}$	Total dimensionless pressure $\mathtt{p} = P + p$
Q	Ensemble-averaged dimensionless quantity $Q = \overline{\mathtt{q}}$
$\underline{Q}$	Ensemble-averaged dimensionless state vector $\underline{Q} = \left[\underline{U}^T \ P\right]^T$
$\underline{U}$	Ensemble-averaged dimensionless velocity $\underline{U} = \overline{\underline{\mathtt{u}}}$
P	Ensemble-averaged dimensionless pressure $P = \overline{\mathtt{p}}$
q	Fluctuations dimensionless quantity $\overline{q} = 0$
$\underline{q}$	Fluctuations dimensionless state vector $\underline{q} = \left[\underline{u}^T \ p\right]^T$
$\underline{u}$	Fluctuations dimensionless velocity $\overline{\underline{u}} = \underline{0}$
p	Fluctuations dimensionless pressure $\overline{p} = 0$
$\underline{\underline{\tau}}$	Correlation tensor $\underline{\underline{\tau}} = \underline{u}\underline{u}^T$
L	Domain scale (with dimensions)
ν_0	Molecular viscosity (with dimensions)
ν_t	Turbulent eddy-viscosity (dimensionless)
Ma	Mach number, $Ma = \max \lVert\underline{U}\rVert / c$, ratio of maximum speed over sound speed
Re	Reynolds number, $Re = UL/\nu_0$, ratio of inertial over viscous forces
Re_τ	Friction Reynolds number
ν	Total kinematic viscosity $\nu = 1/Re + \nu_t$
Ω	Temporal growth rate (complex)
ω	Pulsation (real) so that $q = \sum_{m=-\infty}^{\infty} \int_0^\infty \hat{q}_{m,\omega} e^{i(m\theta - \omega t)} + \hat{q}^*_{m,\omega} e^{i(\omega t - m\theta)} \mathrm{d}\omega$
κ	Spatial growth rate (complex)
k	Wavenumber (real)

m	Azimuthal wavenumber (integer)
λ	Wavelength (real)
G	Fluctuations maximum growth
$\hat{\cdot}$	Coefficient in a decomposition, Fourier or otherwise
$\underline{\underline{H}}$	Extractor $\underline{\underline{H}}\,\underline{q} = \underline{u}$, rectangular matrix with long lines
$\underline{\underline{B}}$	Extensor $\underline{\underline{B}}\,\underline{f} = \left[\underline{f}^T\ 0\right]^T$, rectangular matrix with long columns
$\underline{\underline{L}}$	Linearised Navier-Stokes operator
$\underline{\underline{R}}$	Resolvent operator $\underline{\underline{R}}\,\underline{f} = \underline{u}$
$\underline{\underline{M}}$	Mass matrix $\underline{\underline{M}}\,\underline{q} = \left[\underline{u}^T\ 0\right]^T$. Notice that $\underline{\underline{M}} \neq \underline{\underline{B}}$, $\underline{\underline{M}}$ is square.
$\underline{\underline{W}}$	Weighting matrix $\underline{q}^H\,\underline{\underline{W}}\,\underline{s} = \langle \underline{q}, \underline{s} \rangle$
$\sigma^{(i)}$	Resolvent gain, $\forall i \in \mathbb{N}, i < N, \sigma^{(i)} \in \mathbb{R}, \forall j \in \mathbb{N}, j < i \Rightarrow 0 < \sigma^{(j)} \leq \sigma^{(i)}$
$\underline{\psi}^{(i)}$	Resolvent response mode associated to $\sigma^{(i)}$
$\underline{\phi}^{(i)}$	Resolvent forcing mode associated to $\sigma^{(i)}$
$\underline{\xi}^{(i)}$	Spectral Proper Orthogonal Decomposition velocity mode of rank i
$\underline{\zeta}^{(i)}$	Spectral Proper Orthogonal Decomposition non-linear mode of rank i
$\underline{\Sigma}$	Principal shear direction $\underline{\Sigma} = [\partial_r U_x \ \ \partial_r U_\theta]^T$
$\underline{\Lambda}$	Mode wavevector $\underline{\Lambda} = [k \ \ m]^T$
$A(\cdot)$	Surface area
χ	Average alignment $\chi = \frac{1}{A(\mathcal{A})} \int_{\mathcal{A}} \frac{\underline{\Lambda}\cdot\underline{\Sigma}}{\|\underline{\Lambda}\|\|\underline{\Sigma}\|} \mathrm{d}A$
Υ	Standard deviation of alignment $\Upsilon = \frac{1}{A(\mathcal{A})} \int_{\mathcal{A}} \left(\frac{\underline{\Lambda}\cdot\underline{\Sigma}}{\|\underline{\Lambda}\|\|\underline{\Sigma}\|} - \chi \right)^2 \mathrm{d}A$
$\langle \cdot, \cdot \rangle$	Inner product
$[\cdot, \cdot]$	Hermitian inner product
$\cdot^v$	Vector format for tensors
$\cdot_d$	Discretised format
$\cdot^+$	Inner scaling
η	Absolute tolerance
ι	Relative tolerance
h	Grid size
$\mathcal{H}^1_Q$	Solution space on full Taylor-Hood elements
$\mathcal{H}^1_U$	Momentum space only
$\mathcal{H}^1_P$	Pressure space only
$\underline{y}$	Test function on total space $\mathcal{H}^1_Q$
$\underline{v}$	Test function on momentum space $\mathcal{H}^1_U$
s	Test function on pressure space $\mathcal{H}^1_P$
x, y, z	Cartesian coordinates
x, r, θ	Cylindrical coordinates

Contents

Résumé en français

Cette thèse est un travail théorique de mécanique des fluides qui pousse les limites d'application du formalisme résolvent. Ce dernier est une approche linéaire récente très générale au vaste cadre d'application qui a déjà démontré sa pertinence pour de nombreuses géométries et des types d'écoulements variés. C'est une méthode numériquement peu coûteuse, mathématiquement maîtrisée et rigoureuse.

Pourtant, plusieurs freins existent à son application. Tout d'abord, il s'agit d'une méthode relativement nouvelle, introduite dans les années 2000. Ensuite, cette approche peut se révéler inapplicable dans les cas où l'écoulement se révèle instable, et difficile à interpréter pour des non-spécialistes. En effet, il s'agit d'une méthode fréquentielle et globale qui produit des modes de forçage que l'écoulement est particulièrement susceptible d'amplifier pour une fréquence donnée sans pour autant offrir la capacité d'analyse que permet un calcul de stabilité par exemple.

Ce manuscrit est séparé en 6 sections, une introduction qui rappelle les enjeux de la mécanique des fluides numérique et la hiérarchie des modèles dans ce domaine, depuis les formalismes les plus précis et donc les plus coûteux, aux modèles linéaires qui nous concernent dans la suite.

Le second chapitre est un effort d'améliorer la position de la méthode résolvante dans la hiérarchie des modèles précédente, améliorant sa précision en incorporant des termes de second-ordre. En pratique, on accomplit cela en allongeant le vecteur d'état du système et la matrice résolvante, un peu comme pour reformuler une équation d'ordre deux en un système différentiel du premier ordre.

Cette approche s'est révélée fructueuse seulement dans une petite région de l'espace des paramètres, notamment dû à la difficulté de modéliser de façon linéaire le terme en vélocité-gradient de pression. En comparant avec les modes extraits d'une *Spectral Proper Orthogonal Decomposition* d'une simulation numérique à haute fidélité et ceux obtenus par un calcul de résolvante plus simple avec viscosité turbulente, le nouveau modèle semble moins performant que l'état de l'art. On peut néanmoins constater que la comparaison dans le cas de l'écoulement canal est particulièrement défavorable au modèle du second ordre.

Le troisième chapitre concentre le gros de la contribution scientifique de la thèse et commence par une revue bibliographique des différents phénomènes d'amplification qui existent dans la configuration envisagée : un jet turbulent tournant.

La méthode résolvante appliquée à un écoulement de type *Reynolds-Averaged Navier-Stokes* (RANS) a permis de mettre en lumière deux comportements nouveaux des structures turbulentes. A la lumière de l'étude précédente, un modèle de viscosité turbulente fut inclut dans le modèle résolvent pour améliorer la qualité de ses prédictions.

Tout d'abord, en l'absence de rotation mais pour une décomposition azimutale $|m| > 1$ et à une fréquence très faible on observe des structures à l'extérieur de la buse, accompagnés de long filaments des fluctuations dans la couche de cisaillement du jet. Ces structures sont expliquées en invoquant un phénomène semblable au *Lift-Up* d'un type nouveau.

Ensuite, l'introduction de rotation brise la symétrie des modes par rapport au signe de m et met en lumière une amplification spectaculaire à basse fréquence pour $m < -1$. Aucune des instabilités-types de ce type de jets n'explique cette amplification, qui semble se manifester à différents degrés dans différentes parties du mode. L'amplification observée est donc plutôt associée à une manifestation conjointe de phénomène de Kelvin-Helmholtz et centrifuge.

Le chapitre quatre s'attache à détailler les choix numériques effectués dans le développement du code `SPY` qui a permis les résultats précédents. Ces choix sont souvent critiques pour la bonne résolution numérique du problème et relèvent souvent d'un mélange de bonne pratique, de documentation spécialisée et d'expérience.

Enfin, le chapitre cinq conclut les travaux de cette thèse. Il est suivi par une bibliographie.

Chapter 1

Introduction

> We are dwarfs perched on the shoulders of giants.
> We see more and farther than our predecessors, not because we have keener vision or greater height, but because we are lifted up and borne aloft on their gigantic stature.
>
> *Bernard of Chartres*

This thesis strives to find structure in the chaos that are turbulent flows. Such fluids exhibit a high Reynolds number, which is associated with the dominance of inertial effects over viscous ones. Depending on the geometrical configuration, this number can go from as low as a thousand for a flow to qualify as turbulent. Such flows has long been theorised as chaotic, namely dynamic systems that are so sensitive to boundary and initial conditions that the slightest change can bring about dramatic influence in the final flow. Demonstrations of this behaviour can be found in [83, 103].

This behaviour is combined with a strong dependence on the smaller scales. [63] theorised a concept visible in figure 1.1 that is still fundamental in the field today - energy in these flows cascades down the spatial scales in a self-similar fashion until it reaches a scale where the resulting eddies are small enough for viscosity to dominate and dissipate them. In practice though, that scale is painfully small for many flows of interest.

The difficulty here may be better illustrated with an example. Consider a human swimmer inside a twenty-five meters swimming pool. The swimmer moves in a flow at rest and makes his way back and forth a single time. He does so at an average speed of a meter per second. Regular water at room temperature is not a very viscous fluid, leading to a turbulent Reynolds number that ranges in the tens of millions. To fully resolve this flow using Computational Fluid Dynamics in a Direct Numerical Simulation, one would need to capture the Kolmogorov micro-scales, as exposed in [93]. This leads to a grid requirement ranging in the thousands of billions.

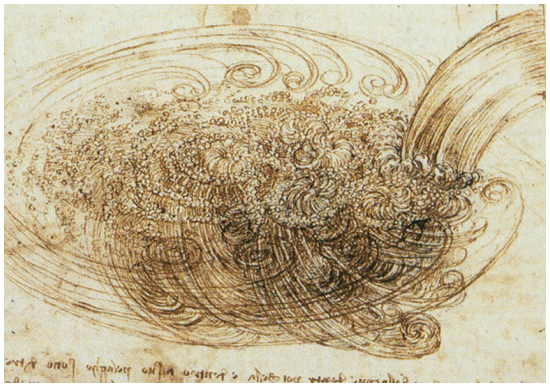

Figure 1.1: Sketch of the eddy cascade by Leonardo da Vinci, XVIth century.

That is not all! Because of the well known Courant Friedrich Levy condition established in [26] which is essential to numerical stability of an advection-type equation, a naive time marching scheme would lead to a final result of about a billion square data points... Which amounts to handling a thousand billion terabytes! By contrast, the Frontier supercomputer at the Oak Ridge National Laboratory, which is thought to be the fastest in the world, only has about forty-two thousand terabytes of Random Access Memory, and a typical modern laptop usually ranges in the tens of gigabytes.

This is still only the memory part of the problem, as the number of operations required to march the scheme forward in time also goes up, yet at this point the picture is pretty clear. Solving turbulent flows in an exact manner is prohibitively expensive computationally.

It is easy to see how these two traits combined create one of the most difficult scientific and engineering conundrum of the century. A turbulent flow depends on scales so small that it becomes numerically unaffordable to solve directly for most applications. At the same time, we know that getting the small scales right is critical to the overall calculation accuracy because of the chaotic behaviour of the equations. To an engineer, this is worse than the fact that proving the existence and uniqueness of solutions to the Navier-Stokes equations with boundary conditions remains an unclaimed Millennium Prize Problem.

Of course, a legitimate way to tackle this issue is forgo the computational approach completely, perform experiments, and measure the quantity of interest. However, the process of building then testing a prototype remains orders of magnitude more expensive than a simulation for many applications. Difficulties can also arise when exploring certain behaviour in detail, such as when instrumentation intrudes upon the flow especially very close to a boundary. Furthermore, there are legitimate safety concerns around early prototype airplanes or rockets that should not be allowed to take off with a numerical proof of concept. Hence, this thesis is focused on numerical models for flows, a field also known as Computational Fluid Dynamics. It goes without saying that experiment remains the final judge of any computation or indeed empirical science in general. The objective here is to make the most of modern computing capabilities and perform fewer experiments in select regimes significant to the problem at hand according to calculation.

Every actor in the ever growing field that is turbulent fluid dynamics, which ranges from a shipbuilder to an aerospace engineer all the way to a fountain designer, is confronted to the previous computational cost issue. Luckily, given the state of knowledge and practises, there are techniques available for every computational budget, see [118, 132].

This study aims at studying one of these methods in more detail. As a first step, let us take a brief look at the modelling toolkit of fluid mechanics relative to turbulent flows in general. This will allow us to better put in context the pros and cons of the chosen method in section 1.1, before we move on to the class of techniques of interest in section 1.2. Once this context has been given, it will be possible to present the scope of this thesis in section 1.3.

1.1 On the modelling of turbulent flows

We have seen that numerical modelling of turbulent flows using Computational Fluid Dynamics (CFD) is driven partly by lingering engineering concerns. This naturally led to a variety of solutions being developed, which will be briefly reviewed in section 1.1.1 before making a case for a specific method in section 1.1.2.

1.1.1 A wide range of options

When choosing a modelling method, there has to be a trade-off between how much is modelled and how insightful the resulting simulation is. In CFD, this dilemma is incarnated in the so-called closure problem. Indeed, a numerical method is 'closed' when it is well-posed and features enough equations and boundary conditions with respect to its unknowns to attempt to solve it. This is equivalent to choosing how much is modelled, and how much is resolved.

Direct Numerical Simulation (DNS). The most simple and direct solution to the previously outlined conundrum remains to compute everything up to the viscous scale. To achieve this, one must more often than not compromise on the problem's boundaries, either limiting the maximum computation time or the breadth of the domain considered. This approach gained traction as numerical resources grew

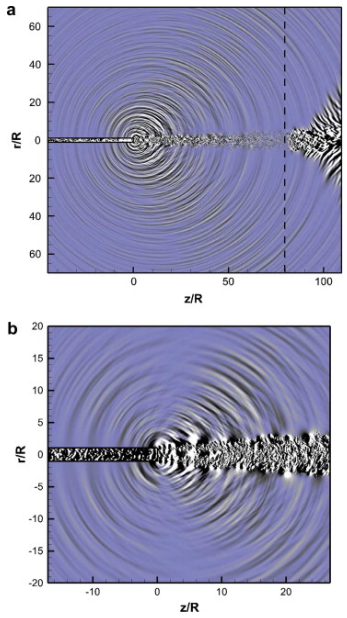

Figure 1.2: Restitution of figure 15. of [117] representing the DNS of a compressible pipe at Reynolds number $Re = 7,500$. a is a dilation field, b represents the density gradients close to the nozzle.

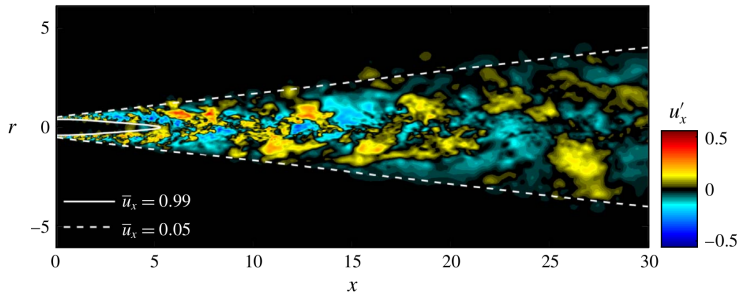

Figure 1.3: Extract of figure 1. of [121] representing the LES of a jet at $Re = 10^6$. Axial fluctuations and baseflow level-sets are presented.

and put complex configurations within reach. Indeed, even moderate Reynolds number are attainable today. Notice the self similarity between the different scales visible in figure 1.2, as described in [63].

However, there are reasons to believe many cases of interest will remain durably out of reach of DNS. After all, one cannot expect computing power to infinitely grow - Moore's law has already been proven wrong in recent years due to quantum effects, and energy consumption concerns associated with the fight against rapid climate change do not bide well for unbridled High Performance Computing.

Large Eddy Simulation (LES). This solution can be understood as something of a compromise, using a space and time-wise filter to smooth out some of the irregularities in a turbulent flow. This is the most recent of the three alternatives presented here, first detailed in [125]. Initially developed for the modelling of atmospheric flows with the intent of improving weather forecast accuracy, this model is now widely used in aerodynamics.

Comparing figures 1.3 and 1.2, it is easy to see that the method makes it possible to attain higher Reynolds number at the cost of simulation detail. It has seen some success in the industry, however the most accurate versions of this method remain computationally out of reach for many users.

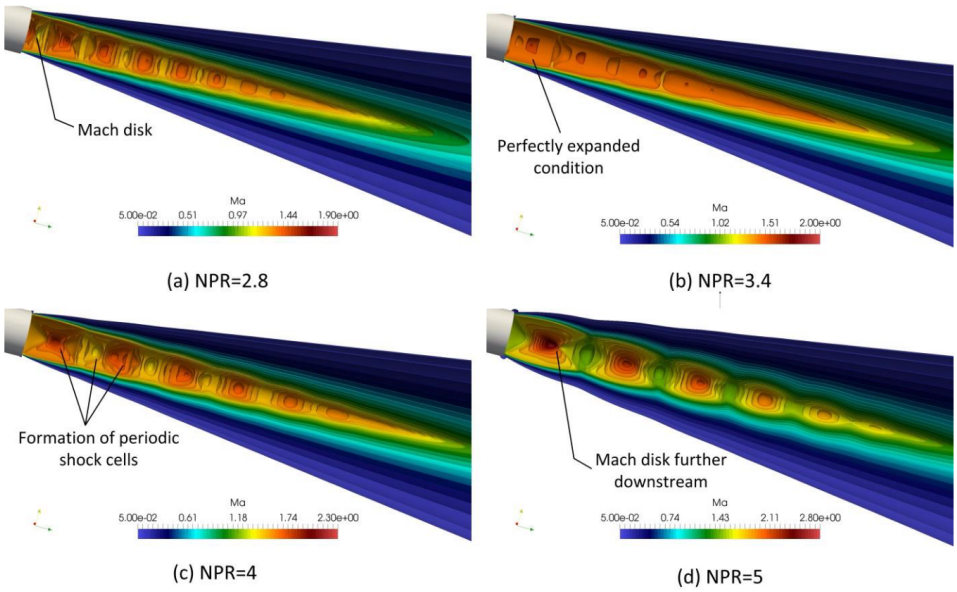

Figure 1.4: Restitution of figure 5. of [138] representing the Mach number Ma for a RANS calculation for a compressible jet for different Nozzle Pressure Ratios (NPR). This study used the `OpenFOAM` suite from [94] just like in chapter 3, albeit with a different solver `rhoCentralFoam`.

Reynolds Averaged Navier Stokes (RANS). This approach is akin to the previous one, but instead of using a filter makes an argument on ensemble averaging to separate baseflow from fluctuations or small-scale perturbations. The main difference between ensemble averaging and the usual LES filter is that the former always commutes with time or space differentiation. Overall, RANS is usually performed on a coarser grid, cheaper and less precise than LES. Methods of this type pre-date the alternatives listed here and go as far as [110]. Indeed, once there was no other way to study turbulent flows.

Comparing figure 1.4 to figures 1.3 and 1.2, much has been lost in the way of flow details. However, the study [20] which is a validation case for [121] from which figure 1.3 is extracted took about $172,000$ core hours to compute. By contrast, figure 1.4 cost about 576 core hours.

For many applications only a few quantities are of actual interest. For instance, the study of jet noise is mostly concerned with far field behaviour of pressure fluctuations, not the entirety of complex flow behaviour at all scales. Yet it remains a legitimate research topic recently addressed in [102, 134]. For such uses, it makes sense to look for the solution with the best ratio between computational cost and resulting insight. That solution is often the same as the cheapest one.

1.1.2 Dive into Reynolds Averaged Navier Stokes

In this thesis we are mainly concerned with the last of the previous three methods, namely RANS type formalism. This approach is used in different industries as it provides sufficient precision for many applications while remaining very affordable.

Constitutive equations

The core idea between this approach hinges on ensemble averaging, a Reynolds operator that allows separation of total flow quantities $\underline{\mathtt{q}}$ into averaged $\underline{Q}$ and perturbations $\underline{q}$.

Starting from the incompressible dimensionless Navier-Stokes Equations (NSE)

$$\begin{cases} \partial_t \underline{\mathtt{u}} + \underline{\underline{\nabla \mathtt{u}}}\ \underline{\mathtt{u}} + \underline{\nabla \mathtt{p}} - \underline{\nabla} \cdot \left[\left(\underline{\underline{\nabla \mathtt{u}}} + \underline{\underline{\nabla \mathtt{u}}}^T \right) / Re \right] = \underline{0}, \\ \underline{\nabla} \cdot \underline{\mathtt{u}} = 0, \end{cases} \tag{1.1}$$

using the conventions detailed in the list of symbols on page iv. The second relation is also called the

continuity equation and denotes incompressibility. This thesis is concerned only with incompressible fluids.

Baseflow equations are obtained by performing ensemble average of equation (1.1)

$$\begin{cases} \partial_t \underline{U} + \underline{\underline{\nabla U}}\ \underline{U} + \underline{\nabla} P - \underline{\nabla} \cdot \left[\left(\underline{\underline{\nabla U}} + \underline{\underline{\nabla U}}^T \right) / Re \right] = - \overline{\underline{\underline{\nabla u}}\ \underline{u}}, \\ \underline{\nabla} \cdot \underline{U} = 0. \end{cases} \tag{1.2}$$

A baseflow $\underline{Q} = \left[\underline{U}^T \ P \right]^T$ is defined as a vector state satisfying equation (1.2) or more generically as a flow upon which instability analysis is performed. A word is warranted here. "Baseflow" and "mean flow" will not be used interchangeably in this thesis, even if by definition $\underline{Q} = \overline{\underline{\mathrm{q}}}$. A mean flow will be considered not as a solution to an equation, but as the time average of an experimental or DNS flow instead. This is assumed to be equivalent to an ensemble average because of the ergodic nature of turbulent flows, which will be be detailed in section 1.2.1. Hence, all mean flows can be baseflows in an instability analysis sense, but the converse is not true.

The corresponding fluctuation equations are obtained by subtracting relations (1.2) from (1.1)

$$\begin{cases} \partial_t \underline{u} + \underline{\underline{\nabla U}}\ \underline{u} + \underline{\underline{\nabla u}}\ \underline{U} + \underline{\nabla} p - \underline{\nabla} \cdot \left[\left(\underline{\underline{\nabla u}} + \underline{\underline{\nabla u}}^T \right) / Re \right] = \overline{\underline{\underline{\nabla u}}\ \underline{u}} - \underline{\underline{\nabla u}}\ \underline{u}, \\ \underline{\nabla} \cdot \underline{u} = 0. \end{cases} \tag{1.3}$$

The left-hand sides of equations (1.2) and (1.3) are both linear. So far, the equations are exact, which also means that nothing has been gained from a modelling perspective. There are two ways to think about RANS from here. On the one hand, it is a predictive engineering tool at zeroth order, if only a model could be found for the right-hand side term of the baseflow equations $\overline{\underline{\underline{\nabla u}}\ \underline{u}}$. In that case, equations (1.3) are more often than not completely discarded.

The components of the tensor $\overline{\underline{\underline{\nabla u}}\ \underline{u}}$ are called Reynolds-stresses, as per their dimensionality in relations (1.2). Because the incompressibility of the fluctuations, they can also be formulated as the average of the divergence of the fluctuation velocity correlation tensor $\overline{\underline{\underline{\nabla u}}\ \underline{u}} = \overline{\underline{\nabla} \cdot (\underline{u}\underline{u}^T)}$. Intuitively, this term represents fluctuations feedback, or in other words the influence of turbulent fluctuations on the baseflow equations (1.2). They play a key role in the energy cascade of [63]. Their importance cannot be overstated.

Indeed, taking out this tensor entirely and solving the system (1.2) using a naive nonlinear solver in a turbulent regime on a coarse grid usually leads to a laminar flow, which does not accurately account for the effect of the small scales and the energy cascade. Laminar flows, as opposed to turbulent flows, may be formal solutions of system (1.2), but are never observed in practice as they become very unstable at high Reynolds number.

On the other hand, it is possible to think of perturbation equations (1.3) as a linearisation of a baseflow around an equilibrium point, and perform an instability analysis. Just like in many other mechanic problems, one picks a baseflow that is known to bifurcate in some manner and look for instabilities that could explain large scale behaviour. In that case, $\partial_t \underline{Q} = \underline{0}$ is often assumed, and equations (1.3) are kept. The two approaches will be reviewed in turn.

Modelling the Reynolds stresses

Establishing a satisfying model so that $\overline{\underline{u}\underline{u}^T} = \underline{\underline{g}}\left(\underline{Q}\right)$ amounts to solving the closure problem and represents a whole field of research. Indeed, if a universal and accurate Reynolds Stress Model (RSM) was found, RANS would be the norm and many CFD practitioners would be out of a job! In practice, only tailored solutions exist, which can be found in reviews such as [65, 99].

Nonetheless, even with an imperfect model, as long as its evaluation remains numerically cheap, such an approach yields insight on new design at low cost, which is enough for many engineers. Nothing constrains $\underline{\underline{g}}$ to be linear, in fact, many RSMs are not linear, as the one exposed in [61]. However, there is a whole class of methods based on the specific assumption

$$\overline{\underline{u}\underline{u}^T} \approx \nu_t \left(\underline{\underline{\nabla U}} + \underline{\underline{\nabla U}}^T \right). \tag{1.4}$$

Equation (1.4) models the effect of turbulence as an additional viscosity. It amounts to considering the effect of turbulence and the Kolmogorov cascade as a purely dissipative effect on the baseflow. With

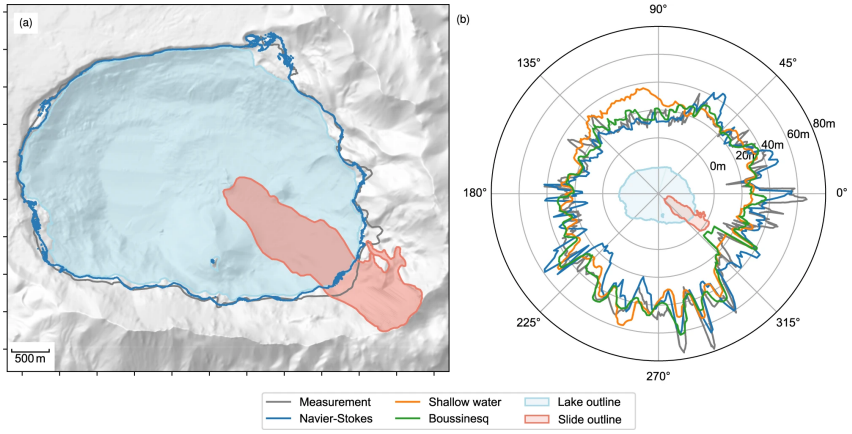

Figure 1.5: Reproduction of figure 8. of [106] studying an Iceland lake landslide showing simulated in blue compared to the measured maximum inundation in grey in `(a)`. `(b)` show the maximum run-up as a function of the azimuth from the centre of the lake. The result of the model is shown in blue, posteriori optimised depth-integrated simulations are shown in green and orange and the measured maximum inundation is shown in grey.

this formalism, turbulence never drives anything and only acts as a momentum sink, eating away at the baseflow more efficiently than usual molecular friction would. While this assumption represents a very restrictive vision of turbulence, it does reproduce a major consequence of its presence and often improve the numerical stability of relations (1.2) as a side effect.

A range of models exist for the turbulent eddy viscosity ν_t, for instance the well-known $k-\epsilon$ model introduced for the first time in [57] and quickly extended by [64]. This is a two-equation model that emulates turbulent kinetic energy and dissipation at the same time. Other expressions include Cess's model derived in [111], a one-equation model designed specifically for channel flow, and the Spalart-Allmaras (SA) model presented in [126]. Both are one-equation models, the former will reappear in chapter 2, and the latter in chapters 3 and 4 of this thesis.

This approach is wildly used in the industry, as well as academic research. Indeed, implementing relations (1.2) with an eddy viscosity (1.4) is fairly straightforward and can serve as a good tractable model for a turbulent fluid that can be coupled with something else relevant to the case at hand, such as a chemical reaction, solid mechanics or even nuclear emissions. Such methods are often well validated and robust, even though they require special treatment near boundaries. So called "wall functions" are often required to provide numerically required boundary conditions on different types of walls.

For instance, [106] performed a multi-phase computation on an Iceland lake landslide, using the canonical eddy viscosity $k-\epsilon$ model in the fluid to attain Reynolds numbers as high as $Re = 10^{10}$. The fluid model was coupled with a granular model for the solid, yielding a three-phase problem. Figure 1.5 is taken from this study, which achieves an average inundation error of about eight metres. Such an example demonstrates that RANS equations with an eddy-viscosity model can be enough to obtain useful insight even for challenging problems. This study made use of the `OpenFOAM` library from [94] to compute a baseflow with eddy-viscosity in a similar manner as the one developed in chapter 3 of this thesis, though for a much larger and challenging multi-phase problem.

Instability approach

Instead of trying to obtain a baseflow $\underline{Q}$, this approach is more interested in the fluctuations $\underline{q}$ around a provided baseflow. In this mindset, the quantities of interest are the perturbations most amplified by the baseflow. This amounts to looking farther than the averaged quantities for the first order of fluid mechanics, searching amongst terms allowed to vary with time for the optimal turbulent configuration.

This approach is especially fruitful if the studied configuration is known to exhibit transitions. In this case an instability-type study can provide valuable insight at very little cost when it comes to controlling an important change in the flow, such as vortex breakdown as in [80] or the well-known transition to

turbulence studied in [77] amongst many others.

Indeed, the strong nonlinearity inherent to the NSE is known to enable quite complex flow transitions for a variety of regimes. In the case of vortex breakdown, a swirling flow can exhibit recirculation as swirl intensity is increased, which can in turn give rise to new instabilities that would not exist without a recirculation bubble. Likewise, the turbulent transition is associated with increased drag for aircraft, but also additional pressure and resistance in pipe flows. The study of such transitions is as old as the field of fluid mechanics, not only because clear-cut transitions are easy to characterise, but also out of genuine engineering interest.

Nonetheless, this range of applications may seem constrained compared to the previous approach. Modelling the Reynolds stresses makes it possible to address almost any flow for a wide range of regimes, as literature on the subject is extensive, with many different models tailored according to the specific use case. However, modelling the Reynolds stresses and performing instability analysis are not exclusive. It is possible to compute a stationary baseflow using an eddy viscosity model in a regime known to be transition-prone and perform instability analysis on it to better characterise this transition. This amounts to computing an overall averaged solution, before examining more closely how turbulence might interact with that baseflow. In fact, such is the approach followed in chapter 3 of this thesis.

There are many ways to think about flow perturbations, and the one followed here is more concerned with fluctuations - $\underline{q}$ is defined as having zero ensemble average, not necessarily a small amplitude. This is significant because most instability models keep the baseflow fixed, which amounts to neglecting fluctuations feedback into the baseflow. Therefore, if $\underline{q}$ grows out of control, the resulting flow becomes non-physical.

In the following, we will restrict the domain of interest further by focusing on linear methods. These approaches take the spirit of RANS the farthest - modelling fluctuations in a linear, thereby cheap, manner.

1.2 Various linear methods

This work is mostly concerned about RANS as a framework for instability analysis with the additional assumption of linearity of the perturbation equations. Amongst many others, three approaches will be reviewed in the following, namely stability analysis in section 1.2.2, optimal growth in section 1.2.3 and resolvent analysis in section 1.2.4. Before moving on to these different techniques, a word on the hidden costs of linear methods is warranted.

1.2.1 The price to pay for linearity

A common trait of linear methods is that they renounce the quest to find an exact representation of the fluctuations $\underline{q}$ in time. Instead, they only concern themselves with the most amplified structures by a given operator. This represents significantly less information than the full time evolution of the fluctuations, and at the same time this represents one of the driving force behind their computational appeal.

How much of a loss is it to go from exact time evolution to most amplified structures of turbulent fluctuations? A known feature of turbulence aside from the chaotic behaviour is ergodicity. This property means that if $\underline{q}$ lives in a space $\mathcal{H}^1_Q$, it will eventually visit all points of this space with equal probability. There is no proof of this, yet it remains a recurring observation since the beginning of modern fluid mechanics. More formally, given measures $\mu_{\mathcal{H}}$ and $\mu_{\mathbb{R}}$ of the relevant spaces, ergodicity may be written as

$$\forall C \in \mathbb{R}^+, \forall V \subset \mathcal{H}^1_Q, \mu_{\mathcal{H}}(V) = C \Rightarrow \exists I \subset \mathbb{R}^+ | \begin{cases} \mu_{\mathbb{R}}(I) = C, \\ \forall t \in I, \underline{q}(t) \in V. \end{cases} \tag{1.5}$$

This property of turbulence has two important consequences. Firstly, fluctuations are expected to have a limited memory. Indeed, since fluctuations explore all possible configurations over time, they are expected to explore most probable configurations in finite time. Past this point, the probability of turbulent fluctuations to return to a previously attained configuration increases. Therefore, redundant information will occur when computing exact behaviour over long time-scales.

Secondly, optimal configurations will be explored as part of the natural evolution of the fluctuations. If all values are equally attainable, and most of them lead to nothing but some are strongly amplified, it makes sense to give up on the unimportant parts of fluctuations from the beginning of the modelling strategy. In other words, in conditions where it can be established that optimal configurations with a much more drastic impact on the flow than most alternatives exist, these become the natural focus of study.

As a side note, it might strike the reader as strange that the term 'coherent' be used for fields that have zero ensemble average by definition. This term is used to contrast destabilising modes with the chaotic picture of turbulent fluctuations in general. Indeed, the most interesting features of turbulence are those that are 'coherent' enough to have significant energy and drive instability.

Last but not least, focusing on linear methods opens the way for Reduced Order Modelling (ROM) of the flow, an approach which endeavours to correctly reproduce as much of the fluctuation energy as possible using only a few modes obtained from linear methods. A general approach to achieve ROM at accuracies relevant for most applications amounts, again, to solving the closure problem by obtaining a reliable, accurate and cheap CFD method, albeit one limited to the framework of instability studies.

However, the choice of a linear formalism is from the onset fraught with risk. The NSE are not linear, so it is possible for phenomena that will never be properly captured by a linear formalism to arise in a real flow. Such phenomena accumulate and build on one another when considering very stiff coupled equations such as flame behaviour. This is part of the price to be paid when taking the cheapest option to the closure problem, and it is possible that this approach never manages to capture some important configurations in a satisfying manner.

1.2.2 Modal stability analysis

Local temporal stability analysis

One of the most popular methods of modelling the fluctuations $\underline{q}$ is assuming that they satisfy

$$\underline{q}(\underline{x},t) = \hat{\underline{q}}(\underline{x})e^{\Omega t} + \hat{\underline{q}}^*(\underline{x})e^{\Omega^* t},\ \Omega \in \mathbb{C}. \tag{1.6}$$

Note that equation (1.6) is not a Fourier decomposition as it allows for amplitude variation. Indeed, it would amount to a Fourier transform in time if Ω was imaginary. In a two-dimensional case, such methods will also often assume a parallel flow with no variation in x. Since the baseflow must satisfy system (1.2), it cannot vary in any other direction than the one orthogonal to motion, $\underline{U}(\underline{x}) = U(y)\underline{e}_x$. In this framework, local analysis equations go

$$\underline{q}(x,y,t) = \hat{\underline{q}}(y)e^{\kappa x+\Omega t} + \hat{\underline{q}}^*(y)e^{\kappa^* x+\Omega^* t},\ (\kappa,\Omega) \in \mathbb{C}\times\mathbb{C}. \tag{1.7}$$

In itself, these assumptions are not enough to obtain a solution. One must also neglect the non-linear terms in equation (1.3), which gives

$$\begin{cases} \underline{\underline{\nabla U}}\ \hat{\underline{u}} + \underline{\underline{\nabla \hat{u}}}\ \underline{U} + \underline{\nabla}\hat{p} - \underline{\nabla}\cdot\left[\left(\underline{\underline{\nabla \hat{u}}} + \underline{\underline{\nabla \hat{u}}}^T\right)/Re\right] = -\Omega\hat{\underline{u}}, \\ \underline{\nabla}\cdot\hat{\underline{u}} = 0. \end{cases} \tag{1.8}$$

In the following, the whole fluctuations system will be reformulated as a generalised eigenvalue problem. Writing

$$\underline{\underline{L}}\,\hat{\underline{q}} = \begin{bmatrix} \underline{\underline{\nabla U}}\ \hat{\underline{u}} + \underline{\underline{\nabla \hat{u}}}\ \underline{U} + \underline{\nabla}\hat{p} - \underline{\nabla}\cdot\left[\left(\underline{\underline{\nabla \hat{u}}} + \underline{\underline{\nabla \hat{u}}}^T\right)/Re\right] \\ \underline{\nabla}\cdot\hat{\underline{u}} \end{bmatrix},\quad \underline{\underline{M}}\,\hat{\underline{q}} = \begin{bmatrix} \hat{\underline{u}} \\ 0 \end{bmatrix}, \tag{1.9}$$

and further assuming a purely imaginary κ, which amounts to a Fourier transform in x, one can write equation (1.8) in compact form

$$\underline{\underline{L}}\,\hat{\underline{q}} = -\Omega\,\underline{\underline{M}}\,\hat{\underline{q}},\ \kappa = ik,\ (k,\Omega) \in \mathbb{R}\times\mathbb{C}. \tag{1.10}$$

From there, one may pick a range of real axial wavenumber k and solve for associated complex Ω to perform Local Temporal Stability Analysis (LTSA) as in [66, 71] and many others beside.

This process is also called modal analysis, and dates back to [108]. Historically, this is the first tool in the physicist toolkit, passed on to us from a time when there was no "C" in CFD. A large real part

of Ω is associated with strong instability and by contrast, finding $\Re(\Omega) < 0$ for all attainable Ω is an indicator of a temporally stable flow for a range of wavenumber k.

LTSA has proven fruitful at capturing many behaviours of flows and has been applied for a variety of configurations, for instance in [39] where it was applied to a rotating plug flow to better characterise instabilities in such a configuration.

Local spatial stability analysis

Some authors are more interested in spatial growth. Unfortunately equation (1.10) is non-linear with respect to κ as a κ^2 term appears from the viscous term. This can be circumvented in the high Reynolds number limit by assuming an inviscid flow, which removes the viscous term and leads back to a generalised eigenvalue problem

$$\Omega \underline{\underline{M}}\, \underline{\hat{q}} + \underline{\underline{\mathcal{L}}}\, \underline{\hat{q}} = -\kappa \underline{\underline{\mathcal{M}}}\, \underline{\hat{q}}, \Omega = i\omega,\ (\kappa, \omega) \in \mathbb{C} \times \mathbb{R}. \tag{1.11}$$

A more general approach that retains the viscous term involves the so-called companion matrix method and implies extending the state vector $\underline{\hat{q}}$ into $\underline{\tilde{q}} = \left[\underline{\hat{q}}^T \ \ \kappa\underline{\hat{q}}^T\right]^T$. This allows a reformulation of the problem as

$$\left(\kappa^2 \underline{\underline{A}}_2 + \kappa \underline{\underline{A}}_1 + \underline{\underline{A}}_0\right) \underline{\tilde{q}} = \Omega \underline{\underline{M}}\, \underline{\tilde{q}} \Leftrightarrow \left(\begin{bmatrix} \underline{\underline{A}}_0 & \underline{\underline{0}} \\ \underline{\underline{0}} & -\underline{\underline{I}} \end{bmatrix} - \Omega \begin{bmatrix} \underline{\underline{M}} & \underline{\underline{0}} \\ \underline{\underline{0}} & \underline{\underline{0}} \end{bmatrix} \right) \underline{\tilde{q}} = -\kappa \begin{bmatrix} \underline{\underline{A}}_1 & \underline{\underline{A}}_2 \\ \underline{\underline{I}} & \underline{\underline{0}} \end{bmatrix} \underline{\tilde{q}}. \tag{1.12}$$

In equation (1.11) or (1.12), it is possible just like in LTSA to pick a range of real ω and solve for associated complex κ as in [72]. Such an approach can be described as Local Spatial Stability Analysis (LSSA).

Absolute and convective instability

For simple flows, it may be possible to do away with the vectors completely and obtain an explicit dispersion relation linking κ and Ω, keeping both these numbers complex. Such an approach is best qualified as Local Spatio-Temporal Stability Analysis (LSTSA). Formally, this amounts to finding $\Omega(\kappa)$ so that for a set of $\kappa \in \mathbb{C}$, equation (1.11) is always satisfied regardless of $\underline{q}$.

It is not always possible to obtain a dispersion relation $\Omega(\kappa)$ for a real flow, nor can it be solved for any arbitrary wavenumber κ, but some $\Omega(\kappa)$ relations can be surprisingly tractable analytic functions. For instance, an explicit dispersion was used to characterise rotating plug flow instabilities and used to derive limit behaviours in [70]. In general, the wavenumbers satisfying

$$\kappa_0 \in \mathbb{C} | \partial_\kappa \Omega(\kappa_0) = 0 \tag{1.13}$$

are of special interest. The quantity $\partial_\kappa \Omega$ is called group velocity and pilots the mode's behaviour - $|\partial_\kappa \Omega| > 0$ means that the fluctuations are moving and will eventually be convected away at the domain boundary, even though they may be growing rapidly with respect to time. In this case, the flow is at worst convectively unstable, even if $\exists \kappa_0 \in \mathbb{C} | \Re(\Omega(\kappa_0)) > 0$. However

$$\exists \kappa_0 \in \mathbb{C} | \begin{cases} \partial_\kappa \Omega(\kappa_0) = 0, \\ \Re(\Omega(\kappa_0)) > 0. \end{cases} \tag{1.14}$$

is associated to absolute instability, or unbridled growth of the perturbations at every point of the domain, see figure 1.6. This is called the Briggs-Bers pinching criterion as it was derived in [14] in the context of plasma physics.

The dispersion relation $\Omega(\kappa)$ can be hard or even impossible to compute for an arbitrary parallel baseflow profile. Thankfully, there exists an equivalence between the Briggs-Bers pinching criterion and a time march given specific initial conditions. As established in [19, 28], it is possible to link the linear evolution of an impulse along relations (1.8) to absolute or convective instability. Intuitively, an impulse contains many different spatial wavelengths and therefore taking the time-evolution evolution of an impulse is akin to exploring many κ at once. If the linear evolution of the impulse leads to oscillations propagating across the domain in finite time, the flow is absolutely unstable.

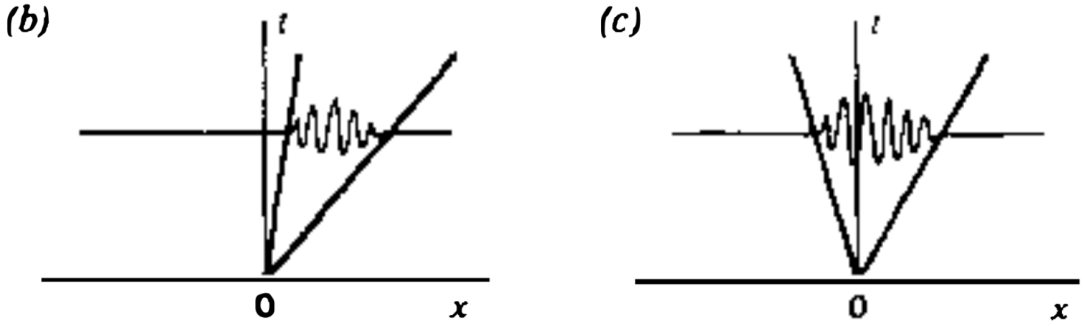

Figure 1.6: Restitution of figure 1. of [52] illustrating the fundamental difference between convective (b) and absolute (c) instability.

Another way to think about flow behaviour in this formalism is the so-called critical nature of the flow. Criticality of a flow is a concept taken from compressible literature defined in [23] as follows. A flow is considered subcritical if a wave with negative group velocity can arise. Conversely, a supercritical flow only tolerates waves convected downstream.

Subcritical behaviour is a necessary but not sufficient condition for absolute instability, while supercriticality implies at most convective instability. In itself, flow criticality gives no information on fluctuation growth, only on the possible direction of wave propagation.

From local to global analysis

Assuming a parallel flow is a very strong hypothesis. Not only does it neglects U_y, it also imposes no baseflow variation in x and periodic boundary conditions for fluctuations in the x direction. Doing LTSA reduces the problem to an infinitesimal slice of flow that is evolving with respect to x as a sinusoidal wave, oscillating in time, and either growing or decaying exponentially.

In an effort to relax the parallel flow hypothesis, an approach called weakly non-parallel analysis was developed. The gist of this method is to assume a slowly varying flow and to write equation (1.7) locally for different planes of constant x. One can then extrapolate a solution throughout the entire domain by combining the contributions of different waves, each computed in a LTSA framework at a slice. This method is applied for instance in [92]. However, this does not alleviate the constraints on fluctuations boundary conditions or on the baseflow.

Some authors such as [80] do away with equation (1.7) completely and perform so-called Global Temporal Stability Analysis (GTSA) throughout the entire domain at once. Removing the spatial wavenumber finally allows the fluctuations to grow on a baseflow evolving in x. This method requires more computing power, but it has gained traction in the community as algorithms and computers continue to progress.

An example of a GTSA study that is very close to chapter 3 of this thesis is presented in figure 1.7. For a swirling flow where increasing swirl leads to a transition with the formation of a recirculation bubble through a process called vortex breakdown, GTSA can help understand this transition by singling out the modes that contribute most to the instability. These are visible on the lower half-planes numbered 4-5-6 in figure 1.7 and can represent a control objective to pilot this transition.

A subtle impact of moving from a LSTSA to GTSA is the loss of "readability", so to speak. In practice, it is often possible to associate every term in a dispersion relation $\Omega(\kappa)$ with a physical mechanism. LTSA modes also require interpretation as phenomena interact, but have a tendency to separate modes depending on the driving mechanism and its associated wavelength. On the other hand GTSA provides an optimal eigenmode with no explanations attached. It is up to the physicist to understand what is driving this mode.

An approach developed to address this and explain GTSA modes *a posteriori* is called structural sensitivity or wavemaker analysis. It practice, it consists of an outer product, multiplying component-wise momentum modes of the adjoint stability operator and standard stability modes. This provides a 3×3 sensitivity tensor which indicates areas where the fluctuations are most sensible to a baseflow change, but also hints at the most important interactions with regards to a mode's growth.

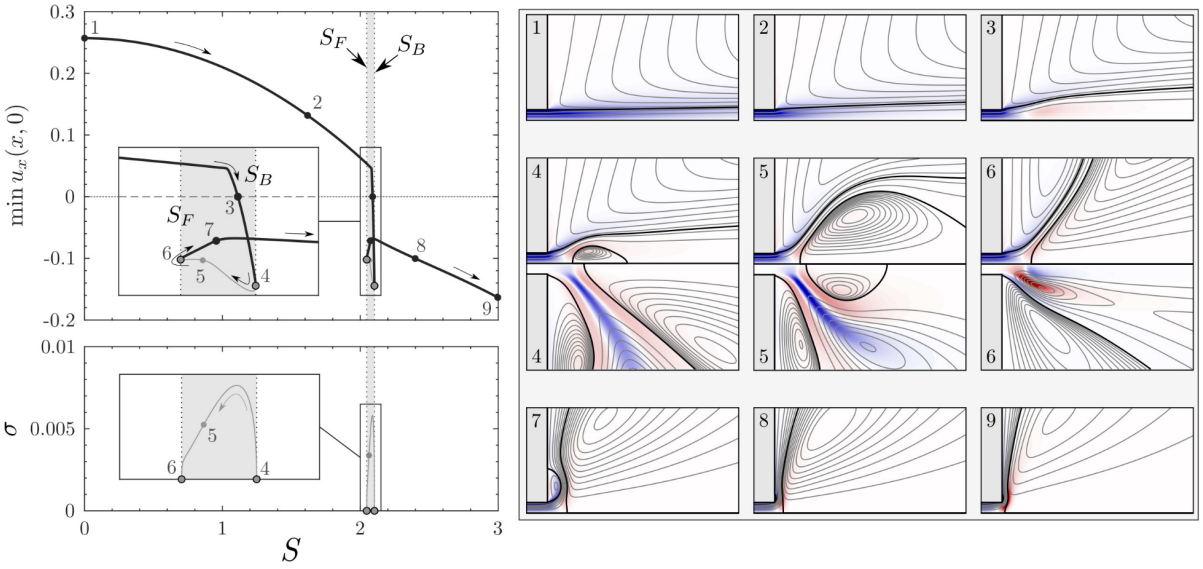

Figure 1.7: Reproduction of figure 3.1 of [25] concerned with study of a swirling round jet at $Re = 100$. In the top left corner, minimum axial velocity on the axis $\min U_x(x,0)$ as a function of swirl intensity S is presented. Growth rates $\sigma = \Re(\Omega)$ as a function of swirl are visible in the bottom left corner when the flow is absolutely unstable. Unstable region is in grey in these curves. $x-r$ planes of the baseflow vorticity and isolines over $(x;r) \in [-1;9] \times [0;5]$, with unstable eigenmodes on the lower half-plane if available, are presented on the right.

For example, in a flat plate flow, a sensitivity analysis giving a strong interaction between components of y and z in the adjoint and x in the response is indicative of the lift-up phenomenon, which will be explored in more details in section 3.1.1.

This method was introduced in [47] and put in practice in [105]. As an illustration of wavemaker analysis, one can see in figure 1.8 that the region in front of the breakdown bubble is especially significant for the counter-rotating spiral mode at $m = -1$. Indeed, a strong growth rate is observed there, especially for diagonal radial and azimuthal components.

Method limits

It is also important to point out that this method can only address self-sustaining structures in the long time limit. By design, it is unable to address fluctuations responding to exterior forcing. Another important drawback of this approach comes from the non-normality of the NSE, which means its eigenvalues can be non-orthogonal. This decreases the utility of a modal approach, as even a modally stable non-normal system can exhibit significant transient growth.

Figure 1.9 illustrates this phenomenon. An aptly chosen initial condition may exhibit substantial transient growth even in a temporally stable non-normal system. This is a problem when interpreting modal stability results when doing CFD of turbulent flows, when operator $\underline{\underline{L}}$ is never self-adjoint or normal. Temporal stability analysis results always stand at long time scales, but important transient effects are simply not captured by this approach. As pointed out in section 1.1.2, this can be enough to cast doubt over the relevance of the entire instability approach when feedback into the baseflow equations is neglected.

1.2.3 Optimal growth

Another popular method of turbulent flows study is called optimal growth. This approach addresses a major shortfall of the previous one by accounting for time dependence. Starting from equations (1.8),

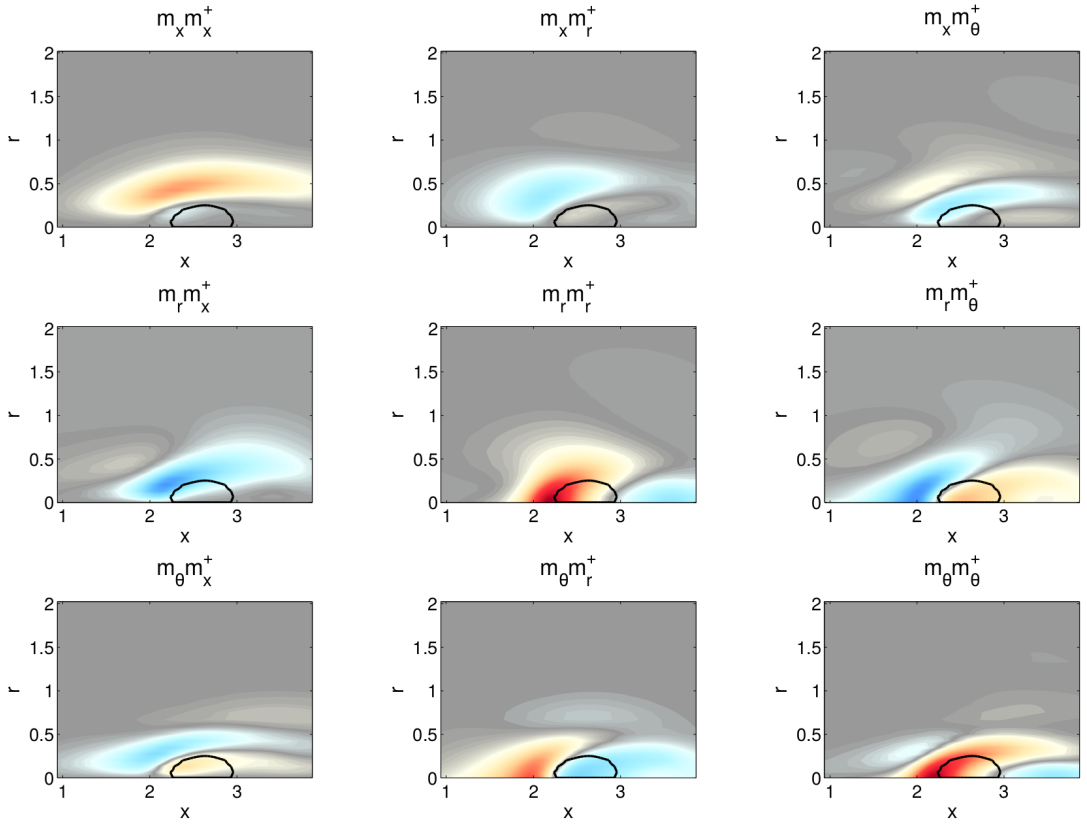

Figure 1.8: Restitution of figure 4. of [105] illustrating real parts of components of the sensitivity tensor $\underline{mm}^H = \underline{qq}^H$. The plot colours scale from -2256 (blue) to 2256 (red). This study concerns the Grabowksi-Berger vortex detailed in section 4.4.1 for $Re = 200$. The modes were decomposed azimuthally and only the $m = -1$ mode is displayed here for a swirl intensity $S = 0.915$. The black line show the breakdown bubble.

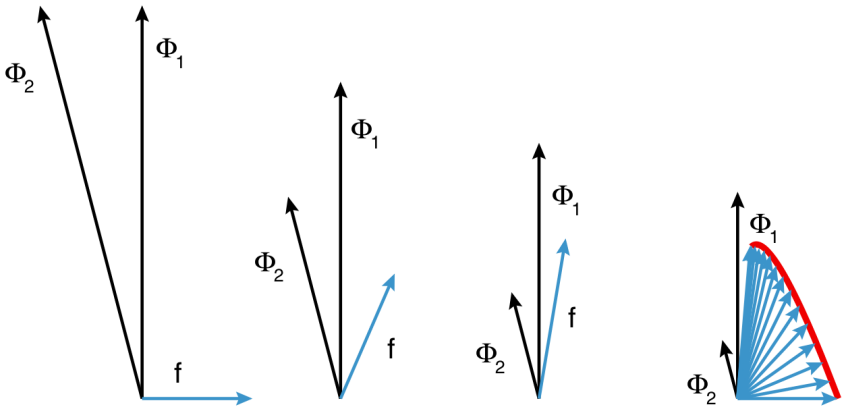

Figure 1.9: Restitution of figure 2. of [118] illustrating transient growth of a modally stable non-normal system. $\underline{f} = \underline{\Phi}_2 - \underline{\Phi}_1$, time evolution goes from left to right, $\underline{\Phi}_1$ reduces by 20% and $\underline{\Phi}_2$ by 50% at every iteration.

one may take the divergence of the velocity equation and obtain the Poisson formulation for pressure

$$\Delta p = -\underline{\nabla} \cdot (\underline{\underline{\nabla U}}\,\underline{u} + \underline{\underline{\nabla u}}\,\underline{U}) \tag{1.15}$$

through use of the fluctuation continuity equation $\underline{\nabla}\cdot\underline{u} = 0$. Injecting this back into the velocity equations eliminates pressure and gives

$$\partial_t \underline{u} = \underline{\underline{\mathscr{L}}}\,\underline{u}. \tag{1.16}$$

This system is deceptively similar to (1.10), but presents a very important difference. The mass matrix $\underline{\underline{M}}$ that was required in relations (1.10) to account for the incompressibility equation is gone. Without it, one may directly solve the time-varying system given initial conditions $\underline{u}_0$ as

$$\underline{u} = e^{t\,\underline{\underline{\mathscr{L}}}}\,\underline{u}_0. \tag{1.17}$$

This allows the quantification of maximal fluctuations growth at time t_1 as

$$G(t_1) = \max_{\underline{u}_0} \frac{\|\underline{u}\|}{\|\underline{u}_0\|} = \left\| e^{t_1\,\underline{\underline{\mathscr{L}}}} \right\|. \tag{1.18}$$

From there, it is natural to focus on the fluctuations that amount to the greatest disturbance at time t_1, namely

$$\underline{u}_{t_1} = \arg\max_{\underline{u}_0} \frac{\|\underline{u}\|}{\|\underline{u}_0\|}. \tag{1.19}$$

The latest formulation is close to an eigenvalue problem. Indeed, diagonalising $\underline{\underline{\mathscr{L}}}$ instantly solves system (1.16). However, even if equation (1.16) is purely linear, the inclusion of finite time in equation (1.19) does capture some transient phenomenon. Consider for instance a case where operator $\underline{\underline{\mathscr{L}}}$ has a clearly dominant eigenvalue Ω_1 with a large real part. This mode is expected to dominate the long term dynamics because of its largest growth rate, and this is readily supplied by the temporal stability analysis detailed in 1.2.2. However, if one substitutes for instance $t_1 = \pi/2\Im(\Omega_1)$ in equation (1.19) this mode is expected not to contribute to $\underline{u}$ at t_1, and therefore not to solve (1.19). This example proves that fluctuations of optimal growth rate with final time t_1 are non-trivial.

This method is outlined in more details in [119] and an example of its application may be seen in [104]. Figure 1.10, taken from the latter work, shows two peaks for every case, low wavenumber peaks that collapse in inner units and another, significantly weaker peak collapsing in outer units. Both these peaks are associated to streamwise vortices amplified into streamwise streaks through the lift-up (LU) mechanism that will reappear in chapter 3.

1.2.4 Resolvent analysis

The resolvent method is more convenient using a Fourier decomposition in time

$$\underline{q}(\underline{x}, t) = \int_{-\infty}^{\infty} \underline{\hat{q}}(\underline{x}) e^{-i\omega t} \mathrm{d}\omega. \tag{1.20}$$

Then, the previous expression may be injected into equation (1.3), designating the non linear terms as forcing $\underline{\hat{f}}$

$$\begin{cases} -i\omega\underline{\hat{u}} + \underline{\underline{\nabla U}}\;\underline{\hat{u}} + \underline{\underline{\nabla \hat{u}}}\;\underline{U} + \underline{\nabla}\hat{p} - \underline{\nabla}\cdot\left[\left(\underline{\underline{\nabla \hat{u}}} + \underline{\underline{\nabla \hat{u}}}^T\right)/Re\right] = \underline{\hat{f}}, \\ \underline{\nabla}\cdot\underline{\hat{u}} = 0. \end{cases} \tag{1.21}$$

Similarly to GTSA, system (1.21) can be put into matrix form

$$\left(\underline{\underline{L}} - i\omega\,\underline{\underline{M}}\right)\underline{\hat{q}} = \underline{\underline{B}}\,\underline{\hat{f}}. \tag{1.22}$$

Indeed, the operator $\underline{\underline{L}}$ is different from $\underline{\underline{\mathscr{L}}}$ associated to the optimal growth method from equation (1.16) as well as $\underline{\underline{\mathcal{L}}}$ in LSSA from equation (1.11), but is identical to the GTSA operator in equation (1.10).

Define $\underline{\underline{B}}$ the extensor matrix so that

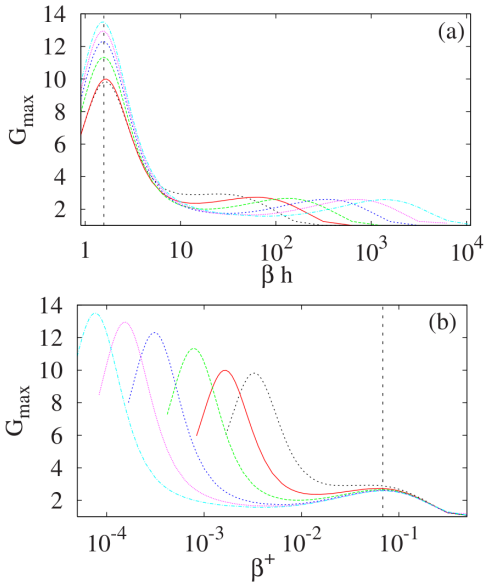

Figure 1.10: Reproduction of figure 2. of [104] concerned with optimal growth of a channel flow of half-height h. Maximum growth rates for streamwise constant perturbations over total calculation time $G_{\max}$ are represented as a function of the spanwise wavenumber for the friction Reynolds numbers $Re_\tau \in \{500, 1000, 2000, 5000, 10000, 20000\}$ (from right to left on plot `(b)`) with a vertical dotted line at the optimal spanwise wavenumber $\beta^+ = 0.0683$. `(a)` and `(b)` differ only in abscissa scaling, the former being in outer and the latter in inner units. See section 2.3.4 for more information on inner scaling.

$$\underline{\underline{B}}\,\hat{\underline{f}} = \begin{bmatrix} \hat{\underline{f}} \\ 0 \end{bmatrix}. \tag{1.23}$$

In this manner, the incompressibility equation remains unforced. Indeed, there are no nonlinear terms there, and strict respect of incompressibility for both baseflow and fluctuations is crucial to flow physics. From relation (1.22) one obtains directly

$$\hat{\underline{q}} = \left(\underline{\underline{L}} - i\omega\,\underline{\underline{M}}\right)^{-1} \underline{\underline{B}}\,\hat{\underline{f}}. \tag{1.24}$$

Introducing extractor $\underline{\underline{H}}$ so that $\underline{\underline{H}}\,\hat{\underline{q}} = \hat{\underline{u}}$, equation (1.24) finally yields

$$\hat{\underline{u}} = \underline{\underline{H}}\left(\underline{\underline{L}} - i\omega\,\underline{\underline{M}}\right)^{-1} \underline{\underline{B}}\,\hat{\underline{f}} \quad \Leftrightarrow \quad \hat{\underline{u}} = \underline{\underline{R}}\,\hat{\underline{f}}. \tag{1.25}$$

The operator on the right-hand side of equation (1.25) is called the resolvent operator as per resolvent formalism, first established by [38] and crucial to modern operator theory. It is also sometimes characterised as a transfer function that linearly associates forcing to response and thus concisely describes the flow system.

Looking at equation (1.25), the reader could be forgiven for being unimpressed. After all, the introduction of unknown forcing terms $\underline{f}$ does little to lift the closure problem and makes the equation overall intractable.

However, that would be missing the main advantage of this method. Strictly speaking, relation (1.25) remains exact. Using Singular Value Decomposition (SVD), which can be thought of as a generalisation of usual operator diagonalisation, it is possible to obtain

$$\underline{\underline{R}} = \sum_i \sigma^{(i)} \underline{\psi}^{(i)} \underline{\phi}^{(i)H}. \tag{1.26}$$

This decomposition provides the three quantities of interest, namely

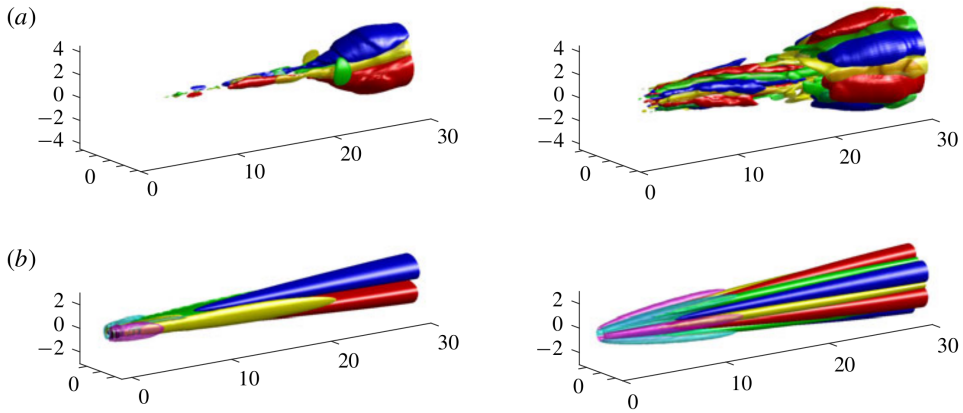

Figure 1.11: Copy of figure 5. of [101] concerned with resolvent analysis of a turbulent jet flow at $Re = 400,000$. On the top (a) are SPOD modes, bottom (b) are resolvent modes at $\omega = 0$. On the left, the $m = 1$ azimuthal decomposition is presented and the $m = 3$ on the right. Red/blue (respectively yellow/green, magenta/cyan) are isosurfaces of $\xi_x^{(1)}$ and $\psi_x^{(1)}$ (resp. $(\nabla \times \xi^{(1)})_x$ and $(\nabla \times \psi^{(1)})_x$, $(\nabla \times \phi^{(1)})_x$). The isosurface level is 25% of maximum and minimum for SPOD modes and response modes, 5% for forcing vorticity at $m = 1$, 15% at $m = 3$, 50% for response vorticity.

1. The gains $\sigma^{(i)}$, which can be understood as a ratio of perturbation kinetic energy obtained over non-linear terms work required to produce them. They are all real positive numbers, which makes it possible to order modes from the most amplified by the linear operator, associated to $\sigma^{(1)}$, to the least amplified.

2. The dominant response mode $\underline{\psi}^{(1)}$ represents the structure which can be expected to arise in the flow fluctuations around the fixed point $\underline{Q}$, provided $\sigma^{(1)} \gg 1$ and $\sigma^{(1)} \gg \sigma^{(2)}$.

3. The optimal forcing mode $\underline{\phi}^{(1)}$ gives the normalised least energetic stimulation that will give rise to $\underline{\psi}^{(1)}$ through the linear operator. It does not correspond to favoured flow behaviour, but may still be useful from an engineering perspective to damp or trigger a specific mode.

This method is fairly modern in the field of fluids mechanics, appearing for the first time in [85] and publicised in [79].

It has been proven in [13, 135] that response modes $\underline{\psi}^{(i)}$ collapse onto Spectral Proper Orthogonal Decomposition (SPOD) modes $\underline{\xi}^{(i)}$ for an infinitesimal resolution. This is significant because any subset of the first SPOD modes is guaranteed to be the most complete representation of the flow energy with regards to the subset dimension. In other words, resolvent analysis provides an accurate representation of the most relevant turbulent fluctuations relative to energy, which is particularly desirable for ROM. This comparison will be revisited in chapter 2. One should note that no similar theoretical link between experiments and linear stability analysis modes obtained by LTSA, LSSA, LSTSA or GTSA.

This important property is illustrated in figure 1.11, where one can see the similarities between the isocontours of $\xi_x^{(1)}$ and $\psi_x^{(1)}$ as well as the modes axial vorticity. Also clearly visible is the formation of streaks, with localised forcing at one end of the domain leading to the formation of long elongated response structures via the LU effect. This will be explored in more details in chapter 3.

Contrary to the previous method, this formalism allows for spatial differentiation of forcing and response. This separation of scales is often crucial for engineering purposes, and a very desirable feature in turbulent flows that are known to be susceptible to multi-scale effects. Indeed, if the method is implemented throughout the domain, it is possible to capture the effect of forcing localised at one end of the domain on response at the other end.

Most authors perform resolvent calculations globally. This leads to the same "readability" problem as above, and led authors such as [101] to also use sensitivity analysis by computing the outer product

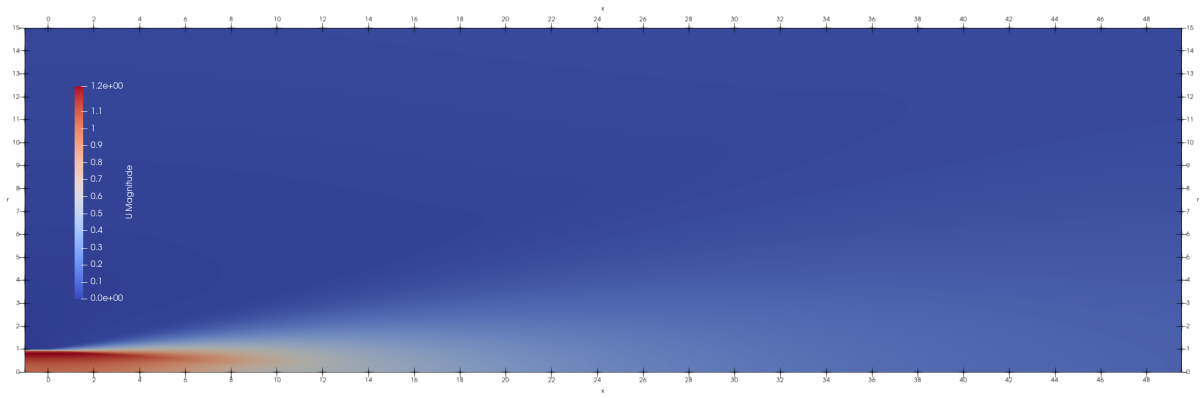

Figure 1.12: Magnitude of the baseflow studied in 3.4.3.

$\underline{\phi}^{(i)}\underline{\psi}^{(i)H}$ and studying regions of overlap between forcing and response component by component. This is relatively straightforward for incompressible flows since $\underline{\psi}^{(1)}$ and $\underline{\phi}^{(1)}$ live on the same space.

1.3 About this work

This thesis was financed throughout by the *Direction Générale de l'Armement* (DGA) of the French Armies Ministry.

1.3.1 Objectives

In this thesis, resolvent analysis is seen as a predictive method - a way to access coherent structures of a turbulent flow given a baseflow.

This thesis will focus on resolvent modes to study coherent structures in turbulent flows. Even though the advent of the resolvent method is a relatively recent happening in the fluids mechanics community, it has led to a great deal of interest and been the subject of several other thesis papers such as [11, 45, 50, 85, 100, 113, 130, 133]. Looking at this impressive list of contributions, it is legitimate to wonder if there remains anything of interest to obtain from this method. The author is convinced this is the case, and hopefully by the end of this manuscript the reader will too.

This thesis aims at two goals:

1. **Improve** resolvent accuracy and relevance at low frequencies,
2. **Investigate** the influence of swirl in a turbulent jet using resolvent analysis.

The first point derives from an observation made in [124], namely that the resolvent method performs significantly better at high frequencies. Therefore, an original idea was explored, which strive to take the resolvent operator to a higher order, using techniques taken from Reynold-Stress Modelling to add the fluctuations correlation tensor $\underline{uu}^T$ to the resolvent state vector.

This idea was directly linked to the next point, as the low-frequency regime is essential for the lift-up effect, which is expected to play an important role in turbulent jets. Therefore, it seemed appropriate to develop a tool that could tackle the regime of interest first.

Resolvent analysis on jets is a recent endeavour, as will be outlined in chapter 3, yet it has nonetheless already enabled notable progress in the field. Swirling jets such as the one displayed in figure 1.12 are known to display new kinds of instabilities with respect to straight jets, and will be the subject of focus in this thesis.

Therefore, this thesis' second objective relates to a more direct application of resolvent analysis to a category of flows where it has not been commonly used. New instability mechanisms such as the centrifugal force are expected to manifest as the swirl increases, and shear instability also present in straight jets is expected to change its shape. The inclusion of a nozzle in the calculations could also bring about changes in the resolvent modes structure.

1.3.2 Outline

This thesis is structured around the two articles produced during my PhD. The first is published at [24] and details an extension of resolvent analysis and its application to channel flow in chapter 2.

The second contribution is a *Theoretical and Computational Fluid Dynamics* draft in chapter 3. At the time of writing, the manuscript has passed the first round of reviewing.

The first publication represents the first year of the PhD and addresses the first objective, the second one is the result of the last two years dealing with the second objective. Both publications are not reproduced *in extenso* and have been adapted to harmonise them with the rest of the manuscript.

These publications contain related literature reviews as well as reproducibility information, but do not delve on the technicalities of the developed code. Chapter 4 will present additional motivation and detail design choices that, while essential to day-to-day work, were not overly influential on scientific conclusions and therefore deemed unworthy of attention in the publications.

Finally, chapter 5 will conclude this thesis.

Chapter 2

A second order resolvent formulation for the analysis of turbulent flow structures

> All models are wrong.
> But some are useful.
>
> *George E. P. Box*

This chapter is an attempt at improving the accuracy of resolvent-based predictions by including velocity correlations in the linear model. Closure assumptions for unresolved nonlinearities are thus pushed back to a higher order. Turbulent channel flow is considered as a test case: response and forcing modes obtained from singular value decomposition of the resolvent model are compared to SPOD modes extracted from a DNS database. The performance of the approach is also measured against previous resolvent-based models. The new model does not yield significant global improvement, but does improve predictions in some regions. Further work on the method should target the linear modeling of the velocity-pressure gradient correlation tensor.

2.1 Literature review

Incompressible turbulent flows are very diverse and cover a broad range of applications. However, they are also notoriously difficult to model. In this work the choice was made to solve the NSE in frequency space instead of approaching time-dependent solutions directly. Here, a novel spectral reduced-order approach to model incompressible turbulent flows will be presented. This method is derived from resolvent modeling with an input from RSMs. The resolvent approach detailed in section 1.2.4 proposes a linear model of a fully turbulent flow at a given frequency. Interpreting nonlinearities in the NSE as a forcing input into the linearized fluctuation equations, the most amplified response structures are taken as a prediction for energetic turbulent flow structures, for instance in [53, 135]. This approach is most often applied in frequency space and comes with all the advantages and drawbacks of a linear model, namely inability to account for all terms, simplicity of implementation, as well as computational efficiency. RSMs originate from a theoretical attempt to improve the quality of RANS models by adding second order terms in the relevant equations as in [103, chapter 11].

Resolvent analysis has already demonstrated its ability to accurately predict large-scale structures in turbulent channel flow at a given frequency; [82] already exposed excellent agreement between DNS data and a combination of twelve resolvent modes with weights derived from an optimisation problem computed at every wavenumber in a spectral framework. This excellent correlation persists throughout the DNS energy spectrum and across the channel without any empirical modeling. Quantifying complexity in the same study clearly shows the main advantage of reduced-order modeling - indeed, the computations involved with the resolvent model are more than three orders of magnitude cheaper than the

relevant DNS, and they nonetheless produce high-quality estimations of the fluctuations. Despite these encouraging results, this approach provides no information on nonlinear terms in the original equations, which can also represent an engineering objective.

Indeed, other authors have given thought to the idea of a low-order modelling of turbulent flows that would be more cost-efficient than DNS - good enough for engineering purposes, and orders of magnitude less expensive. [2] considers a stratified channel flow and prove that on the limited range of scales considered, a resolvent model manages to reproduce an energy budget similar to that of a DNS.

As part of the effort to improve resolvent model performance for wall-bounded flows, [114] apply a decomposition of the velocity field in solenoidal and non-solenoidal parts in the Orr-Sommerfield-Squire (OSS) formulation. Exact Coherent States (ECS) for simple Couette and Poiseuille flows were used to validate the model's performance. An astute method to explicitly compute interaction coefficients as part of an optimisation problem led to a marked increase in performance. A single resolvent mode was demonstrated to accurately represent some ECS solutions. Finally, a characterization of nonlinear terms was performed using the DNS of a channel flow, but stopped at the conclusion that its spectral signature is non trivial. The most important drawback of this approach is that the OSS formulation makes the corresponding nonlinear terms much harder to interpret and model, thus limiting the possibility for further model improvement.

[1] computed SPOD and resolvent modes for a wide range of wavenumbers from a DNS database. That study avoids the use of eddy viscosity and presents large discrepancies between SPOD and resolvent modes. Possible explanations include different physical phenomena which dominate various flow regions, such as the lift-up effect which seems to produce favourable conditions for model and data agreement. Figures 3 and 4 of [1] display the correlation between SPOD and resolvent modes which clearly illustrate the appeal of a new reduced-order method that would be more general than the current state of the art.

[88] present good agreement between a DNS power spectral density (PSD) and a modeled one, using eddy viscosity and a resolvent formalism in a channel flow, as well as an engineered forcing that corresponds better to true flow statistics than white-noise.

More recently, [89] detailed how to obtain a "coloured" forcing term more representative of flow physics. This approach results in a tool with predictive value, though its generality is somewhat lessened by the use of an eddy viscosity model.

[5] present a resolvent-based estimation of turbulent channel flow using wall fluctuations as an input. This work also highlights the importance of "coloured" forcing in the NSE, as white-noise forcing leads to large fluctuations in the logarithmic layer.

Another recent study by [128] stresses how the addition of eddy viscosity makes a significant difference in the resolvent model's ability to properly capture flow energy. Mainly concerned with the latter quantity, [128] outline the balance between production, dissipation, and nonlinear transfer of turbulent fluctuation kinetic energy.

Indeed, the ability of eddy viscosity to improve resolvent models, making it possible to reproduce in such a formalism fine structures close to the wall present in DNS is desirable in channel flows, as stressed by [129]. Although the addition of eddy viscosity makes the resolvent model more robust across wave speeds, the conclusion of [129] is that a scale-dependant eddy viscosity should be considered.

A drawback of resolvent methods listed above is their inability to predict nonlinear terms representative of the real flow. Indeed, the analysis of such a linear operator provides response modes of physical quantities and corresponding optimal forcing terms that represent flow nonlinearities. These forcing terms are obtained according to optimisation relative to the linear operator without regard for flow physics. Therefore, they are not representative of physical flow quantities. In an effort to address this limitation and obtain the "coloured forcing" directly in the new approach, a usual resolvent model for the velocities was coupled with equations for velocity correlations such as to obtain a "second order resolvent model" that would accurately account for both dominant order response and nonlinear terms in the NSE, called forcing terms.

This idea can to some degree be found in the stochastic structure stability theory of [36]. Indeed, this work details how to obtain a linear model for a turbulent mean flow and the associated Reynolds stresses where both evolve in time. [36] acknowledges that for large Reynolds numbers the method becomes highly intractable, preferring instead a reduced order model which uses a few realisations of the fluctuations forced with random white noise to approximate non-linear terms in the mean flow equations as the system becomes large.

Another similar approach goes by the name of generalised quasilinear approximation. This formalism explicitly introduces a range of frequencies that are allowed to interact with one another. [73] explains how this is a generalisation of the quasilinear approach where a single frequency is considered independently of all others. Indeed, in order to close the model, some interactions between waves are cut off from the generalised model. This approach does not always fare well in describing the whole system, but almost always constitutes an improvement compared to the classical quasilinear approximation.

This paper is organised as follows: section 2.2 presents the methodology of usual resolvent analysis as well as the additional equations specific to the new approach, section 2.3 gives more details about the parameter choices and test dataset, section 2.4 presents two linear systems before linking them together, section 2.5 exhibits results across the wavenumber space and details a specific set of parameters. Finally, section 2.6 summarises the study.

2.2 Methodology

This section aims at laying out necessary formalism and equations. Starting from the NSE and a given mean flow, analytical tools to obtain insights into the coherent structures of the flow will be built.

As a side-note, it is accurate to say "mean flow" here because a DNS calculation was used in this case, see section 2.3.4.

The first goal is to obtain a linear system $\underline{u} = \underline{\underline{R}}\,\underline{f}$ which transforms a given forcing $\underline{f}$ representing non-linear terms of the relevant equations into a fluctuation velocity field $\underline{u}$ through a resolvent operator $\underline{\underline{R}}$. The standard approach of defining the linear resolvent operator, as widely applied in the recent literature, is presented in section 2.2.1. The proposition for an extended linear resolvent operator is introduced in section 2.2.2. Subsequently, section 2.2.3 will explain how a linear system can be exploited to obtain its most amplified fluctuations and optimal forcing.

2.2.1 First order

Recall the incompressible perturbations equations 1.3 with $\underline{\underline{\tau}} = \underline{u}\underline{u}^T$, and total derivative defined as $D\underline{u} = \partial_t \underline{u} + \underline{\underline{\nabla u}}\,\underline{U}$

$$\begin{cases} D\underline{u} + \underline{\underline{\nabla U}}\;\underline{u} + \underline{\nabla} p - \frac{1}{Re}\Delta \underline{u} = -\underline{\nabla}\cdot\left(\underline{\underline{\tau}} - \overline{\underline{\underline{\tau}}}\right) \\ \underline{\nabla}\cdot\underline{u} = 0 \end{cases} \Leftrightarrow \left(\partial_t \underline{\underline{M}} + \underline{\underline{L}}_u\right)\underline{q}_u = \begin{bmatrix} \underline{f}_u \\ 0 \end{bmatrix}. \tag{2.1}$$

Since the term $\underline{\nabla}\cdot\left(\underline{\underline{\tau}} - \overline{\underline{\underline{\tau}}}\right)$ is nonlinear in the fluctuation quantities $\underline{q}_u = \left[\underline{u}^T\; p\right]^T$, it may be interpreted as forcing as per [82].

Note that the first line of the linear system (2.1) relates to the incompressibility condition, which is not forced. Resolvent analysis thus circumvents the closure problem by labelling unclosed terms as forcing. Conceptually, one goes from trying to solve for $\underline{q}_u = \left[\underline{u}^T\; p\right]^T$ to looking for coherent structures favoured by the linear operator $\underline{\underline{L}}_u$.

2.2.2 Second order

The key proposition is to model the $\underline{\underline{\tau}}$ tensor, in an attempt to increase the accuracy of the resolvent model. From the second line of (2.1) one obtains

$$\begin{aligned} \left(D - \frac{1}{Re}\Delta\right)\underline{\underline{\tau}} + \underline{\underline{\tau}}\;\underline{\underline{\nabla U}}^T + \underline{\underline{\nabla U}}\;\underline{\underline{\tau}} = &-\underline{u}\underline{\nabla} p^T - \underline{\nabla} p \underline{u}^T - \frac{2}{Re}\left(\underline{\underline{\nabla u}}\right)^T \underline{\underline{\nabla u}} \\ &- \underline{u}\left[\underline{\nabla}\cdot\left(\underline{\underline{\tau}} - \overline{\underline{\underline{\tau}}}\right)\right]^T - \underline{\nabla}\cdot\left(\underline{\underline{\tau}} - \overline{\underline{\underline{\tau}}}\right)\underline{u}^T. \end{aligned} \tag{2.2}$$

The right-hand side of equation (2.2) is considered to be made up of forcing terms denoted $\underline{\underline{f}}$, their common trait being their nonlinearity with respect to $\underline{u}$, p and $\underline{\underline{\tau}}$.

This is not satisfying, as the forcing terms are numerous and known to play an important role in flow physics. [103] details the role of the velocity-pressure gradient tensor $\underline{u}\underline{\nabla} p^T$ especially, which appears critical in redistributing energy amongst perturbation components. It was attempted to model some of

these terms linearly, but to no avail. Inspiration from RSMs as in section 1.1.2 such as [33, 62] did not yield satisfying results. As reported in section 1.1.2, many RSMs such as those reported in [55, 65, 81, 99] are not linear which makes their use limited in this formalism.

Replacing the symmetric $\underline{\underline{f}}$ and $\underline{\underline{\tau}}$ tensors with vectors $\underline{f}^v$ and $\underline{\tau}^v$, which each contains six independent tensor components, equation (2.2) can be cast as a linear system

$$\left(\partial_t \underline{\underline{I}} + \underline{\underline{L}}_\tau\right) \underline{\tau}^v = \underline{f}^v. \tag{2.3}$$

2.2.3 Resolvent analysis

Recall the approach detailed in section 1.2.4, which gives response and forcing modes. This approach can be generalised using $\underline{\underline{B}}$, $\underline{\underline{H}}$ and $\underline{\underline{L}}$ so that $\underline{u} = \underline{\underline{R}}\,\underline{f}$. Specific matrices will be discussed later for the relevant systems.

The SVD of the $\underline{\underline{R}}$ matrix, $\underline{\underline{R}} = \sum_i \sigma^{(i)} \underline{\psi}^{(i)} \underline{\phi}^{(i)H}$, yields $\underline{\phi}^{(1)}$ and $\underline{\psi}^{(1)}$, optimal modes in the sense that they represent the forcing/response pair associated with the highest gain.

This entire process is not new in the case of system (2.1) and has already been performed in [1, 89], amongst others.

2.3 Test case: channel flow

2.3.1 Flow configuration

The specific case of a fully developed channel flow between two infinite plates, separated by a distance $2L_y$ is studied. The presence of viscosity imposes $\underline{u} = \underline{0}$ at both walls. This naturally translates into $\underline{\underline{\tau}} = \underline{\underline{0}}$ at the wall. Even though there is physical motivation to impose additional boundary conditions for $\underline{\underline{\tau}}$, the order of the system prevents the addition of further constraints.

For a wide range of parameters, forcing and response structures are concentrated near the channel walls, with very weak coupling between the top and the bottom halves of the channel. This weak coupling leads to poorly conditioned numerical systems when the full channel height is resolved. To address this problem, following [1], only the half-channel height was resolved, and symmetry conditions imposed at the centre line as follows.

With x streamwise, y wall-normal and z spanwise directions, the mean flow goes as $\underline{U}(x,y,z) = U(y)\underline{e}_x$ with U a function made strictly even across the channel. If u_z is an even (respectively odd) function, and thus symmetric (resp. anti-symmetric) across the channel centre line, then it follows from equation (2.5) that p is an even (resp. odd) function. In turn, this gives odd (resp. even) u_y, and even (resp. odd) u_x.

The parity of the six components of $\underline{\underline{\tau}}$ is constant - $u_x u_y$ and $u_y u_z$ are always odd, $u_x u_z$ is always even, regardless of the parity of u_z. For the sake of conciseness, the present analysis is limited to modes with even u_z, yet it was verified that this choice has little influence on results. Symmetry was enforced *a posteriori*, after DNS calculations and singular value decomposition, as in [1]. In the following sections, only a half-channel was studied.

2.3.2 Fourier transforms

Fourier transforms in space and time for all flow quantities go as

$$q(x,y,z,t) = \hat{q}(y)\exp(ik_x x + ik_z z - i\omega t) \tag{2.4}$$

Note that all terms depending solely on averaged flow quantities disappear through Fourier transform at non-zero wavenumber. This is crucial because the forcing of equation (2.1) becomes $\underline{f}_u = -\underline{\nabla} \cdot \underline{\underline{\tau}}$ and the link with system (2.3) is now apparent.

δ_i^j is taken to be the Kronecker delta and $\mathrm{d}U = \mathrm{d}U/\mathrm{d}y$ the mean flow shear. The condensed notation $F = -i\omega + ik_x U - (\partial_y^2 - k_x^2 - k_z^2)/Re$ is also introduced, so that in the channel flow case, new directional formulations of equations (2.1) and (2.2) are obtained

$$F\hat{u}_j + \mathrm{d}U\delta_j^x\hat{u}_y + ik_x\hat{\tau}_{jx} + \partial_y\hat{\tau}_{jy} + ik_z\hat{\tau}_{jz} + \hat{\partial_j p} = 0, \tag{2.5}$$

$$F\hat{\tau}_{ij} + \mathrm{d}U\left(\delta_i^x\hat{\tau}_{jy} + \delta_j^y\hat{\tau}_{iy}\right) = \hat{f}_{ij}. \tag{2.6}$$

2.3.3 Wall-normal discretisation

Discretisation of the full channel in the wall-normal direction was performed using $n = 129$ Chebyshev–Gauss–Lobatto nodes, with $y = 0$ being the centre of the channel,

$$\forall k \in \mathbb{N}, k \leq n_y,\ y_k = L_y \cos\frac{k\pi}{n}, \tag{2.7}$$

to allow for more points closer to the channel wall. The operator $\underline{\underline{\partial}}_y$ is implemented to spectral order, using Chebyshev polynomials following [109]. A test case for convergence relative to n is detailed in section 2.5.2.

In the following, the notation d will be used to denote operators discretised using this spacing.

One may now compute an integration matrix $\underline{\underline{W}}_d$ so that $\underline{\hat{u}}_d^H\,\underline{\underline{W}}_d\underline{\hat{u}}_d \approx \int_{-L_y}^{L_y}\|\underline{\hat{u}}\|^2(y)\mathrm{d}y$ in the chosen discretisation. Modes computed using the process detailed in section 2.2.3 satisfy

$$\underline{\phi}_d^{(i)H}\underline{\phi}_d^{(j)} = \underline{\psi}_d^{(i)H}\underline{\psi}_d^{(j)} = \delta_j^i, \tag{2.8}$$

so they are orthonormal for an equal spacing discretisation only. This can be corrected as follows.

Using the Cholesky decomposition $\underline{\underline{W}}_d = \underline{\underline{C}}_d^T\,\underline{\underline{C}}_d$, the resolvent is transformed as

$$\underline{\underline{\tilde{R}}}_d = \underline{\underline{C}}_d\,\underline{\underline{R}}_d\,\underline{\underline{C}}_d^{-1}. \tag{2.9}$$

Then one can then take the Singular Value Decomposition (SVD) of the $\underline{\underline{\tilde{R}}}_d$ matrix, $\underline{\underline{\tilde{R}}}_d = \sigma_d^{(i)}\underline{\tilde{\psi}}_d^{(i)}\underline{\tilde{\phi}}_d^{(i)H}$, and obtain the true modes of the system $\underline{\phi}_d^{(i)} = \underline{\underline{C}}_d^{-1}\underline{\tilde{\phi}}_d^{(i)}$ and $\underline{\psi}_d^{(i)} = \underline{\underline{C}}_d^{-1}\underline{\tilde{\psi}}_d^{(i)}$. These new modes are indeed orthonormal with the chosen spacing, $\underline{\phi}_d^{(i)H}\underline{\underline{W}}_d\underline{\phi}_d^{(j)} = \underline{\psi}_d^{(i)H}\underline{\underline{W}}_d\underline{\psi}_d^{(j)} = \delta_j^i$.

2.3.4 DNS dataset

The analysis is based on spectral DNS data of a channel flow. This data was used to extract the time-averaged mean flow and to compute the leading SPOD modes, against which the linear model results will be compared as per [13, 120]. This dataset has been validated in previous studies [1, 89].

Two Reynolds numbers are defined as

$$Re = \frac{U_{bulk}L_y}{\nu} \quad \text{and} \quad Re_\tau = u_\tau Re, \tag{2.10}$$

where U_{bulk} is the mean velocity, L_y is the channel half-width, ν is the kinematic viscosity, and $u_\tau = \sqrt{\max(\mathrm{d}U)/Re}$ is the friction velocity. Inner scalings are further defined as $x^+ = x\cdot u_\tau/\nu$ and $u^+ = u/u_\tau$. Two DNS datasets are used, with ($Re = 2,800$ which gives $Re_\tau = 180$) and ($Re = 10,000$ meaning $Re_\tau = 550$).

The time-wise Fourier transform necessary for SPOD computation was performed using the Welch method with a second order sinusoidal window of size $N = 256$, with 75% overlap. The Welch transform process also featured a force correction to counter the spurious influence of the windowing function established in [76]. More information on chosen DNS parameters can be found in table 2.1, which presents the size of the box in streamwise and spanwise directions L_x and L_z, the grid steps in these directions in inner scaling h_x^+ and h_z^+, as well as the smallest and largest cells in the normal direction $\min h_y^+$ and $\max h_y^+$.

Re_τ	Re	L_x	L_z	h_x^+	h_z^+	$\min h_y^+$	$\max h_y^+$
179	2,800	4π	2π	11.78	5.89	$5.42 \cdot 10^{-2}$	4.42

Table 2.1: Characteristic parameters of the DNS database.

2.4 Final linear systems

In the previous two sections a variety of transformations and hypotheses were described that introduced heavy notation. For the rest of this study, the hat will be removed from all Fourier coefficients (see section 2.3.2), as well as the d (see section 2.3.3) subscript and v (see section 2.2.2) superscript in the interest of clarity.

In this section, the final form of the linear systems of interest in sections 2.4.1 and 2.4.2 will be brought to light. Section 2.4.3 explains the procedure for the comparison between linear model results and leading SPOD modes of the DNS data.

2.4.1 First order

Equation (2.5) can be directly discretised to yield a $4n \times 4n$ discrete system, where $[\mathrm{d}U]_{ij} = \delta^i_j \mathrm{d}U_i$ and $[F]_{ij} = \delta^i_j F_i$,

$$\begin{bmatrix} \underline{\underline{F}} & \underline{\underline{\mathrm{d}U}} & \underline{\underline{0}}_n & ik_x \underline{\underline{I}}_n \\ \underline{\underline{0}}_n & \underline{\underline{F}} & \underline{\underline{0}}_n & \underline{\underline{\partial}}_y \\ \underline{\underline{0}}_n & \underline{\underline{0}}_n & \underline{\underline{F}} & ik_z \underline{\underline{I}}_n \\ ik_x \underline{\underline{I}}_n & \underline{\underline{\partial}}_y & ik_z \underline{\underline{I}}_n & \underline{\underline{0}}_n \end{bmatrix} \begin{bmatrix} \underline{u}_x \\ \underline{u}_y \\ \underline{u}_z \\ \underline{p} \end{bmatrix} = \left(\underline{\underline{L}}_u - i\omega \underline{\underline{M}} \right) \underline{q}_u = \begin{bmatrix} \underline{f}_u \\ \underline{0}_n \end{bmatrix}. \tag{2.11}$$

The extensor $\underline{\underline{B}}_u$ and extractor $\underline{\underline{H}}_u$ operators therefore are non-square identity matrices,

$$\underline{\underline{B}}_u = \begin{bmatrix} \underline{\underline{I}}_{3n} \\ \underline{\underline{0}}_n \end{bmatrix}, \qquad \underline{\underline{H}}_u = \underline{\underline{B}}_u^T. \tag{2.12}$$

So far, this formulation is not novel and appears in [1, 5, 89, 135]. The process detailed in sections 2.2.3 and 2.3.3 yields a resolvent matrix $\underline{\underline{R}}_{1^{\mathrm{rst}}\ \mathrm{order}}$ for the so-called "first order system", as well as associated response modes $\underline{\psi}^{(i)}_{1^{\mathrm{rst}}\ \mathrm{order}}$ and forcing modes $\underline{\phi}^{(i)}_{1^{\mathrm{rst}}\ \mathrm{order}}$.

The currently most successful resolvent-based modelling of energetic coherent structures in channel flow uses a first order formulation (section 2.2.1) with an eddy viscosity model, as argued in [88]. For more information on existing models, please see section 1.1.2. For comparison, the Cess model employed in reference studies [89, 129] was used

$$\frac{\nu_t}{\nu} = \frac{1}{2}\sqrt{1 + \frac{\kappa^2 Re_\tau^2}{9}\left(1-y^2\right)^2\left(1+2y^2\right)^2\left[1-\exp\left(-Re_\tau \frac{1-|y|}{A}\right)\right]^2} - \frac{1}{2}, \tag{2.13}$$

using the friction Reynolds number as defined in equation (2.10). In order to verify that the above model accurately represents the flow dynamics, a comparison between the mean flow computed using the eddy viscosity (as in section 2 of [111]) and the one obtained by DNS was performed. The velocity profiles are compared in figure 2.1. Differences between the two curves exist but remain small.

When applied, this model replaces the molecular diffusion term in equation (2.5), $\Delta \underline{u}/Re$, by a more complete term $\underline{\nabla} \cdot \left[(1+\nu_t/\nu)(\underline{\underline{\nabla u}} + \underline{\underline{\nabla u}}^T)\right]/Re$. This is the resolvent system used by [1, 89], with an eddy viscosity representing at least part of the unknown nonlinear terms. Applying once more the process in sections 2.2.3 and 2.3.3 yields a resolvent matrix $\underline{\underline{R}}_{\mathrm{eddy\ viscosity}}$, as well as associated response modes $\underline{\psi}^{(i)}_{\mathrm{eddy\ viscosity}}$ and forcing modes $\underline{\phi}^{(i)}_{\mathrm{eddy\ viscosity}}$.

2.4.2 Second order

The original proposition in the method is to include equation (2.6) inside a unified resolvent operator that includes velocity, pressure, and $\underline{\tau}$ in the state vector. Recall that the motivation of this study lies

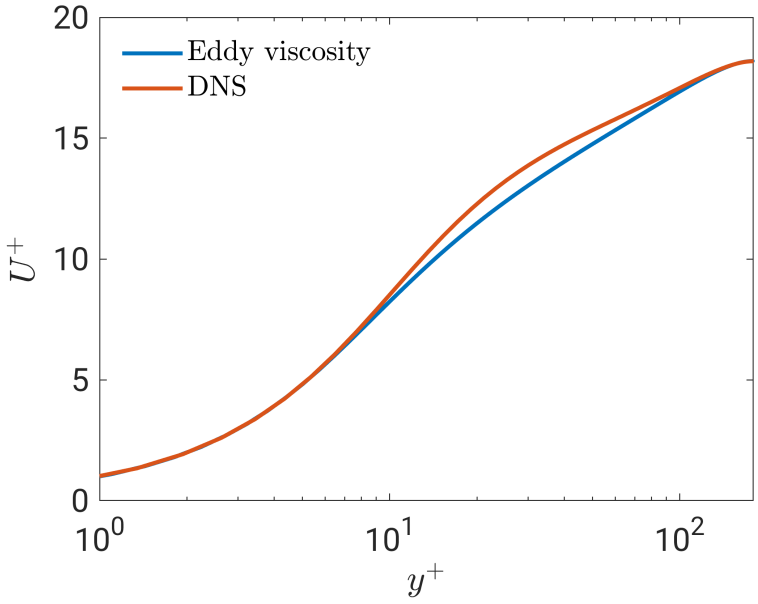

Figure 2.1: Mean velocity profiles from DNS and computed as a steady state with the Cess eddy viscosity model (equation (2.13)).

in improving the capability of the resolvent operator to correctly predict flow physics both in terms of fluctuations and their first moment.

Equation (2.6) translates to a $6n \times 6n$ linear system with the vector notations $\underline{\tau}$ and $\underline{f}$ (see section 2.2.2) written as

$$\left(\underline{\underline{L}}_{\tau} - i\omega\,\underline{\underline{I}}\right)\underline{\tau} = \underline{f}_{\tau}. \tag{2.14}$$

As before, $\underline{f}_{\tau}$ represents the forcing of the second order equations. Together, equations (2.11) and (2.14) form a general system formulation that is $10n \times 10n$ in size,

$$\begin{bmatrix} \underline{\underline{L}}_u - i\omega\,\underline{\underline{M}} & \underline{\underline{A}} \\ \underline{\underline{0}}_{4n} & \underline{\underline{L}}_{\tau} - i\omega\,\underline{\underline{I}} \end{bmatrix} \begin{bmatrix} \underline{q}_u \\ \underline{\tau} \end{bmatrix} = \left(\underline{\underline{L}} - i\omega\,\underline{\underline{\mathcal{M}}}\right)\underline{q} = \begin{bmatrix} \underline{0}_{4n} \\ \underline{f}_{\tau} \end{bmatrix}. \tag{2.15}$$

The equation above makes use of the coupling matrix $\underline{\underline{A}}$ of size $4n \times 6n$ defined as

$$\underline{\underline{A}}\,\underline{q} = \begin{bmatrix} \nabla \cdot \tau \\ \underline{0}_n \end{bmatrix}. \tag{2.16}$$

The extensor $\underline{\underline{B}}$ and extractor $\underline{\underline{H}}$ may be explicitly derived

$$\underline{\underline{B}} = \begin{bmatrix} \underline{\underline{0}}_{4n} \\ \underline{\underline{I}}_{6n} \end{bmatrix}, \qquad \underline{\underline{H}}_u = \begin{bmatrix} \underline{\underline{I}}_{3n} & \underline{\underline{0}}_{7n} \end{bmatrix}. \tag{2.17}$$

The process detailed in sections 2.2.3 and 2.3.3 yields a new resolvent matrix $\underline{\underline{R}}_{2^{\text{nd}}\text{ order}}$, with its associated response modes $\underline{\psi}^{(i)}_{2^{\text{nd}}\text{ order}}$ and forcing modes $\underline{\phi}^{(i)}_{2^{\text{nd}}\text{ order}}$. Note that the latter corresponds to the forcing terms of equation (2.6) instead of those of equation (2.5).

2.4.3 Comparison of model versus data

The process detailed above was implemented in a `Matlab` code version R2019b from [54] using the `svds` or subset singular value decomposition function to obtain resolvent modes.

The most amplified response and forcing modes obtained by the new resolvent model were compared with the most energetic SPOD modes obtained from DNS data. Said SPOD modes are computed using

the method of snapshots, see [120]. This method allows us to obtain SPOD velocity modes, denoted $\underline{\xi}^{(i)}$. The same approach was used to compute SPOD nonlinear modes, denoted $\underline{\zeta}^{(i)}$, obtained directly from the nonlinear term of equation (1.2) in the DNS.

SPOD modes represent the orthonormal basis that captures the most of the flow energy for any given rank, see [135]. They are obtained as eigenvectors of a Cross-Spectral Density (CSD) matrix computed at a given frequency. SPOD may be performed for both velocities and nonlinear terms of the NSE. While the gain-based ranking of the modes gives an indication of each mode's prevalence in the flow, there is no causal association between SPOD nonlinear and forcing modes obtained in this manner. In other words, $\underline{\xi}^{(i)}$ is not related to $\underline{\zeta}^{(i)}$, and both modes are computed independently.

The matrix system detailed in equation (2.15) is exact but the flow response $\underline{q}$ can only be determined if the forcing $\underline{f}_u$ is known. As stated in section 1.2.4, for large gain $\sigma^{(1)}$ and large gain separation $\sigma^{(1)}/\sigma^{(2)}$, it is expected that the first left-singular vector $\underline{\psi}^{(1)}$ approximates $\underline{\xi}^{(1)}$, the actual flow fluctuations obtained from SPOD, as already mentioned in 1.2.4. This has been observed in previous studies such as [1, 89], and the coherent structures in a flow are of engineering and scientific interest by themselves, especially if they are provided by a numerically cheap linear analysis process.

However, as pointed out for instance by Towne et al. [136, section III.c] and by [58], there is no reason why the nonlinear terms in the actual flow $\underline{\zeta}^{(i)}$ should be approximated by the right-singular vectors $\underline{\phi}^{(i)}_{1^{\text{rst}}\text{ order}}$ of the resolvent matrix $\underline{\underline{R}}_{1^{\text{rst}}\text{ order}}$. Indeed $\underline{\zeta}^{(1)}$ represent the best low-rank approximation of flow nonlinear terms, whereas $\underline{\phi}^{(1)}_{1^{\text{rst}}\text{ order}}$ only represents the optimal input to obtain $\underline{\psi}^{(1)}_{1^{\text{rst}}\text{ order}}$ with respect to $\underline{\underline{R}}_{1^{\text{rst}}\text{ order}}$.

Thus, there is no real physical insight to explain why $\underline{\zeta}^{(1)}$ and $\underline{\phi}^{(1)}_{1^{\text{rst}}\text{ order}}$ would have a similar structure, yet it is accurate to say that only the part that is strongly amplified by the linear operator is expected to have an important influence on flow behaviour, as argued in [58]. By contrast, $\underline{\nabla} \cdot \underline{\underline{R}}_\tau \underline{\phi}^{(1)}_{2^{\text{nd}}\text{ order}}$ includes additional physics that might yield a better approximation of $\underline{\zeta}^{(1)}$.

2.5 Results

2.5.1 Parameter space exploration

For a first comparison with results from [1, 89], the agreement between SPOD data and resolvent predictions was measured by varying $\underline{\lambda}^+ = [\lambda_x^+ \ \lambda_z^+]^T$, the $^+$ superscript denoting inner scaling as defined in section 2.3.4. This agreement is quantified in terms of the projection coefficient $\beta = \left|\underline{\psi}^{(1)} \underline{\underline{W}} \underline{\xi}^{(1)H}\right|$, i.e. between first resolvent mode and first SPOD velocity mode. As stated in section 2.4.3, the dominant velocity mode obtained through SPOD from DNS data is compared with the most amplified left-singular vector of the resolvent operator.

Only the $Re_\tau = 180$ ($Re = 2,800$) case will be discussed here, but the $Re_\tau = 550$ ($Re = 10,000$) case was also explored with similar conclusions. Isocontours of β for the range of $\underline{\lambda}^+$ available at the fixed frequency $f^+ = 10^{-2}$ are shown in figure 2.2.

This graph indicates no clear incentive to use the "second order" resolvent model over the first order eddy viscosity resolvent model throughout the $\underline{\lambda}^+$ plane at this frequency. Even though the new model performs slightly better over a restricted area in the low λ_x^+, high λ_z^+ regime, its performance drops everywhere else. The value $f^+ = 10^{-2}$ was chosen as representative of the near-wall cycle, to be consistent with [1].

Results obtained with different frequencies $(10^{-4}, 10^{-3}, 10^{-2}, 10^{-1}, 1)$ show a similar pattern. The isocontours are also shown at $f^+ = 10^{-4}$ in figure 2.3, where one can see that the first order eddy viscosity outperforms the second order resolvent model throughout the domain much like the $f^+ = 10^{-2}$ case.

2.5.2 Near wall structures

In the following, a case study for ($\lambda_x^+ = 1,130$; $\lambda_z^+ = 113$; $c^+ = \omega^+ \lambda_x^+ / 2\pi = 12$) is presented. This choice of parameters corresponds to the "near-wall" case discussed by Morra et al. [89, paragraph 3.1]. Indeed,

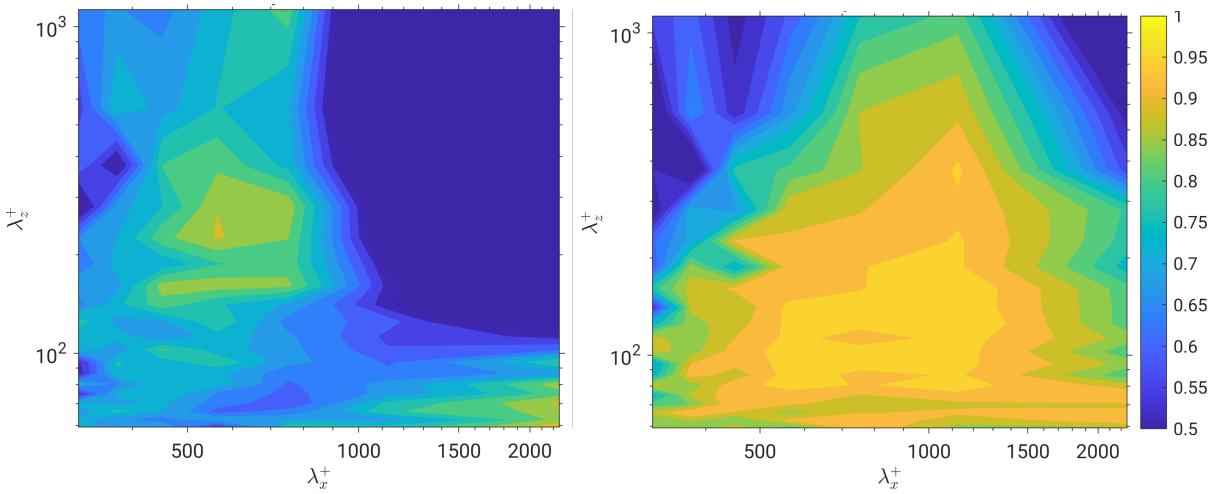

(a) Second order, (b) Eddy viscosity.

Figure 2.2: Projection coefficient of first SPOD mode against resolvent response mode $\beta = \left|\underline{\psi}^{(1)}\, \underline{\underline{W}}\, \underline{\xi}^{(1)H}\right|$ at $(Re; f^+) = (2,800; 10^{-2})$ for a range of wavenumbers $\underline{\lambda}^+$.

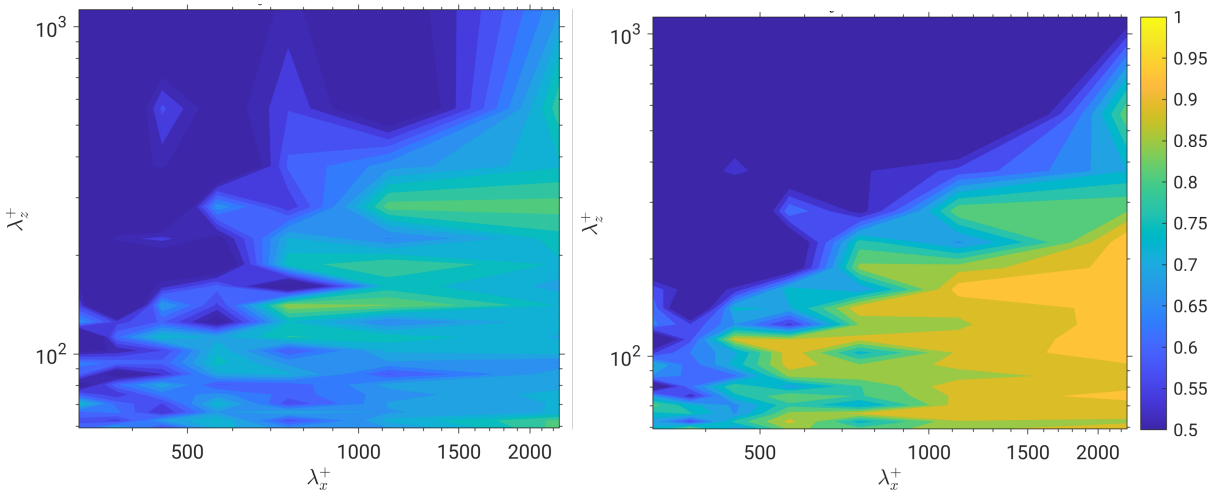

(a) Second order, (b) Eddy viscosity.

Figure 2.3: Projection coefficient of first SPOD mode against resolvent response mode $\beta = \left|\underline{\psi}^{(1)}\, \underline{\underline{W}}\, \underline{\xi}^{(1)H}\right|$ at $(Re; f^+) = (2,800; 10^{-3})$ for a range of wavenumbers $\underline{\lambda}^+$.

these wavenumbers represent a particularly energetic point in frequency space for $y^+ \approx 15$, so relatively close to the wall.

To verify that results are independent of the number of points n, an additional set of calculations at $n = 257$ for the near-wall regime was performed. This calculation using roughly double the y resolution as the one presented below differed by less than 2% from the following results in all aspects. Therefore, results are considered converged with respect to n.

Figure 2.4 shows the absolute value of the first SPOD velocity and resolvent response modes for a variety of models along the three flow directions. It features the "first order model" from section 2.4.1 with and without eddy viscosity, as well as the "second order model" detailed in section 2.4.2. Likewise, figure 2.5 presents the first SPOD nonlinear and resolvent forcing modes for all directions.

As detailed in sections 2.2 and 2.4.3, the modes compared here are the first modes with respect to gain obtained from eigenvalue decomposition of a CSD matrix, and from the SVD of a resolvent matrix for a specific model. There is a noteworthy exception to this, "second order forcing terms" computed as normalised $\underline{\underline{\nabla}} \cdot \underline{\underline{R}}_{\tau} \underline{\phi}^{(1)}_{2^{\text{nd}}\text{ order}}$. Thus, all modes presented below verify $\underline{x}^H \underline{\underline{W}}\, \underline{x} = 1$. As discussed in section 2.3.1, only half a channel was considered, supposing the velocity along z to be even for all modes.

All in all, figure 2.4 yields positive results. In the streamwise direction (figure 2.4a), where the fluctuations are most intense, the "second order" resolvent model succeeds in capturing most of the SPOD mode. The model captures very well close-wall behaviour in this direction with no need for empirical eddy viscosity or wall functions. However, the new resolvent model does tend to underestimate the fluctuation amplitudes in the other two directions (figures 2.4b and 2.4c), performing rather poorly in the spanwise direction, where it smoothens out the flow oscillations to an extreme degree. As in [89], the introduction of an eddy viscosity model greatly improves the performance of the resolvent model (consider the difference between the eddy viscosity and the first order curves).

Figure 2.5 shows that the nonlinear terms of equation (1.2) are better represented overall along the three directions using the second order model than the first order one. This result was to be expected as there is no reason behind writing $\underline{\phi}^{(1)}_{1^{\text{rst}}\text{ order}} \approx \underline{\zeta}^{(1)}$, see section 2.4.3. Notice though that the forcing components in the wall-normal and spanwise directions are strongly underpredicted by the resolvent model. The second order model allows again for an accurate restitution of actual flow statistics close to the wall in the streamwise direction. The capability to predict, to some degree, the properties of the nonlinear terms may be useful to construct estimators, as in [5].

2.5.3 Large scale structures

In this section, the point in parameter space $(\lambda_x; \lambda_z; c^+) = (4.19; 1.26; 16)$ is explored. As before, this choice of parameters and the name of this test case correspond to that of Morra and al. [89, paragraph 3.1]. The denomination "large scale" is inferred from the energetically significant dynamics associated with these wavenumbers, which exhibit structures that span the entire channel. The scaling is identical to the previous section, and only the absolute value of the modes is presented. Figure 2.6 presents the first SPOD velocity and resolvent response modes, whereas figure 2.7 presents the first SPOD nonlinear and resolvent forcing modes.

Overall, this case study yields more mixed results. In two of the three directions, the model performs worse than the basic first order resolvent model or the eddy viscosity system. The new model consistently underestimates real statistics for low y^+, and does not improve predictions compared to the simpler first order model, even in the dominant direction. Worse, the second order model smoothens out variations of velocity amplitude in the spanwise direction. Here again, the addition of an eddy viscosity yields significant improvements in the predictions from the first order resolvent model.

Interestingly, the model overestimates the forcing in the x direction in figure 2.7 and underestimates the rest. In comparison, an eddy viscosity model yields somewhat relevant predictions in the spanwise direction but otherwise fails to capture the dynamics of the nonlinear terms in the flow. Again, this is to be expected, as optimal forcing of the resolvent matrix cannot be expected to correspond to actual flow statistics.

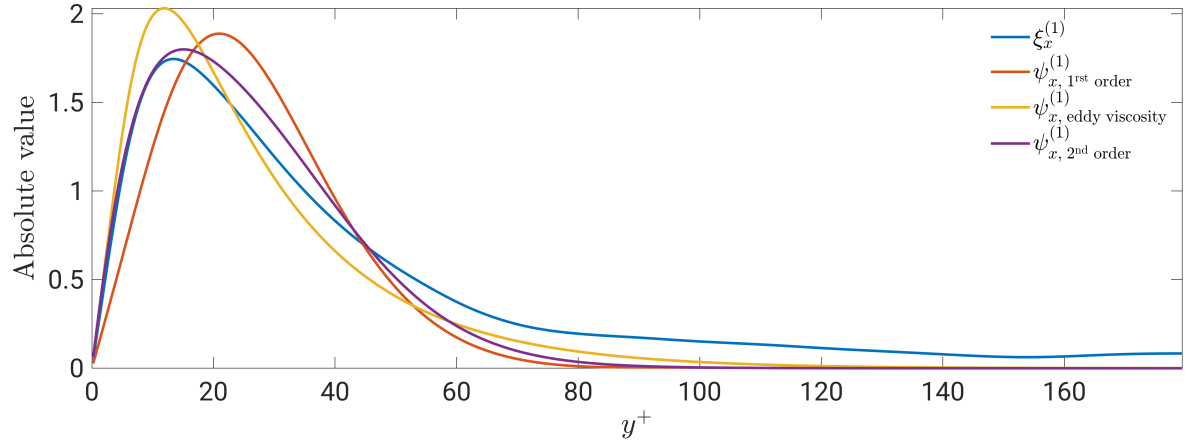

(a) Streamwise component,

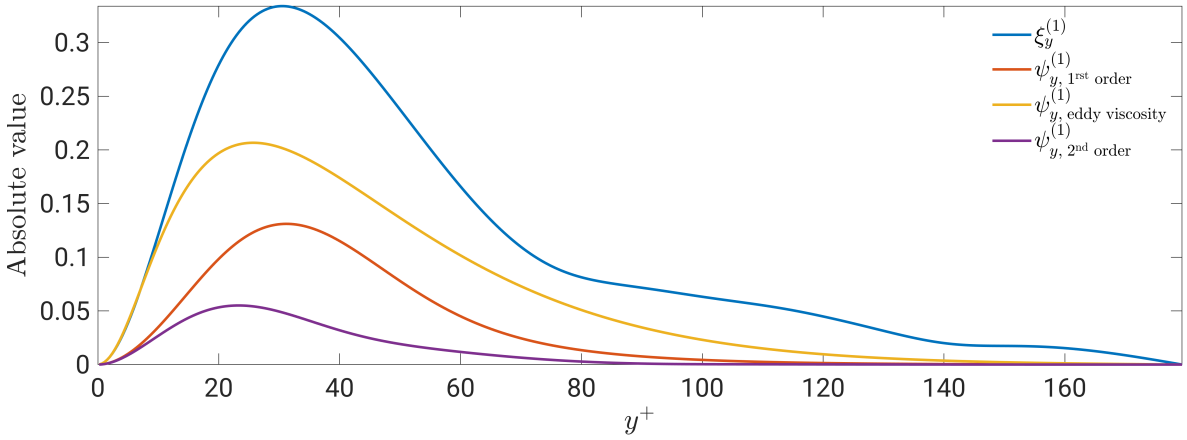

(b) Vertical component,

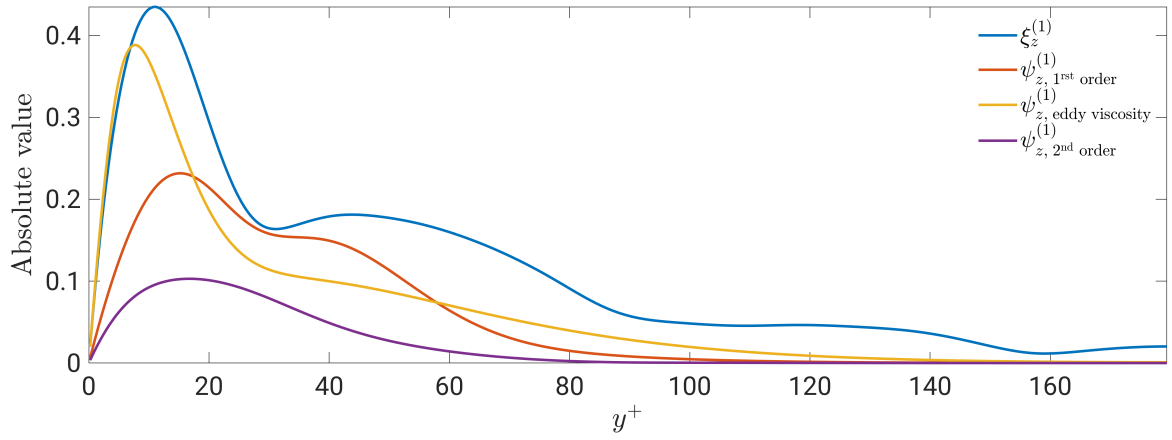

(c) Spanwise component.

Figure 2.4: Comparison between the first SPOD mode of the DNS data $\underline{\xi}^{(1)}$ and predictions from various resolvent models $\underline{\psi}^{(1)}$. Velocity components are shown for $(Re_\tau; \lambda_x^+; \lambda_z^+; c^+) = (180; 1, 130; 113; 12)$.

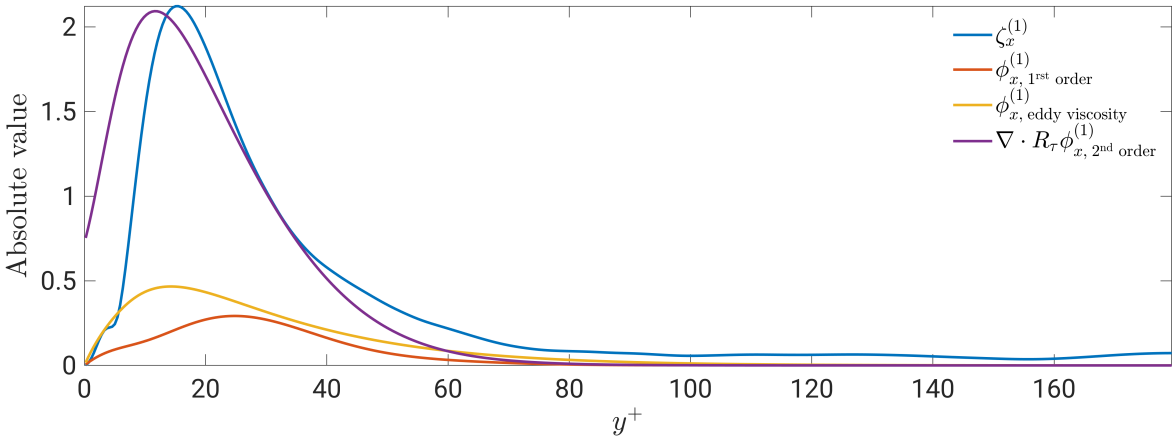

(a) Streamwise component,

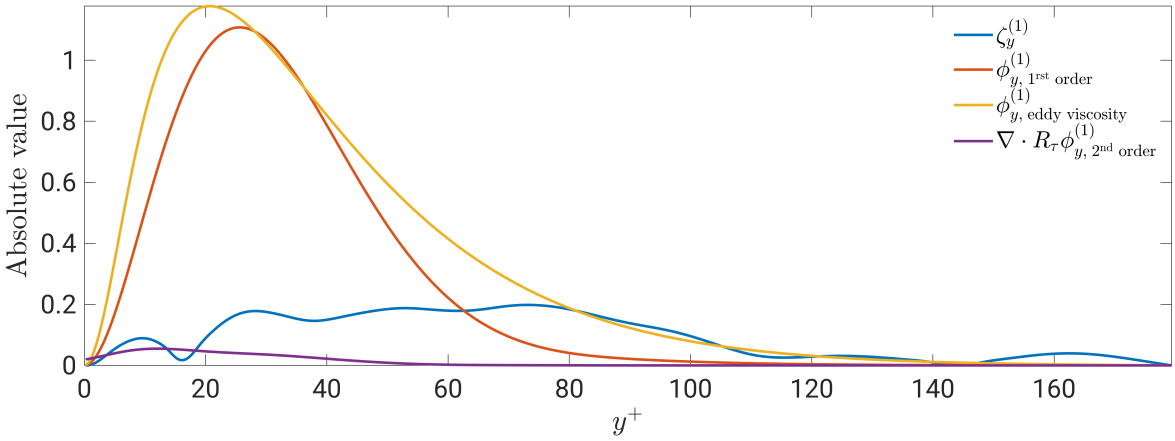

(b) Vertical component,

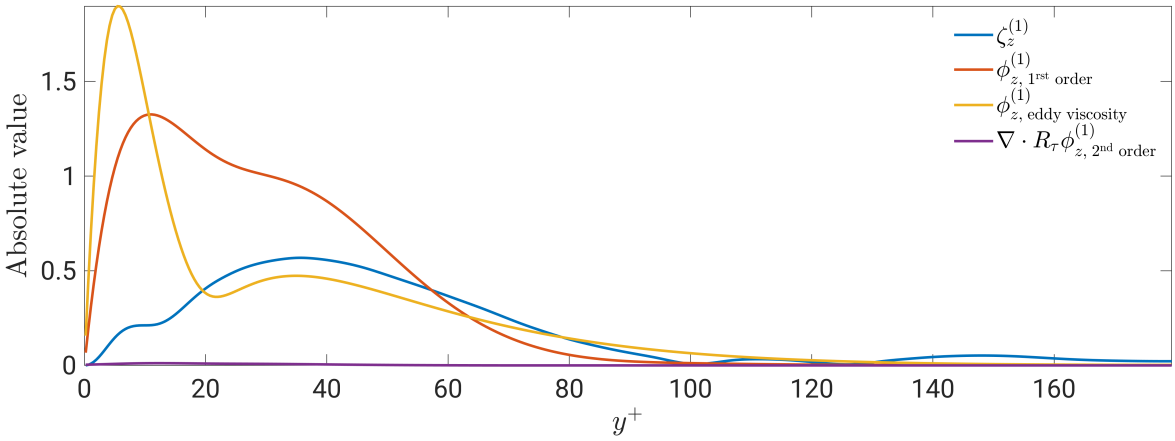

(c) Spanwise component.

Figure 2.5: Comparison between the first SPOD mode of the DNS data $\underline{\zeta}^{(1)}$ and prediction from the second order model $\underline{\nabla} \cdot \underline{\underline{R}}_\tau \underline{\phi}_{2^{\text{nd}}\text{ order}}^{(1)}$. Optimal forcing obtained from first order resolvents are also shown for reference. Nonlinear and forcing components are shown for $(Re_\tau; \lambda_x^+; \lambda_z^+; c^+) = (180; 1, 130; 113; 12)$.

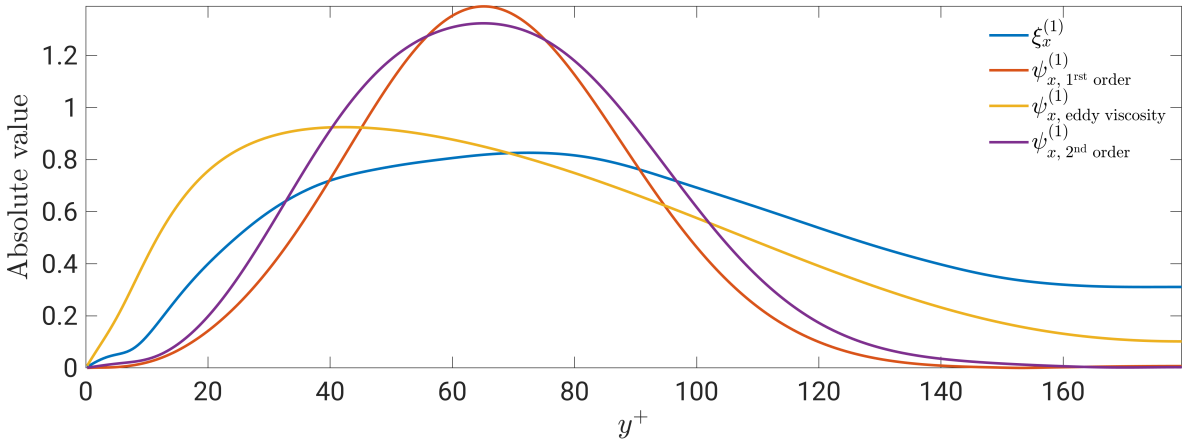

(a) Streamwise component,

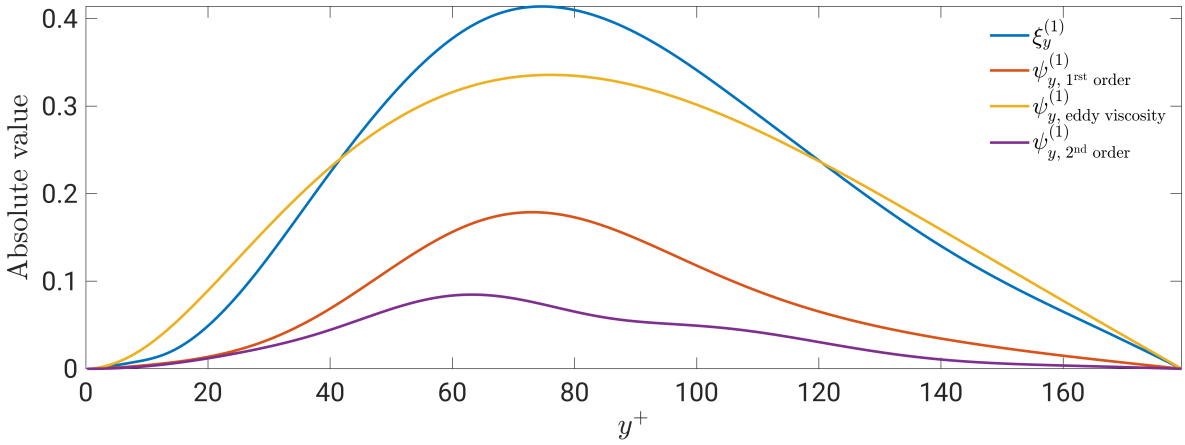

(b) Vertical component,

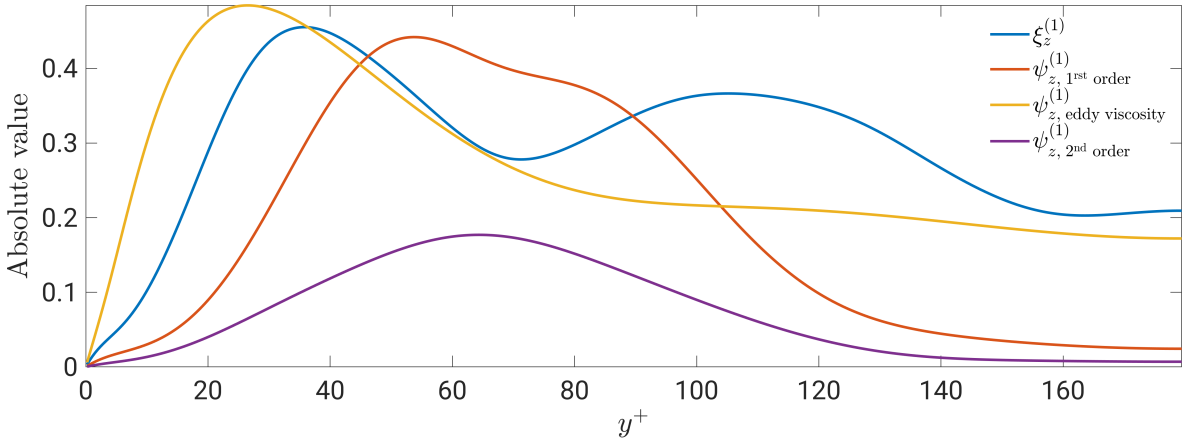

(c) Spanwise component,

Figure 2.6: Comparison between the first SPOD mode of the DNS data $\underline{\xi}^{(1)}$ and predictions from various resolvent models $\underline{\psi}^{(1)}$. Velocity components are shown for $(Re_\tau; \lambda_x; \lambda_z; c^+) = (180; 4.19; 1.26; 16)$.

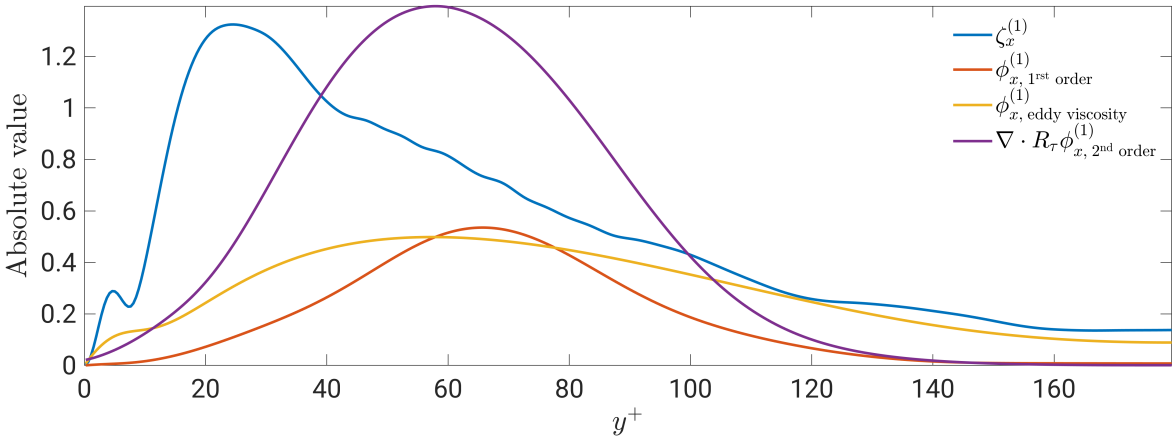

(a) Streamwise component,

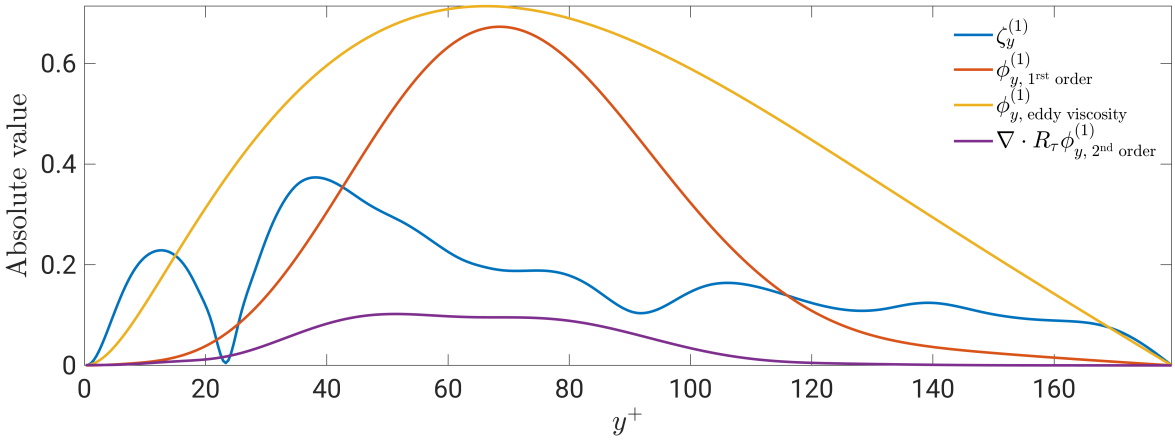

(b) Vertical component,

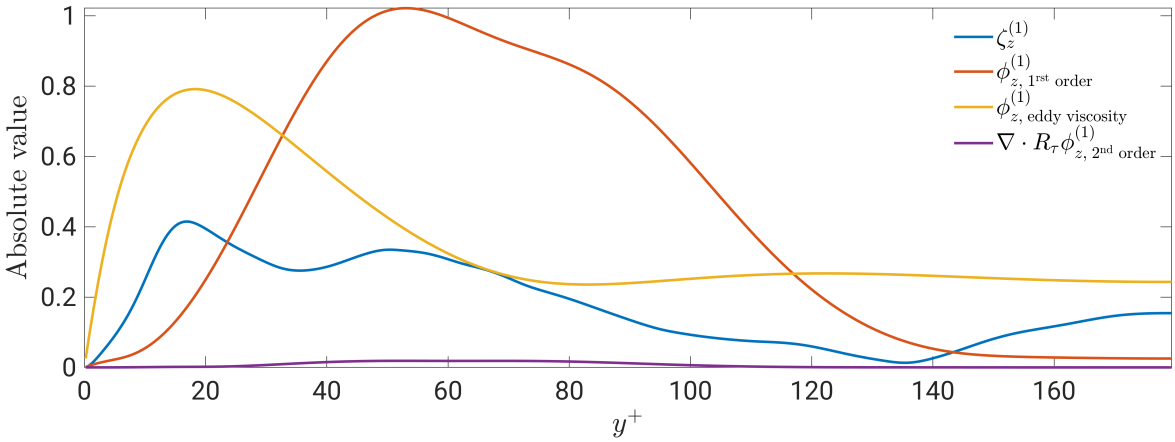

(c) Spanwise component.

Figure 2.7: Comparison between the first SPOD mode of $\underline{\nabla} \cdot \underline{\underline{\tau}}$ in the DNS data $\underline{\zeta}^{(1)}$ and prediction from second order resolvent analysis $\underline{\nabla} \cdot \underline{\underline{R}}_\tau \underline{\phi}^{(1)}$. Optimal forcing obtained from first order resolvents are also shown for reference. Nonlinear and forcing components are shown for $(Re_\tau; \lambda_x; \lambda_z; c^+) = (180; 4.19; 1.26; 16)$.

2.6 Conclusion

The resolvent operator, which relates forcing input of a linear system to the associated response, has been formulated for the Navier-Stokes equations so that the forcing input includes third-order turbulent correlations, which drive a velocity response indirectly via the $\underline{\underline{\tau}}$ tensor. In contrast, classical resolvent analysis, classified as "first order" in this paper, defines forcing input as a substitute for second order correlations, which drive the velocity response directly.

In this study, it was tested whether the shift of forcing to higher order improves the linear response predictions in the case of turbulent plane channel flow. The relevant quantities to compare are the leading SPOD modes extracted from turbulent DNS data, which represent energetic coherent turbulence structures, and the leading SVD modes from the linear resolvent model. In the present case of a flow with streamwise and spanwise invariant statistics, such modes are obtained for a range of wavenumbers for a logarithmic range of frequencies. The reasoning was performed on a half-channel and presented results for an even u_z.

Classical first order resolvent analysis generally yields meaningful predictions of the leading SPOD modes, but leaving much room for improvement in quantitative accuracy. The limiting assumption of this approach is that the nonlinear terms in the fluctuation equations can be replaced by white noise. The currently best available strategy is to use this assumption, in combination with the inclusion of an eddy viscosity in the linear operator.

Much recent discussion in the community revolves around the question of how to improve the predictions further by replacing the white noise with "coloured" noise input. The present approach instead aims to produce the "colour" of $\underline{\nabla} \cdot \underline{\underline{\tau}}$ by computing the $\underline{\underline{\tau}}$ in a spectral setting as a response to forcing at a higher order. If one assumes that in a real flow, forcing of equations 2.6 follows some kind of white noise law, this formalism could predict with some accuracy non-linear terms of RANS using the resolvent method.

The success of this strategy, as far as it has been possible to establish, is not as clear as might have been hoped. Streamwise velocity fluctuation amplitudes are very well predicted in a "near-wall" setting in the sense of [1, 89], and the streamwise component of $\underline{\nabla} \cdot \underline{\underline{\tau}}$ obtained from the model also compares well to the corresponding SPOD mode from the DNS. On the other hand, wall-normal as well as spanwise velocity fluctuations and $\underline{\nabla} \cdot \underline{\underline{\tau}}$ amplitudes are strongly underpredicted. In the "large-scale" setting in the sense of [1, 89], the second order model clearly gives less accurate results than the standard first order resolvent, especially when eddy viscosity is included in the latter.

This observation stands even if an imperfect eddy viscosity model is used, namely one that produces a different mean flow from the DNS. Worse, this behaviour is consistent throughout the frequency space and the two Reynolds numbers explored. When the model performance is measured in terms of projection with SPOD modes throughout the parameter space, the second order model cannot compete with the first order model with eddy viscosity.

The roadblock to accurate second order resolvent modelling is a typical closure problem, which could be caused by the velocity-pressure-gradient correlation detailed in section 2.2.1. Efforts to cast this tensor in the form of a linear function of $\underline{u}$, p or $\underline{\underline{\tau}}$, so that it could be incorporated into the resolvent operator, have not been fruitful.

As such, the present study represents a first step in a new direction for improved resolvent analysis applied to turbulent flow, from where new paths are hoped to emerge. It is possible that this method proves more promising in another geometry or at Reynolds number higher than the maximum explored $Re_\tau = 550$.

Chapter 3

Resolvent analysis on a swirling turbulent jet

Et pourtant, elle tourne !

Galileo Galilei

This study aims at exploring coherent structures in swirling turbulent jets. A stationary axisymmetric turbulent baseflow was obtained for $Re = 200,000$ using the SA eddy-viscosity model and an open source computational fluid dynamics code. The same eddy-viscosity field was included inside the fluctuation equations in an effort to improve accuracy of the resolvent method. These fluctuations were then solved using resolvent analysis, using only the first mode to approximate the most amplified response and optimal forcing. Several configurations were studied, going gradually from a baseflow with no azimuthal velocity to one with comparable axial and azimuthal components. Double spiral counter-rotating but co-winding modes are found to exhibit spectacular amplification at low frequency, to the point that their gains overtook those of modes associated with the Kelvin-Helmholtz (KH) mechanism. This behaviour is explained as lift-up (LU) and something more that is not KH. This was done by comparing the alignment of the mode wavevector with regards to principal shear, using the so-called dot criterion. Another phenomenon of interest at low frequencies is the development of structures atop the finite-height nozzle included in the calculations, with is shown to be related to the lift-up effect and jet entrainment.

3.1 Literature review

3.1.1 Straight jet amplification mechanisms

Using resolvent analysis, [101] has been able to describe the fluctuations that arise from a turbulent baseflow taken out of the LES of [121, section 2]. The resolvent modes computed with an eddy-viscosity model compare well to SPOD modes extracted from the data, in line with section 1.2.4.

The authors introduced a notion of sensitivity by inspecting correlations between components of forcing and response throughout the domain. This tool enabled the differentiation between several amplifying mechanisms, namely Orr, LU, and KH. [101] provides a mapping to where each phenomenon is expected to dominate throughout the frequency space.

Kelvin-Helmholtz

Literature on KH mechanism and associated instabilities dates back to [108]. This mechanism may be illustrated in figure 3.2 for a parallel two-dimensional inviscid flow and motivated as in [39, section B.2]. Suppose the flow to be potential on both sides of an interface featuring a point jump of velocity $2U$. Consider a reference frame moving at the mean of the two layers, in which the interface is steady. Further assume a perturbation along the jump line of wavelength λ and amplitude $\mathcal{A}$.

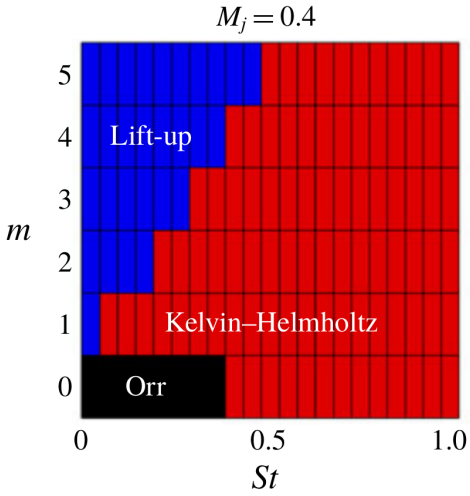

Figure 3.1: Extract of figure 13 of [101], concerned with the study of a $Re = 400,000$ straight weakly compressible $Ma = 0.4$ jet. proposing a mechanism map as a function of Strouhal number St and azimuthal wavenumber m.

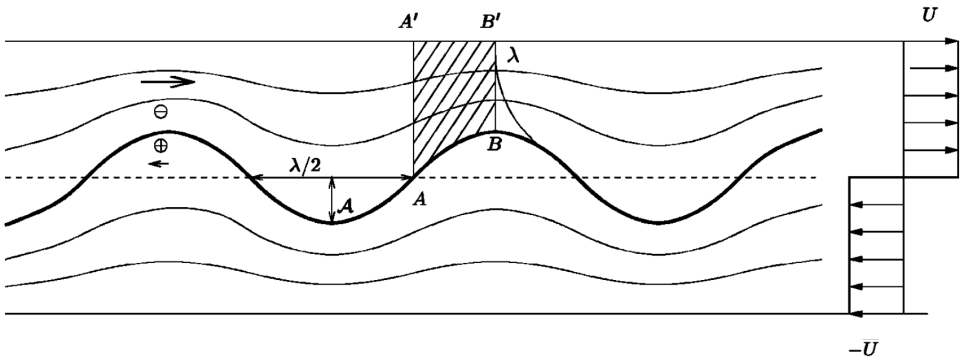

Figure 3.2: Figure 3 of [39], illustrating the KH mechanism for a 2D parallel flow.

Given the previous assumptions, the situation is perfectly symmetrical on either side of the interface, and so only the top part will be considered. Now consider a point A at the average interface height, then a point B at a distance $\lambda/4$. Because the fluid is irrotational, the perturbation is expected to vanish away from the interface like $e^{-y/\lambda}$. Since A was taken at a point where the surface is unperturbed, we can write $\mathtt{q}_A = Q$. By contrast, $\mathtt{q}_B = Q + q$. Supposing an infinite domain, one may project A and B into A' and B' at a very large distance L away from the interface where the effects of the perturbations have all but vanished and streamlines are straight one more.

Using Bernouilli's theorem between A and B without gravity for dimensionless quantities gives

$$\begin{aligned}
\frac{\mathtt{u}_A^2}{2} + \mathtt{p}_A &= \frac{\mathtt{u}_B^2}{2} + \mathtt{p}_B, \\
\Leftrightarrow \mathtt{p}_A - \mathtt{p}_B &= \frac{1}{2}(\mathtt{u}_B^2 - \mathtt{u}_A^2), \\
\Leftrightarrow -p &= Uu + \frac{u^2}{2}, \\
\Leftrightarrow p &= -Uu + O(u^2)
\end{aligned} \tag{3.1}$$

Because of incompressibility, symmetry, and assuming $\mathcal{A} \ll \lambda \ll L$ one can use conservation of mass to write

$$\begin{aligned}
\int_0^{L+\mathcal{A}} \mathtt{u}(x_A, y)\mathrm{d}y &= \int_0^L \mathtt{u}(x_B, \mathcal{A} + y)\mathrm{d}y, \\
\Leftrightarrow u\int_{\mathcal{A}}^L e^{-y/\lambda}\mathrm{d}y &= U\int_0^{\mathcal{A}} \mathrm{d}y, \\
\Leftrightarrow u\left[-\lambda e^{-y/\lambda}\right]_{\mathcal{A}}^L &= U\mathcal{A}, \\
\Leftrightarrow u\left[1 - \frac{\mathcal{A}}{\lambda} + O\left(\frac{1}{\lambda^2}\right)\right] &= \frac{\mathcal{A}}{\lambda}U.
\end{aligned} \tag{3.2}$$

Taken together, equations (3.1) and (3.2) give

$$\left.\begin{array}{rcl} p & \approx & -Uu \\ u & \approx & \left(1 - \frac{\mathcal{A}}{\lambda}\right)^{-1} \frac{\mathcal{A}}{\lambda}U \end{array}\right\} \Rightarrow p \approx -\left(1 - \frac{\mathcal{A}}{\lambda}\right)^{-1} \frac{\mathcal{A}}{\lambda}U^2. \tag{3.3}$$

This explains the growth of the mode. Indeed, the decrease in pressure at B is associated to an increase below the interface by symmetry, which drives vertical flow at B normal to the jump interface, causing a rise in $\mathcal{A}$. A more formal derivation of the amplification mechanism may be found in [31, section 1.4], also in the case of a velocity jump.

At the dawn of the twentieth century, [108] studied cylindrical flows using LTSA, as presented in section 1.2.2 and famously established that for a two dimensional flow, the absence of an inflexion point $\underline{x}_0$ in the baseflow that would satisfy $\partial_y^2 U_x(\underline{x}_0) = 0$ is a necessary condition for stability.

It was generalised in the azimuthal direction by [12], where an instability growing simultaneously on radial shear in the axial and azimuthal directions was proposed. This is the favoured mechanism in [39, section B.3] for instability growth by LTSA on a plug round jet at high wavenumbers in an inviscid flow, even after introducing swirl. However, the authors acknowledge that the use of an infinitesimal flow profile such as the one proposed in that work is known to lead to nonphysical KH solutions that would be damped by viscosity in a real flow.

Orr mechanism

This phenomena exploits shear by creating structures tilted against baseflow shear that grow as they are straightened. This phenomena is explained in [22] by considering a parallel baseflow in two-dimensions $\underline{U}(\underline{x}) = U(y)\underline{e}_x$. From there and following section 1.2.2, perturbations are considered in a two-dimensional local framework, with $q(x, y) = \hat{q}(y)e^{ik_x x} + \hat{q}^*(y)e^{-ik_x x}$. Going back to the first equation of (1.3) and neglecting the right-hand side as well as setting $\nu = 0$ gives

$$\partial_t \hat{u}_x + U'\hat{u}_y + iUk_x\hat{u}_x + ik_x\hat{p} = 0, \tag{3.4}$$
$$\partial_t \hat{u}_y + iUk_x\hat{u}_y + \partial_y\hat{p} = 0, \tag{3.5}$$
$$ik_x\hat{u}_x + \partial_y\hat{u}_y = 0. \tag{3.6}$$

This system multiplied on the left hand side by $\underline{u}^T$ yields the Reynolds-Orr equation representing fluctuation energy evolution in time. Assuming a wall on one boundary, $\underline{u} \underset{y\to\infty}{\longrightarrow} \underline{0}$ gives

$$\begin{aligned}
&\partial_t \left\|\underline{\hat{u}}\right\|^2 + U'\hat{u}_x\hat{u}_y + iUk_x \left\|\underline{\hat{u}}\right\|^2 + ik_x\hat{u}_x\hat{p} + \hat{u}_y\partial_y\hat{p} = 0,\\
\Rightarrow\ &\partial_t \int_0^\infty \left\|\underline{\hat{u}}\right\|^2 \mathrm{d}y + \int_0^\infty U'\hat{u}_x\hat{u}_y\mathrm{d}y + i\int_0^\infty Uk_x \left\|\underline{\hat{u}}\right\|^2 \mathrm{d}y + ik_x\int_0^\infty \hat{u}_x\hat{p}\mathrm{d}y + \int_0^\infty \hat{u}_y\partial_y\hat{p}\mathrm{d}y = 0,\\
\Rightarrow\ &\partial_t E + \frac{1}{2}\int_0^\infty U'\hat{u}_x\hat{u}_y\mathrm{d}y + \frac{i}{2}\int_0^\infty Uk_x \left\|\underline{\hat{u}}\right\|^2 \mathrm{d}y + \frac{1}{2}\left[\hat{p}\hat{u}_y\right]_0^\infty + \frac{1}{2}\int_0^\infty \hat{p}(ik_x\hat{u}_x - \partial_y\hat{u}_y)\mathrm{d}y = 0,\\
&\Rightarrow \Re\int_0^\infty \hat{p}\partial_y\hat{u}_y\mathrm{d}y - \frac{1}{2}\Re\int_0^\infty U'\hat{u}_x\hat{u}_y\mathrm{d}y = \partial_t E.
\end{aligned}$$

This shows the perturbation energy density E can increase if $\Re(\hat{u}_x\hat{u}_y) < 0$ assuming $U' > 0$. That is the definition of a structure tilted against the flow shear. By contrast, a structure tilted with the flow shear would have $\hat{u}_x\hat{u}_y > 0$.

Figure 3.3 illustrates how this mechanism leads to optimal growth for short time, with structures tilted against the shear growing as they are straightened, and then decay as they become tilted in the same direction as the shear.

Lift-up

By contrast with the two previous amplification mechanisms, LU cannot be understood with a purely two-dimensional approach. LU is another shear amplification mechanism that manifests as rolls producing streaks. It was exhibited in [34], also considering a parallel baseflow $\underline{U} = U(y)\underline{e}_x$, but assuming the perturbations $\underline{q}(y,z)$ do not depend on x. This mechanism is also inviscid, leading to equations

$$\partial_t u_x + U'u_y = 0, \tag{3.7}$$
$$\partial_t u_y + \partial_y p = 0, \tag{3.8}$$
$$\partial_t u_z + \partial_z p = 0. \tag{3.9}$$

It is possible to introduce a streamfunction φ so that $u_y = -\partial_z\varphi$ and $u_z = \partial_y\varphi$. Derivating (3.8) with respect to z and (3.9) with respect to to y, then substracting one from the other eliminates pressure and gives

$$\partial_t\Delta\varphi = 0. \tag{3.10}$$

Equation (3.10) means that it is possible to have a solution for stationary φ, which would lead to a time-invariant u_y. Assuming this, relation (3.7) may be integrated in time $u = u_0 - u_yU't$. This shows it is possible to create linear instability growth with these simple perturbations, for instance by picking $\varphi = A\sin(k_yy)\sin(k_zz)$, which leads to closed, steady streamlines. In such a configuration, fluid is alternatively picked up from fast baseflow regions to be pulled down into slow regions, or conversely lifted up from slow regions into fast ones, hence the name lift-up. LU is therefore all about vertical convection that induces large streamwise streaks.

3.1.2 Rotating jet instabilities

[42, 59, 60, 71, 72, 75] have all conducted LTSA, LSSA or LSTSA analysis of swirling flows at zero to moderate Reynolds number. These authors all took a prescribed parallel baseflow sometimes as simple

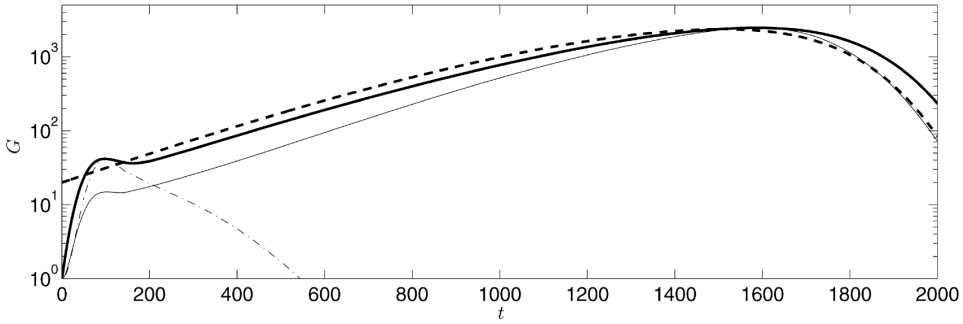

(a) Figure 6 showing envelopes of maximal energy growth G for different initial conditions. Of most interest is the thin-dotted line which show actual energy evolution when initialising the flow system with structures leading to maximum growth at time $t = 98$,

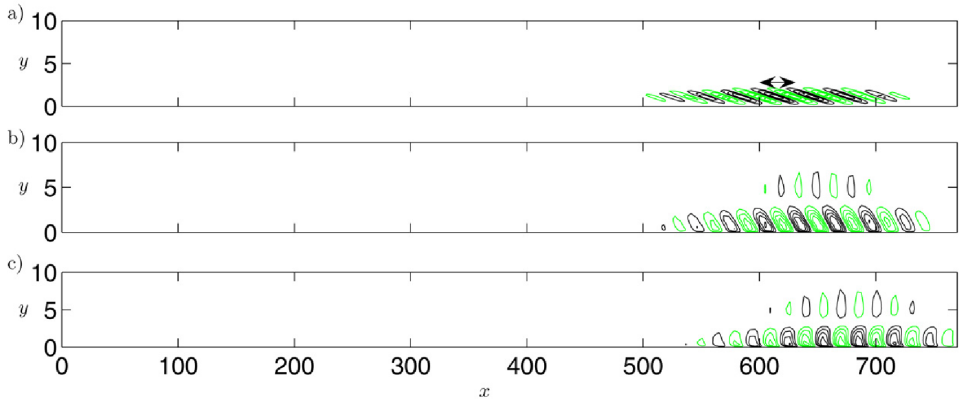

(b) Figure 8 showing the time evolution of streamwise velocity. `a)` $t = 0$, `b)` $t = 50$, `c)` $t = 98$.

Figure 3.3: Illustrations from [3], applying the optimal growth technique discussed in section 1.2.3 to a boundary layer at $Re = 1,000$, which highlights the Orr mechanism at short times.

as a plug flow then derived dispersion relations analytically or numerically. This has the advantage of readily supplying growth rates, modes, as well as physical motivation for them.

In the case of [105], the focus was on the Grabowski-Berger vortex, detailed in section 4.4.1. In the high swirl regime after the apparition of the vortex breakdown bubble, Qadri et al. used GTSA along a sensitivity analysis to bring to light two regions of the bubble where perturbations are most amplified. Just ahead of the bubble, radial and azimuthal perturbations are amplified, and around it, strong shear causes a KH type mechanism. The fact that this publication highlights two different mechanisms operating at the same time using GTSA contrasts with tradition non-swirling jet analysis where a single mechanism is often sufficient to explain the observed amplification.

[42] stands out by exploiting the equivalence between the fluctuations impulse response and the Briggs-Bers pinching criterion detailed in section 1.2.2, albeit in a parallel flow framework. This study highlights the special role of a region upstream of the recirculation bubble which serves as a wavemaker for an absolutely unstable double helix mode.

[71] performed LSTSA and additionally plotted critical curves where the transition from convective to absolute instability takes place depending on co-flow and swirl intensity for every azimuthal wavenumber. In turn, this allowed him to single out the most unstable azimuthal wavenumbers for a given co-flow as the first one transitioning into absolute instability when increasing swirl.

[72] and [60] studied the interplay between swirl and compressibility using LSSA and LTSA respectively, finding swirl to be more destabilising than compressibility is stabilising.

[59] also introduced viscosity and discovered additional types of viscous instabilities, again using LTSA. Furthermore, this work compared the modes obtained numerically to experiments and demonstrated satisfying agreement for a range of frequencies.

The different authors cited here disagree on which mode is more unstable when introducing swirl, but this is not surprising as the baseflows considered also differ. [71] argues in favour of the axisymmetric mode, [105] support a bending mode, whereas [42, 59, 60, 72, 75] claim it to be a spiral mode.

The swirling jet problem was also addressed formally in a LSTSA framework in [39], again for a plug flow. This approach has the advantage of being purely analytical, thus allowing a clear separation of the different terms driving instabilities. In turn, this enabled the authors to highlight four separate mechanisms, namely inertial waves, C, axial and azimuthal KH. However, this study acknowledges that its baseflow is non physical because of its infinitely thin shear layer. This leads to unbounded amplification of KH instabilities with wavenumber, and to a damping of C instabilities.

More recently, the work of [80] studied a Grabowski-Berger vortex using GTSA. Performed at very low Reynolds number in a decidedly laminar regime, the analysis captures the phenomenon of recirculation, as well as flow instability at high swirl. Furthermore, this analysis studied in detail flow behaviour prior to vortex breakdown, highlighting the importance of spiral and double spiral modes in the breakdown process. Through studies of the associated Hopf bifurcation, this paper managed to reproduce behaviour obtained in Direct Numerical Simulations, most notably a range of swirl intensity where the fluctuation display hysteresis.

Another study of interest is [30], where coherent structures are obtained in a laminar jet using numerical bifurcation analysis, going above and beyond critical swirl to study vortex breakdown. In this study, similarly to [44] discussed in section 4.4.3, the computational domain had a wall on top of the nozzle. and is not concerned with quantifying gain, yet it does study vortex breakdown as a Hopf bifurcation that happens first for single or double helix type structures.

In recent years, interest on linear modelling of turbulent jets has steadily increased as numerical capabilities have evolved, allowing for computations with ever increasing Reynolds number as well as global analysis on previously inaccessible scales. The closest study to this one would be [86], which used resolvent analysis on a coaxial swirling jet. The key difference between this work and the present study are geometry and Reynolds number considered. The former is fully turbulent, whereas the latter was decidedly laminar.

Centrifugal

When considering rotating flows, C instabilities come into play. [39] outlines the driving force behind this type of flows by considering a plug round parallel flow in solid body rotation of angular velocity S and radius R amidst a flow at rest in the long wavenumber limit.

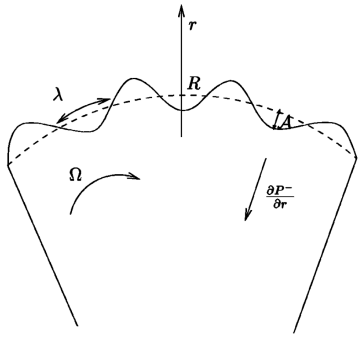

Figure 3.4: Figure 5 of [39], illustrating the C mechanism for a parallel solid core rotation.

Inside the rotating core, the centrifugal force reads $\underline{F}_S = S^2 r \underline{e}_r$. Close to the interface, it is compensated by an equal and opposite pressure gradient $\partial_r P(R^-)$. In general, such a radial pressure gradient also exists outside the core, but in this ideal scenario it goes to zero immediately after the velocity jump.

A particle displaced along $\underline{e}_r$ from inside the core R^- to the outside R^+ conserves its angular momentum due to the absence of viscosity. It is therefore subjected to a higher centrifugal force as r increases, but to a much lower pressure gradient as $\partial_r P(R^+) = 0$. Conversely, a fluid particle pulled from the outside in has insufficient angular momentum to grant it a centrifugal force that would keep it away from the axis, yet it becomes subject to a strong pressure gradient $\partial_r P(R^-)$. This phenomenon is illustrated in figure 3.4.

[107] derived what became known as the Rayleigh criterion in the case of parallel flow with no axial component. This criterion goes that the existence of a radius where $\partial_r(r^2 U_\theta^2) < 0$ is a necessary condition for axisymmetric C amplification. In [131], this criterion was found to be sufficient for the case of Couette flows. It was generalised for a non-uniform axial flow in [41].

A generalised criterion for axially and azimuthally decomposed fluctuations

$$q(x, r, \theta) = \hat{q}(r) e^{i(kx+m\theta)} + \hat{q}^*(r) e^{-i(kx+m\theta)} \tag{3.11}$$

with azimuthal wavenumber $m \neq 0$ was further derived in [51, section 3]. This paper established a sufficient condition for stability as

$$\forall \underline{x} \in V | k^2 \frac{\partial_r(r^2 U_\theta^2)}{r^3} - \frac{2km}{r^2} U_r \partial_r U_x - \frac{\left[k\partial_r U_x + m\partial_r(U_\theta/r)\right]^2}{4} \geq 0. \tag{3.12}$$

[66] argued this criterion is too restrictive and derived a simpler sufficient criterion for instability in the infinitely large wavenumber limit which reads

$$\forall \underline{x} \in V | U_\theta \partial_r \left(\frac{U_\theta}{r}\right) \left[\partial_r(rU_\theta)\partial_r\left(\frac{U_\theta}{r}\right) + (\partial_r U_x)^2\right] < 0. \tag{3.13}$$

[35] proved later that the criterion from equation (3.13) was linked to C instability by considering a coordinate system turning with the fluid, writing associated inertial effects, and falling back on [66]'s criterion. More recently, further generalisation was performed in [17] and finally in [16, equation (3.25)] for a wider range of profiles and at a higher order. [16, 17, 35, 51, 66, 107, 131] all used generic flow profiles in inviscid LTSA as presented in section 1.2.2.

Inertial waves

Also called Kelvin waves, inertial are associated to Coriolis forces. As derived in [90], consider a two-dimensional baseflow in uniform solid rotation at angular velocity S around axis $\underline{e}_w$, assume perturbations independent of x, and write their momentum equation (1.3) in the rotating frame

$$\partial_t \underline{u} + \underline{\nabla}\tilde{p} + 2S\underline{e}_z \times \underline{u} = \underline{0} \tag{3.14}$$

with the centrifugal correction being bundled into pressure.

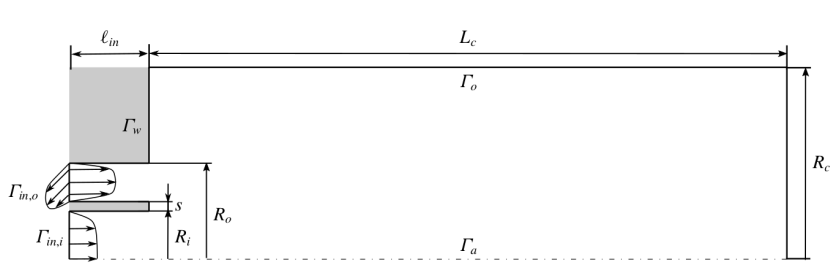

(a) Figure 1 illustrating the numerical setup,

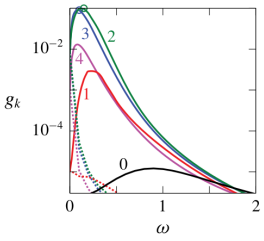

(b) Figure 10 showing resolvent gains $g_k = \sigma^{(1)}$, see 1.2.4.

Figure 3.5: Figures taken from [86], concerning with the resolvent study of a coaxial swirling jet at $(Re; S) = (200; 1)$.

Assuming $q(x, y, z, t) = q_0 e^{i(\underline{k}\cdot\underline{x}-\omega t)} + q_0^* e^{-i(\underline{k}\cdot\underline{x}-\omega t)}$, one obtains from equation (3.14) and the continuity equation

$$u_{x0} = p_0 \frac{\omega k_y + 2iSk_x}{\omega^2 - 4S^2}, \tag{3.15}$$

$$u_{y0} = p_0 \frac{\omega k_x - 2iSk_y}{\omega^2 - 4S^2}, \tag{3.16}$$

$$u_{z0} = p_0 \frac{k_z}{\omega}, \tag{3.17}$$

$$\omega^2 = \frac{4S^2 k_z^2}{k_x^2 + k_y^2 + k_z^2} \tag{3.18}$$

A few points immediately stem from these derivations. First, as long as $\omega < 2S$, a solution exists with real k_x, k_y, and k_z. Therefore, a wide range of inertial waves can exist in any rotating flow. This continuous set of waves becomes discrete when the waves are confined, as established in [116, chapter 11] where they are referenced as Kelvin waves, or [48, chapter 4].

Secondly, this derivation does not establish an amplification mechanism *per se*. Indeed, the waves derived above do not grow in time in the chosen formalism. However, resonant phenomenon has been observed experimentally by [78] when multiple inertial waves of the same frequency piled atop one another, leading to flow transition.

[70] mentions interactions between inertial waves and KH modes as a phenomenon that could occur at low frequencies. According to this author, this has a stabilising effect on $m > 0$ modes. Sadly, even though literature on inertial waves is expansive when considering rotating cylinders or large rotating flows, detailed understanding of the role these waves play in jets remains lacking.

3.1.3 Numerical evidence

On the numerical front, [74] used a line vortices model to study the evolution of rotating jets. These calculations bring to light complex interplay between KH phenomena in the axial and azimuthal directions as well as the influence of C effects, as visible in figure 3.6. Indeed, the large rolls visible on the first moments of that calculation bring to mind the usual KH rolls. However, the introduction of swirl leads to the apparition of structures in the crest of the rolls that break the overall structure symmetry.

These different phenomena are very sensitive to initial conditions, displaying chaotic behaviour. One of the major effects of introducing swirl in the flow is the formation of counter-rotating structures. These structures can in turn be dispersed by strong KH waves or overtake them, hinting at a competition between KH and C effects.

More recently, [84] performed a LES of a swirling flow and then a SPOD to obtain the most energetic fluctuations of this flow. This study was performed at relatively low Reynolds number, but attained high swirl, as the focus of the authors was on the description of vortex breakdown. In the regime that is of interest to this study, the authors exhibited four spirals at very low frequency, which were considered to be a consequence of the coordinate system and spurious.

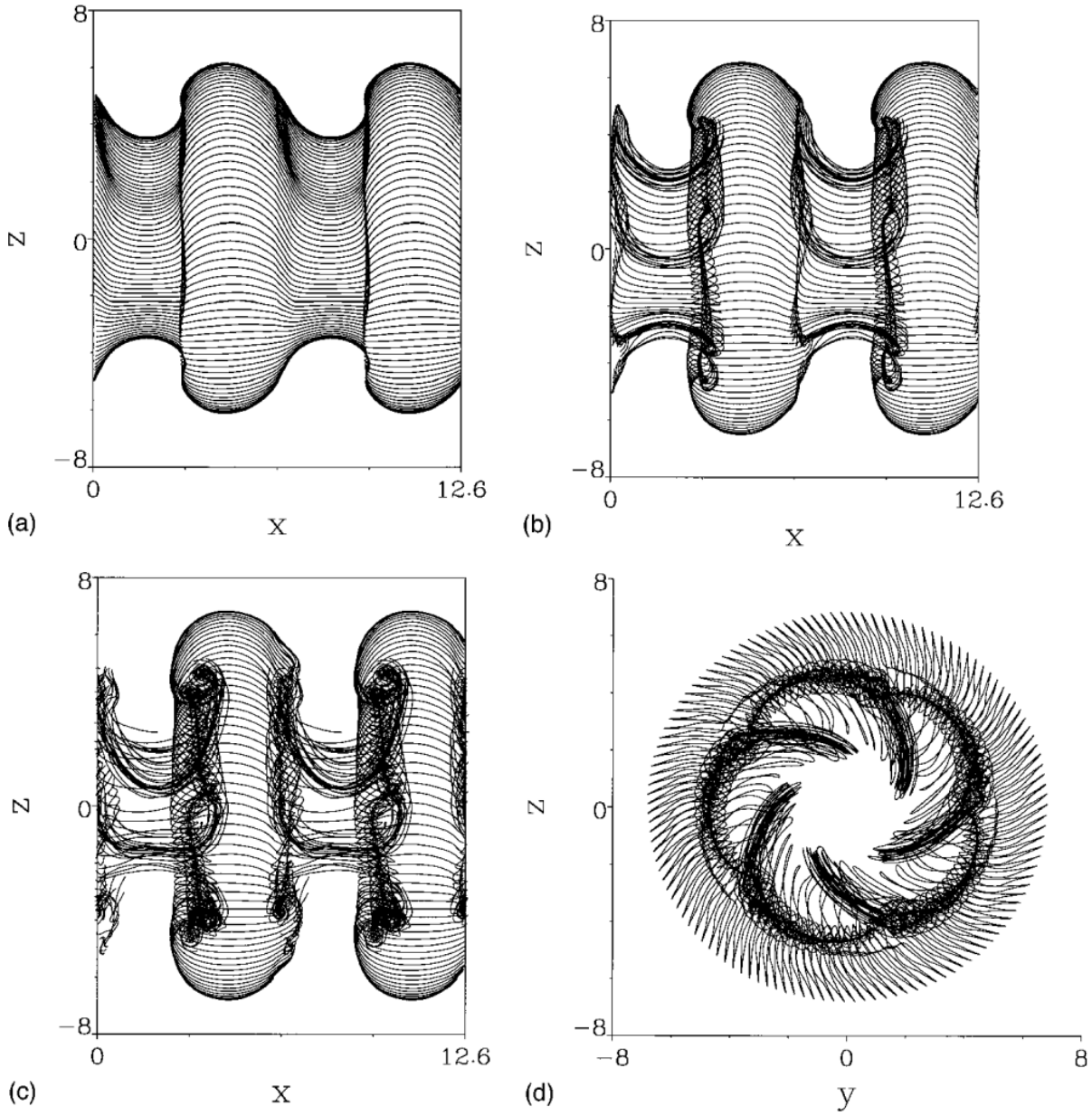

Figure 3.6: Reproduction of figure 10 of [74], representing a swirling jet computation by the method of vortex lines experiment with $\Delta U_\theta/\Delta U_x = 8.2$ subject to an axisymmetric perturbation of amplitude 5%, and an azimuthal disturbance of amplitude 0.04%. Shown are side views at times 0.977 `(a)`, 1.187 `(b)`, and 1.343 `(c)`, along with an end view for $t = 51.343$ `(d)`.

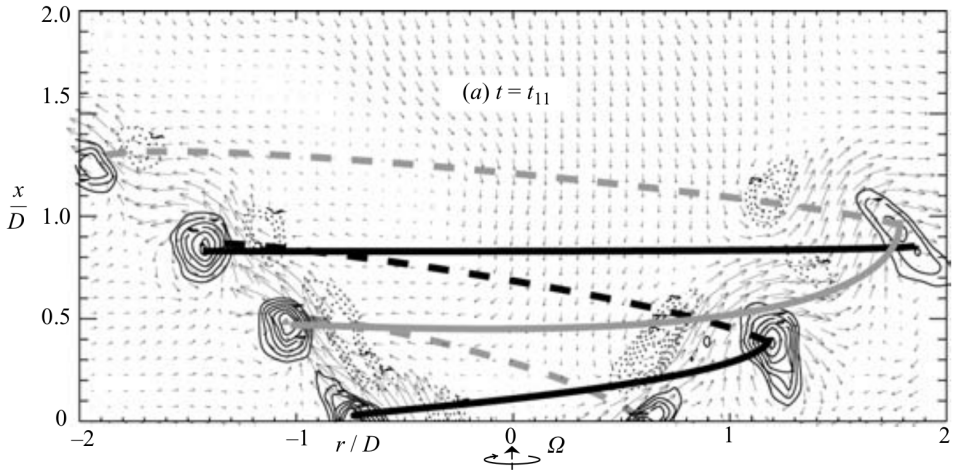

Figure 3.7: Excerpt from figure 6 of [69], representing a swirling jet experiment at $(Re; S) = (967; 1.03)$. In grey and black is the outer shear layer double spiral $m = -2$, vorticity contours are superimposed, solid in the outer shear layer and dotted in the inner shear layer. Velocity field is also represented as a quiver plot. Note the indirect swirl direction.

The Direct Numerical Simulation performed in [115] outright points out at a counter-winding counter-rotating double spiral being selected in a regime close to vortex breakdown. Concerned with a Grabowki-Berger vortex, a case further detailed in 4.4.2, this study observes a regime of axisymmetric, another regime of bending breakdown, and a third regime of helical breakdown depending on the swirl intensity. The authors found that the local critical nature of the flow was a good measure of the onset of vortex breakdown. [43] builds upon this study to outline the non-parallel nature of the mechanism, which behaves like a bluff body in the wake of the jet. Again, breakdown is explained using the transition from convective to absolute instability.

3.1.4 Experimental evidence

[15, 40, 69, 95] all presented experimental evidence of spiral-type coherent structures in a rotating jet. The last three especially were able to single out double spirals using dye visualisation as well as Particle Image Velocimetry.

Through loudspeakers, [40] forced the jet at specific azimuthal wavenumbers and observed the resulting flow. In this manner, the robustness of vortex breakdown was established as well as the receptivity of the flow to double or triple spirals, such as the one presented in figure 3.7.

[92] also performed high fidelity measurements that compared well to weakly non-parallel spatial stability analysis predictions close to the nozzle at relatively low Reynolds number. When forcing appropriately at the lip, the authors found a double spiral co-winding counter-rotating mode present close to the nozzle but decaying faster in the downstream direction than the dominant bending mode. This mode was explained invoking C instabilities, mostly under the argument that this mechanism favours $m < 0$. At the time of writing, it is unclear to the present author why this would be the case.

The works of [40, 92] are especially relevant to this study as they feature actuated jets. Reducing the space of available forcing to a specified azimuthal wavenumber in this manner can only be expected to facilitate comparison with resolvent modes.

Observing the lack of a resolvent study of a turbulent swirling jet, albeit not a lack of interest, this work aims for a contribution on the subject. This paper is organised as follows: section 3.2 presents the procedure followed to obtain the baseflow used for this work as well as its main characteristics. On a more theoretical note, section 3.3 details the resolvent analysis procedure followed here, as well as a validation case. Then, section 3.4 showcases the most important results, namely the gains and the various structures obtained. Finally, section 3.5 summarises the chapter.

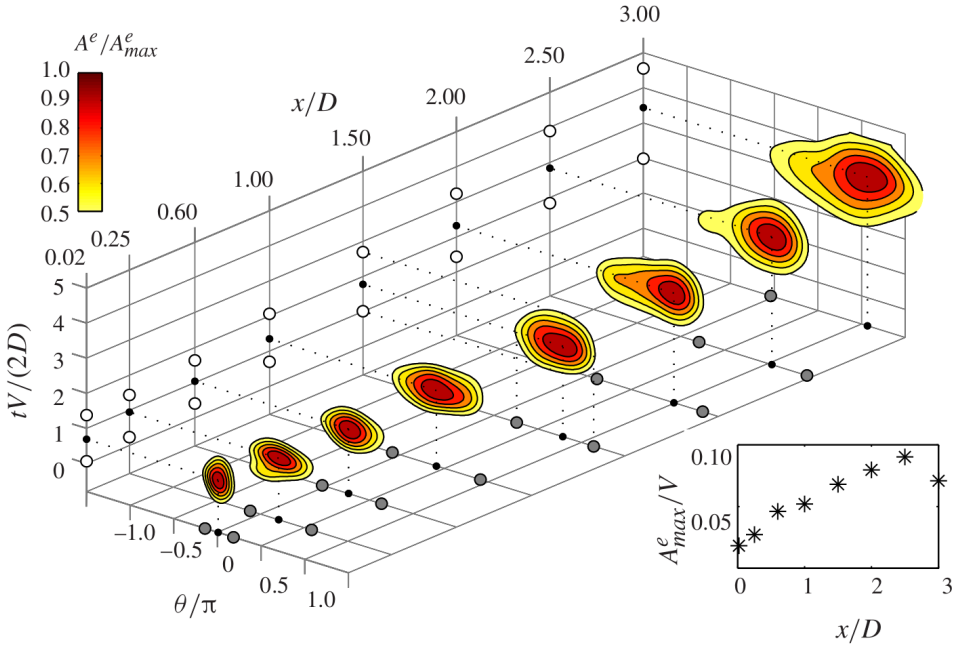

Figure 3.8: Part of figure 25 in [92], representing a wave packet envelope in a swirling jet experiment at $(Re; S) = (20,000; 0.6)$. Contours are normalised by their maximum A^e_{max} that varies with x as plotted on the bottom right.

3.2 Baseflow

The objective of this section is to obtain a baseflow $\underline{Q} = \left[\underline{U}^T, P\right]^T$ satisfying the stationary incompressible RANS equations (1.2) with an eddy viscosity

$$\begin{cases} \underline{\underline{\nabla U}}\ \underline{U} + \underline{\nabla} P - \underline{\nabla} \cdot \left[\nu \left(\underline{\underline{\nabla U}} + \underline{\underline{\nabla U}}^T\right)\right] = \underline{0}, \\ \underline{\nabla} \cdot \underline{U} = 0. \end{cases} \tag{3.19}$$

This baseflow can alternatively be called fixed point of equation (3.19) and provides a model for the baseflow of equation (1.1). Throughout this chapter, viscosity is taken as $\nu = 1/Re + \nu_t$ with Reynolds number $Re = UR/\nu_0 = 200,000$. ν_0 is the molecular kinematic viscosity, U is the reference velocity defined as the axial velocity at the origin, R the reference length corresponding to the radius of the jet.

$\nu_t(\underline{U}, \underline{x})$ is obtained using the SA model, originally introduced in [126]. Alternatives are presented in section 1.1.2, where the present approach to RANS is explained. It is possible that the SA model performs rather poorly in this high Reynolds regime, however it was numerically cheap and easy to implement, with natural boundary conditions of zero derivative at outlets, and zero value at the walls and inlet, resulting in a largely laminar inflow.

3.2.1 Case description

The case of interest is an axisymmetric jet with a nozzle represented in figure 3.9. Our coordinate system is cylindrical and direct, meaning the azimuthal axis is coming towards the reader in figure 3.9. Said nozzle is of radius and length R. The nozzle has a finite width at the inlet $\epsilon = 10^{-4}$, but sharpens into a point at the lip.

At the inlet inside the nozzle (see figure 3.9), the baseflow is prescribed as

$$\underline{U}_{inlet}(r) = \tanh\left[6(1 - r^2)\right] (\underline{e}_x + Sr\underline{e}_\theta)\,. \tag{3.20}$$

S being swirl intensity, a crucial parameter for flow behaviour. Without loss of generality, this study only considers positive swirl, meaning that the vortex winds in space in the direct sense defined by the

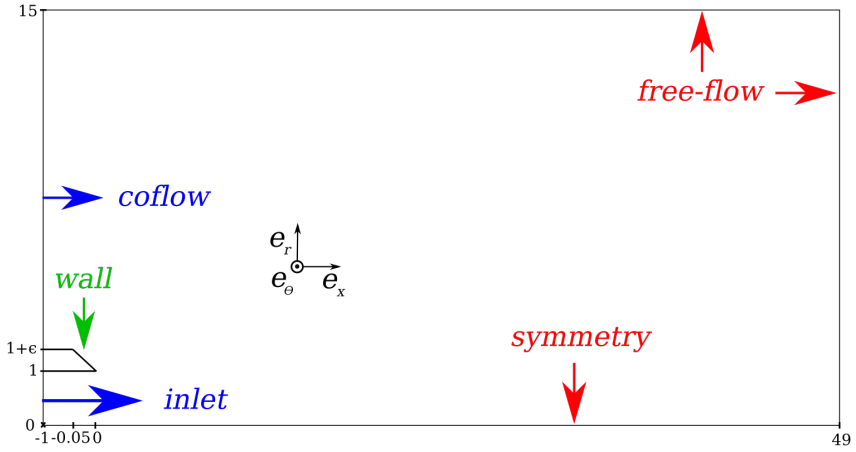

Figure 3.9: Case layout.

right-hand rule with respect to the axial direction. Inlet profiles are very similar to those presented in figure 4.2a, and resemble a smooth plug flow with a solid body rotation of dimensionless vorticity S. This flow is clearly centrifugally unstable according to Rayleigh's criterion derived in [108], as the azimuthal velocity decays exponentially at the nozzle wall.

In practice, this was not enough to obtain a flow using the `OpenFOAM` code. It is well known that recirculation regions near outlets with weak convection can lead to numerical challenges as flow is brought in from outside the numerical domain. To prevent this issue, a weak coflow coaxial to the jet was introduced, which we specify as

$$\underline{U}_{coflow}(r) = 2U_m\tilde{r}(1-\tilde{r}/2)\underline{e}_x \tag{3.21}$$

with $U_m = 0.05$ and $\tilde{r} = (r-1-\epsilon)/(19-\epsilon)$. Therefore, the axial coflow profile evolves as a parabola that goes to zero at the wall and increases to about five percent of the jet axial speed at the domain top. Velocity is also set to zero at the walls. At the axis of symmetry $r = 0$ we impose zero radial and azimuthal velocities, as well as $\partial_r U_x = 0$.

For the outlets at the top and the far right of the domain, boundary conditions are stress-free, which is a mixed boundary condition between the pressure and velocity so that

$$P\underline{n} = \nu\left(\underline{\underline{\nabla U}} + \underline{\underline{\nabla U}}^T\right)\underline{n} \tag{3.22}$$

with $\underline{n}$ the vector normal to the boundary - in this case either $\underline{e}_x$ or $\underline{e}_r$. This condition is also sometimes called 'free flow' or 'outflow'.

This setup allows for a very stiff baseflow, with quite a thin shear layer. To define the shear layer thickness in the presence of coflow, consider

$$\begin{cases} U_m(x) = \min\limits_r U_x(x,r), \\ r_m(x) = \arg\min\limits_r U_x(x,r), \end{cases} \tag{3.23}$$

$$\Pi(x,r) = \frac{U_x(x,r) - U_m(x)}{1 - U_m(x)}, \tag{3.24}$$

$$\Theta(x) = \int_0^{r_m} \Pi(x,r)\left[1-\Pi(x,r)\right] r\mathrm{d}r. \tag{3.25}$$

This leads to figure 3.10 and about $\Theta(R) \approx 0.02$. For reference, the shear layer thickness of the flow used by [121] obtained by LES is also shown, appropriately adimensionalised. Thus this study's baseflow has a very sharp but finite shear layer.

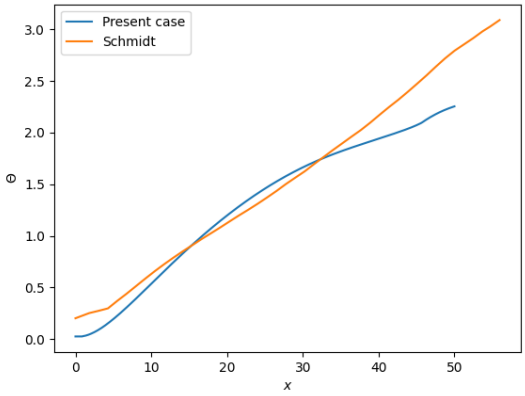

Figure 3.10: Shear layer thickness Θ for the baseflow of this case with reference.

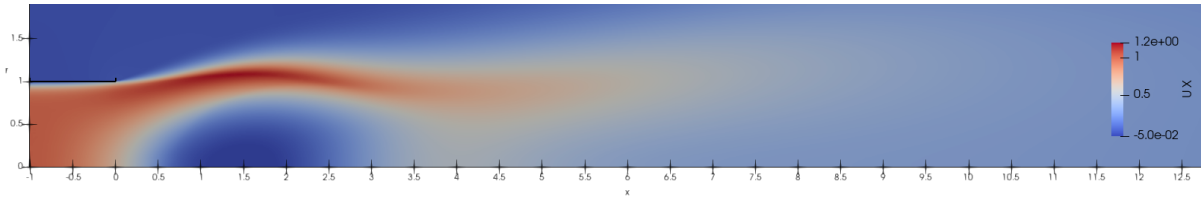

Figure 3.11: $x - r$ view of the x component of a baseflow at $S = 1.6$ close to the nozzle.

3.2.2 `OpenFOAM` calculations

All meshes used in this paper are triangular, unstructured, and non-homogeneous. They were drawn using `gmsh` from [46]. Overall, the final mesh used has about 152,000 nodes and 452,000 elements. The smallest element size is $h = 10^{-3}$. This is small when compared to the entirety of the domain, but large with respect to the nozzle height $\epsilon = 10^{-4}$. In the course of the following calculations, structures were found to be as small as h, which is therefore expected to be an important source of error. However, convergence relative to the mesh refinement was verified, see section 4.1.4, and several validation cases are considered in section 4.4.

In order to compute an incompressible turbulent and viscid flow satisfying the geometric constraints detailed in section 3.2.1, we made use of the `OpenFOAM` CFD software available at [94], more specifically the `simpleFoam` solver. Since this code is based on a finite volume paradigm, calculations were performed on an azimuthal slice containing a single element.

Calculations were performed from $S = 0$ all the way to $S = 1.6$ with a resolution as fine as $\Delta S = 0.01$. This allowed for confirmation that the SA model was able to capture the vortex breakdown effect and subsequent recirculation, see figure 3.11. For more information on this phenomenon, see [80]. In this case, this flow reconfiguration was considered undesirable. Therefore, in the following, $S \leq 1$ is enforced to avoid recirculation effects.

Using a GTSA framework, it has been verified that this regime is modally stable, that is to say all eigenvalues of the linear fluctuation operator taken across the entire domain have negative real part. and that the axial velocity on the axis remains positive throughout the domain.

Actual computations were made on an *Intel(R) Xeon(R) Gold 6230* CPU with a frequency of 2.10 GHz. 40 cores and an absolute tolerance of $\eta = 10^{-12}$ were used for each calculation. The full configuration is available on GitHub under an OpenSource licence.

The result is represented in figure 3.12 for reference. One can see that the jet is fully developed inside the domain with no discernible effect of the outlet boundaries on the top and to the right. The largest gradients are of course the edge of the potential core, most importantly around the nozzle tip.

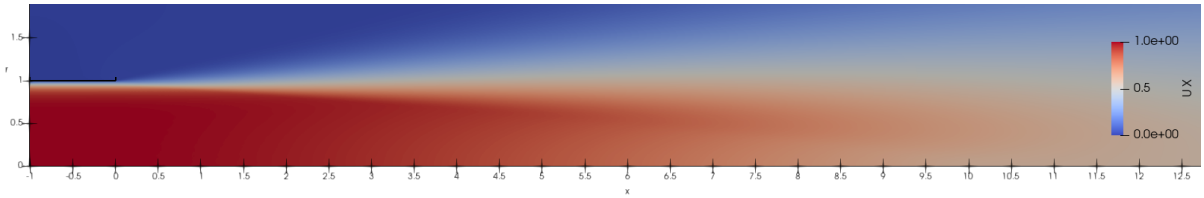

(a) Axial direction,

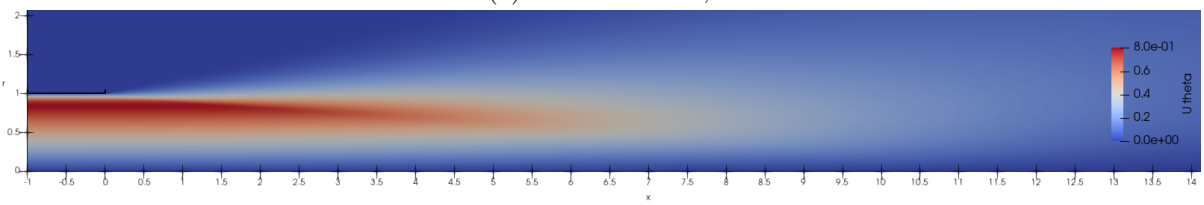

(b) Tangential direction.

Figure 3.12: $x-r$ views of baseflow velocities at $S=1$ close to the nozzle.

3.3 Resolvent analysis

3.3.1 Methodology

The objective here is to accurately predict flow fluctuations on a given baseflow. Said fluctuations $\underline{q} = \left[\underline{u}^T \; p\right]^T$ are three-dimensional and time-dependant but may be decomposed in azimuthal and frequency modes

$$\underline{q}(x,r,\theta,t) = \sum_{m=-\infty}^{\infty} \int_0^{\infty} \underline{\hat{q}}_{m,\omega}(x,r) e^{i(m\theta-\omega t)} + \underline{\hat{q}}^*_{m,\omega}(x,r) e^{i(\omega t - m\theta)} \mathrm{d}\omega. \tag{3.26}$$

In the following, the difference will be made between something wrapped in space around $\underline{e}_x$, which we will call **winding**, and something that is **rotating** in time. Since the structures of interest are real, one also expects a sign change of both m and ω to yield the same mode. Thus, $\omega \geq 0$ is imposed with no loss of generality. With these conventions, a mode with $m<0$ is counter-rotating.

For the purpose of conciseness, $\underline{\hat{q}}_{m,\omega}$ will simply be written $\underline{q}$ in the following. Using this decomposition leads to the operator replacement $\partial_\theta \leftrightarrow im$ and thus $\underline{\nabla} \leftrightarrow \underline{\nabla}_m$. Hence, the fluctuations equations can be derived

$$\begin{cases} -i\omega\underline{u} + \underline{\underline{\nabla_m u}}\;\underline{U} + \underline{\underline{\nabla_0 U}}\;\underline{u} + \underline{\nabla}_m p - \underline{\nabla}_m \cdot \left[\nu\left(\underline{\underline{\nabla_m u}} + \underline{\underline{\nabla_m u}}^T\right)\right] = \underline{\nabla}_m \cdot \left(\underline{\overline{u}\,\overline{u}}^T - \underline{u u}^T\right), \\ \underline{\nabla}_m \cdot \underline{u} = 0. \end{cases} \tag{3.27}$$

At this stage, introducing eddy viscosity in the fluctuation equations has been proven to improve the accuracy of a resolvent process as in [1, 89]. See [87] for a more quantitative comparison of resolvent performance with and without eddy viscosity. This is also consistent with considering equations (3.27) as fluctuations of the baseflow equations (3.19) in the perturbations approach mentioned in section 1.1.2. Hence, viscosity $\nu = 1/Re + \nu_t$ in equation (3.27) is identical to that used in section 3.2.

The method of resolvent analysis has been detailed in section 1.2.4 as well as in works such as [1, 89, 118, 124] and many others beside. For a given set of parameters $(Re; S; m; St)$, and provided a baseflow respecting the parameters $(Re; S)$, such an analysis yields three quantities of interest:

1. The gains $\sigma^{(i)}$, which can be understood as a ratio of fluctuation kinetic energy obtained over non-linear terms work required to produce them. These allow us to order the modes from the most amplified by the linear operator, associated to $\sigma^{(1)}$, to the least amplified.

2. The dominant response mode $\underline{\psi}^{(1)}$ represents the structure which can be expected to arise in the flow fluctuations around the fixed point, provided $\sigma^{(1)} \gg 1$ and $\sigma^{(1)} \gg \sigma^{(2)}$.

3. The optimal forcing mode $\underline{\phi}^{(1)}$ gives the normalised least energetic stimulation that will give rise to $\underline{\psi}^{(1)}$ through the linear operator. It does not correspond to any actual flow behaviour, but may still be useful from an engineering perspective to damp a problematic mode.

Resolvent analysis is a linear method of studying instabilities that differs from GTSA in three important respects:

1. Response modes obtained through resolvent analysis require associated forcing to exist,
2. The use of resolvent permits capturing non-modal phenomena,
3. In the resolvent formalism, frequency is a parameter, whereas modal analysis allows for natural singling out of resonant frequencies.

A more detailed comparison of the methods is provided in section 1.2. This analysis is also global, i.e. fully two dimensional with respect to x and r, which is another difference with LTSA literature making the assumption of parallel flow.

3.3.2 Implementation

In order to perform the process detailed in section 3.3.1 around the baseflow computed in section 3.2, the `FEniCSx` software published in [123] was used. More specifically, the usual Taylor-Hood P2-P1 family was used, solliciting `Basix` elements detailed in [122]. The problem was formulated in weak form for finite element resolution in the `UFL` language published in [4] with no special treatment at the axis of symmetry. Interpolation between the two codes, `OpenFOAM` and `FEniCSx`, was non trivial and required some smoothing. More details are provided in section 4.2.

In line with section 3.2.1, the fluctuations boundary conditions were set as follows: $\underline{u} = \underline{0}$ for all baseflow Dirichlet boundary conditions, stress free at the outlets, and a special boundary condition on the axis of symmetry dependant on the azimuthal wavenumber m

$$\begin{cases} \partial_r u_x = \quad u_r = \quad u_\theta = 0 \text{ if } \ m \ = 0, \\ \quad u_x = \partial_r u_r = \partial_r u_\theta = 0 \text{ if } |m| = 1, \\ \quad u_x = \quad u_r = \quad u_\theta = 0 \text{ else.} \end{cases} \tag{3.28}$$

Once discretisation is performed using finite elements, the SVD is not computed directly. Indeed there is an equivalence between the SVD of $\underline{\underline{R}}$ and the classic diagonalisation of $\underline{\underline{R}}^H \underline{\underline{W}}_\psi \underline{\underline{R}}$, $\underline{\underline{W}}_\psi$ being the matrix of weights associated with the hermitian inner product of response modes $\underline{\psi}^{(i)} \underline{\underline{W}}_\psi \underline{\psi}^{(j)H} = \delta^i_j$.

This gives

$$\underline{\underline{R}} = \sum_i \sigma^{(i)} \underline{\psi}^{(i)} \underline{\phi}^{(i)H} \Leftrightarrow \underline{\underline{R}}^H \underline{\underline{W}}_\psi \underline{\underline{R}} = \sum_i \sigma^{(i)2} \underline{\phi}^{(i)} \underline{\phi}^{(i)H}. \tag{3.29}$$

Which allows for formulation of an eigenvalue problem for the first eigenpair

$$\sigma^{(1)2} = \max_{\underline{\phi}} \frac{\underline{\phi}^H \underline{\underline{R}}^H \underline{\underline{W}}_\psi \underline{\underline{R}} \underline{\phi}}{\underline{\phi}^H \underline{\underline{W}}_\phi \underline{\phi}}, \qquad \underline{\phi}^{(1)} = \arg\max_{\underline{\phi}} \frac{\underline{\phi}^H \underline{\underline{R}}^H \underline{\underline{W}}_\psi \underline{\underline{R}} \underline{\phi}}{\underline{\phi}^H \underline{\underline{W}}_\phi \underline{\phi}}. \tag{3.30}$$

This formulation handles the specificity of cylindrical coordinates in the mass matrices $\underline{\underline{W}}_\psi$ and $\underline{\underline{W}}_\phi$ as well as inside the operator $\underline{\nabla}_m$.

Weights can also be introduced in matrices $\underline{\underline{B}}$ and $\underline{\underline{W}}_\psi$. Having $\underline{\underline{B}}$ go to zero in a region in space is equivalent to preventing this region from being forced in relations (3.27). Since that region is still accounted for in $\underline{\underline{W}}_\phi$, this leads to a range of the forcing vector $\underline{\phi}$ that has no influence on the numerator of equation (3.30), but increases the denominator. Therefore, the eigenvalue solver will always set that region to zero.

Similarly, having $\underline{\underline{W}}_\psi$ go to zero for a region in space prevents response from affecting the numerator of equation (3.30), discouraging forcing that would lead to structures there. $\underline{\psi}^{(i)}$ and $\underline{\phi}^{(i)}$ live in identical spaces here, so the only added value of considering different weighting matrices is the option of additional constraint on the response modes.

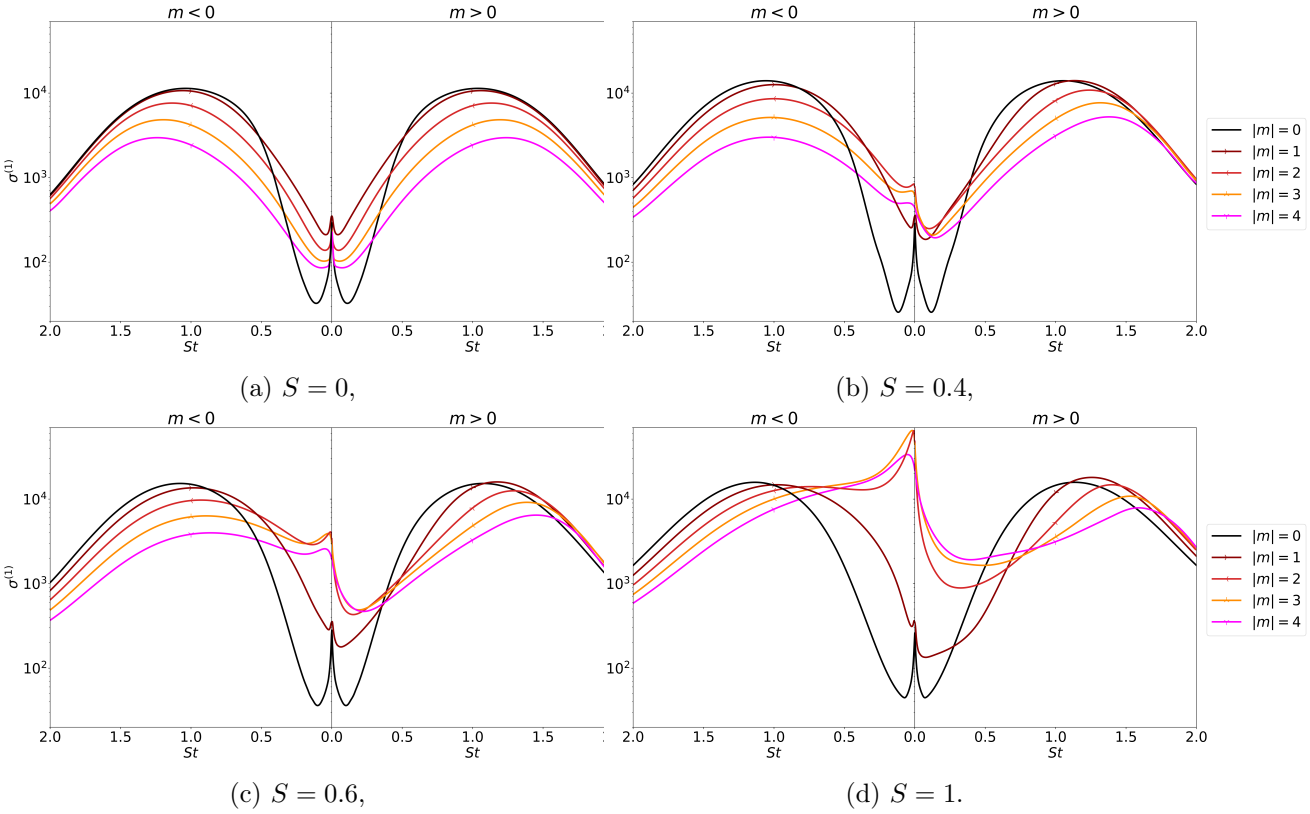

(a) $S = 0$, (b) $S = 0.4$,

(c) $S = 0.6$, (d) $S = 1$.

Figure 3.13: Gains as a function of Strouhal number for different values of S and m.

In the following, $\underline{\underline{B}}$ was forced to zero for the top left of the domain to prevent spurious forcing exploiting baseflow defects. In other words, forcing was constrained to the lower part of the domain for numerical reasons.

The `FEniCSx` library alone proved insufficient to perform the eigenvalue calculations required by the resolvent method detailed in section 3.3.1. Thus the `PETSc` library of [8–10] and `SLEPc` of [49] was used. The parallel version of this library developed in [139] was especially useful. `PETSc` was accessed through the `petsc4py` package published in [27].

In practice the inversion in the $\underline{\underline{R}}$ operator was performed using a lower-upper solver levering MUMPS as in [6, 7] and the eigenvalues calculations using a Krylov-Schur method. Computations were run on 35 cores of an *Intel(R) Xeon(R) Gold 6240Y* CPU running at 2.60 GHz. Again, an absolute tolerance of $\eta = 10^{-12}$ was enforced. The complete code is available on GitHub under an OpenSource licence. Additional information is available in section 4.3.

3.4 Coherent structures

3.4.1 Flow behaviour with increasing swirl

Figure 3.13 represent the evolution of the dominant gains $\sigma^{(1)}$ as a function of Strouhal number $St = \omega R/\pi U$ for different azimuthal wavenumbers m. To respect conventions in the field, the Strouhal number was made dimensionless with respect to diameter, not to radius as is the case for all other quantities. Each plot was made for a different swirl intensity S.

As expected, introducing swirl breaks axisymmetry in equations (3.27). Indeed, convection terms are altered with the introduction of non-zero U_θ and the fluctuation equations are no longer invariant with respect to the transform $\theta \leftrightarrow -\theta$. Therefore, it stands to reason that curves of constant $|m|$ no longer collapse on each other, since they become the solutions to different problems. In section 3.3.1, we

detailed that modes complex conjugates have the same gain. This leads to

$$\forall m \in \mathbb{N}, \forall S \in \mathbb{R}, \lim_{St \to 0^+} \sigma_m^{(i)}\Big|_S = \lim_{St \to 0^+} \sigma_{-m}^{(i)}\Big|_S . \tag{3.31}$$

and this behaviour is readily visible in figure 3.13. Also note that it is expected that gains become damped as $|m|$ increases in a viscous flow, which is also the case here. Figure 3.13 was limited to $|m| < 5$ for readability.

The implementation chosen in section 3.3.2 allows for exploration of very low Strouhal numbers, where strong amplification is observed at high swirl. Because of the boundary conditions detailed in 3.2.1, increasing S amounts to increasing U_θ while keeping U_x constant at the nozzle inlet. Hence, a higher swirl intensity means more kinetic energy as well as extra shear into the fluid, and an associated increase in amplification should not come as a surprise.

However, going from $S = 0$ to $S = 1$ has less then doubled baseflow kinetic energy and introduced an additional component of shear $\partial_r U_\theta$ roughly equivalent to $\partial_r U_x$ already present in the shear layer. Yet one can see in figure 3.13 this leads to an almost two orders of magnitude increase in the gains. Therefore, the dependence of $\sigma^{(1)}$ on swirl intensity, baseflow kinetic energy or shear is highly nonlinear at low frequencies. Hence, it seems likely that a new amplification mechanism absent in straight jets comes into play as swirl is increased...

Unaffected bending and axisymmetric modes

First of all, the axisymmetric behaviour does not substantially change with S. KH modes at $m = 0$ dominate flow behaviour for frequencies $St > 0.5$ in the absence of swirl in figure 3.13a. This is expected, as axisymmetric modes lead to the highest gains for pure $\partial_r U_x$ shear in two dimensions as established in [31]. When swirl is introduced, the $m = 0$ curve and associated structures become overtaken by other azimuthal wavenumbers $m > 0$ at high frequencies $St > 1$. This could be because KH instabilities as described in [39] and section 3.1.1 are growing along flow streamlines. An $m = 0$ mode is locked in the $\underline{e}_x$ direction and incapable of evolving along streamlines tilted by the presence of U_θ. Therefore, it is impossible for an axisymmetric fluctuation to leverage azimuthal KH, no matter the frequency regime. Hence, other modes overtake the $m = 0$ one in the swirling regime at high frequencies because higher wavenumbers are able to leverage KH in the two directions at once.

Bending modes $|m| = 1$ separate for non-zero swirl as all $|m| > 0$ modes do, but do not seem to undergo radical change as S increases. Figure 3.13 seem to imply a phenomenon not unlike Doppler shift, with a $m = 1$ curve shifting into the high frequencies, and the $m = -1$ curve into the low frequencies with little additional amplification relative to swirl intensity overall.

This is not the conclusion of [71], who argues for a most amplified mode at $m = 0$ for a swirling jet. [59, 60, 66, 92] all compute the $m = -1$ mode taking over the axisymmetric KH mode as swirl increases and eventually leading the way to instability.

Another derivation in [72] proposes a much higher most unstable azimuthal wavenumber, going as high as $m = 14$. The latter case is very different in terms of flow profiles, considering very localised swirl in the shear layer. [72] also exhibits significant amplification around $St = 0$. Finally, [32, 39] both argue in favour of an infinite m, though the former also concedes this is probably due to the choice of an infinitely thin shear layer.

All the authors above perform LTSA, which includes a parallel flow assumption as presented in section 3.1. The formalism of [92] is also based on LSSA, but only weakly non parallel. As stated in 3.3.1, there are significant differences between this approach and the one pursued here, which could explain the disparity between results.

On the influence of swirl on spiral modes

Figure 3.13 features a spectacular amplification of modes with $|m| > 1$ at low Strouhal numbers, especially for $m < 0$. Indeed, the gains obtained in this regime become even larger than the maximum of the axisymmetric mode at high frequency traditionally associated with KH waves. The phenomenon persists up to the highest wavenumber studied $|m| = 5$, but wears off around $St \approx 1$.

Even before looking at the mode structure in detail, this points to the LU mechanism as detailed in [91, 101], which is expected to play an important role in flow physics for $|m| > 0$ and low St. This will be discussed in more details later when studying mode structures.

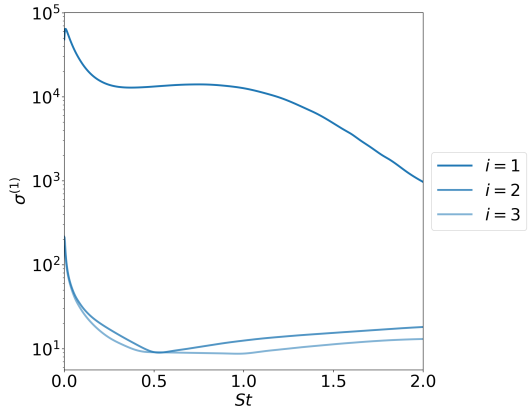

Figure 3.14: Three first gains as a function of Strouhal number for $(S; m) = (1; -2)$.

This amplification is even more dramatic and longer lasting for $m < 0$, or counter-rotating modes. This is not a new result as it has already been observed by [59, 67, 68, 70, 72, 92] that there is a regime of swirl intensity where such modes are amplified. Authors present different results when quantifying growth rates, but the simple persistence of counter-rotating modes for the variety of baseflows considered, from the Batchelor vortex to experimental fitted profiles, does suggest some degree of generality. The difference between LTSA and resolvent analysis outlined in section 3.3.1 still apply of course, and teachings from one method do not always carry over to the other.

This behaviour can also be found in the resolvent analysis conducted by [86] for a coaxial jet, whose gain curves in figure 10 bear striking resemblance to figure 3.13. This study is very similar to the current case, though it was performed at a significantly lower Reynolds number, and for a co-axial jet.

[84] also extracted a multi-spiral mode $|m| = 4$ from LES computations in the regime of swirl intensity that is relevant to this study. This mode has a strong frequency peak at low frequency $St \approx 0.02$, but this mode is dismissed as spurious in the publication.

Finally, experimental evidence of a double spiral in a swirling turbulent jet can be found in [15, 40, 42, 69, 92], where double spiral counter-rotating co-winding structures plays a key role, especially around conical vortex breakdown. Theses structures where extracted from the flows through a variety of techniques from hot wire probes to dye visualisations.

Low rank behaviour

A large gain separation $\sigma^{(1)} \gg \sigma^{(2)}$ for as many m and as wide a range of St is desirable for reduced order modelling, as established in [13]. Indeed, in such a case it is possible to accurately represent the dynamics around the baseflow using only a single mode pair $\underline{\phi}^{(1)}$ and $\underline{\psi}^{(1)}$ for every m and St. Therefore, obtaining high gain separation throughout the parameter space is equivalent to a low-rank resolvent operator $\underline{\underline{R}}$ for the case considered.

Figure 3.14, which is representative of relative gains behaviour for all m at high swirl, shows this is indeed the case, with a large gain separation throughout the range of Strouhal numbers considered.

3.4.2 Kelvin-Helmholtz mode

As a first step when examining modes, it can be verified that the resolvent method reproduces known phenomena, such as the well-known KH mechanism detailed in section 3.1.1. Figure 3.15 shows that this is the case.

In this regime which exhibits the largest gain without swirl, one can clearly see structures around the boundary of the potential core. This potential core is clearly visible in figure 3.12a and goes from the nozzle tip at $(x; r) = (0; 1)$ to the lower right of figure 3.15 at $(x; r) = (14; 0)$. This mode changes sign upon entering or leaving the core. Comprised of many rings tightly grouped together in the x direction, the mode is limited to the edge of the potential core and has no support any distance from it.

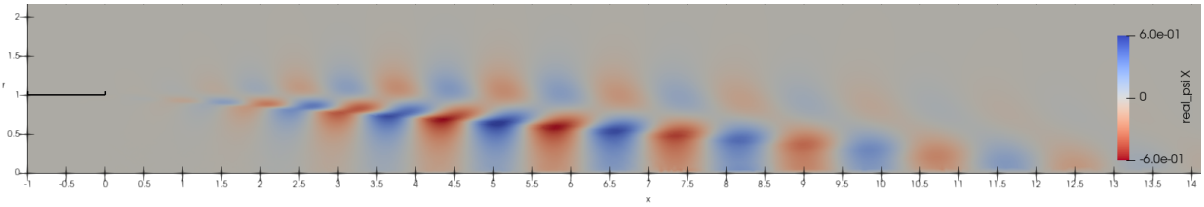

Figure 3.15: Contours of the real part of the first response mode $\psi_x^{(1)}$ in a regime associated to KH $(S; m; St) = (0; 0; 1)$.

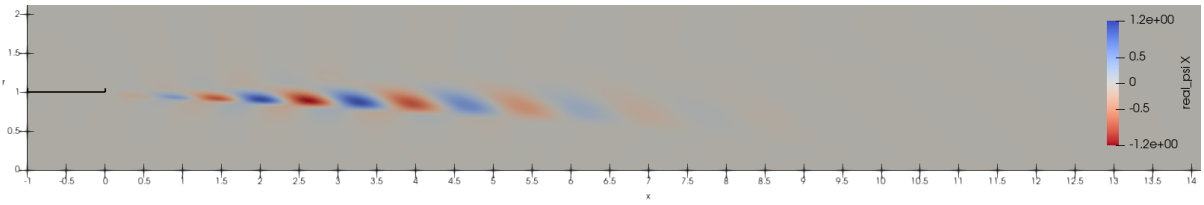

(a) $(S; m; St) = (0; 5; 1)$,

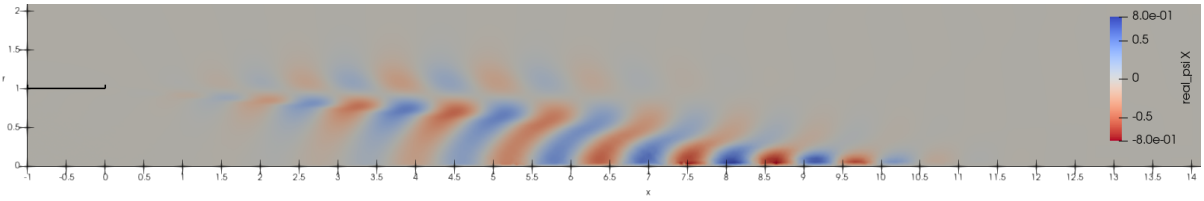

(b) $(S; m; St) = (1; 0; 1)$.

Figure 3.16: Contours of the real part of the first response mode $\psi_x^{(1)}$ in other regimes associated to KH.

It can easily to see in figure 3.16 the same traits that give away KH as the main amplification mechanism in other regimes, always at high frequencies $St > 0.5$. This seems to be the driving force behind most high frequency modes.

3.4.3 Most amplified mode

The focus of our study naturally lands on the most amplified mode, namely the mode $(S; m; St) = (1; -2; 0.004)$, located at the highest peak of figure 3.13d. This mode is depicted in 3D in figure 3.17a alongside its counterpart for $m = 2$. Isosurfaces of axial forcing and of velocity response are shown at 10% of their respective maximum values.

Both modes wind in the same direction in space, but rotate in opposite directions. Given the parameters $|m| = 2$ and $St > 0$, a double spiral structure was expected for both modes. Visually, the modes have a very different helix step. They bear close resemblance to modes exhibited in [30] obtained by numerical continuation.

The case for lift-up

The forcing for both values of m is extremely localised and very similar in appearance. Wrapped around the nozzle, it acts in the region with the highest shear in both axial and azimuthal directions. The forcing mode envelope ends at $x \approx 0$ whereas the response picks up from $x > 4$ onward, all the way to $r = 6$. Therefore, extremely localised forcing at the nozzle produces a very large response spiral taking up almost all of the shear layer.

There is no significant overlap between response and forcing modes. That is a characteristic of the LU phenomenon, where forcing leads to streak formation further downstream in the flow.

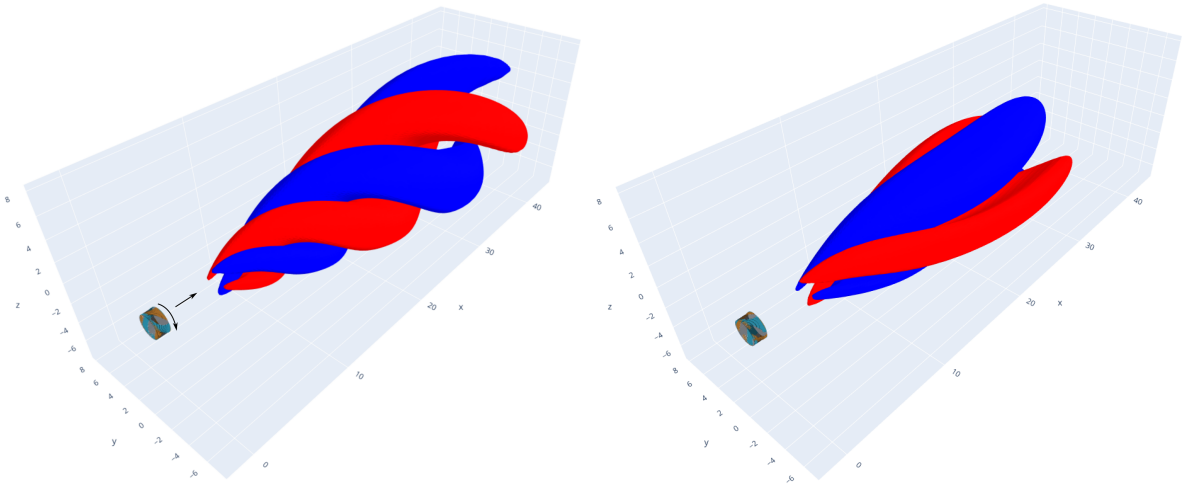

(a) $m = -2$, (b) $m = 2$.

Figure 3.17: 3D isocontours at 10% for $(S; St) = (1; 0.004)$, $m \in \{-2; 2\}$. Axial forcing $\phi_x^{(1)}$ is in cyan-yellow, response $\psi_x^{(1)}$ in blue-red. The black arrows represent main baseflow velocity components, the nozzle is in transparent black.

Figure 3.18 shows a slice of the forcing vectors superposed over contours of the axial response. As expected, the forcing is found to pick up fast fluid from inside the nozzle $r < 1$ and lift it into areas of strong axial response. In the swirling jet case, rolls are more discrete than the flat plate case presented in section 3.1.1, yet this is believed to be the same underlying mechanism. This may be an effect of the case setup that enforces incompressibility but allows for fluid to exit the domain at the top and right boundaries.

The presence of LU can be further investigated by studying the forcing at the nozzle in detail. In figure 3.19a one can see forcing structures tightly wrapped around the nozzle, especially focused at its tip. Also note the tilted structure of the forcing below and above the nozzle, which points to the Orr amplification mechanism.

Figure 3.19b presents baseflow streamlines and the map of the modulus of the forcing component orthogonal to the baseflow in the $x - r$ plane, further scaled by the maximum forcing norm across the image. Formally, this amounts to computing

$$\underline{e}_\perp = \frac{1}{\sqrt{U_x^2 + U_r^2}} \begin{bmatrix} U_r \\ -U_x \end{bmatrix}, \qquad \underline{\phi}_{2D} = \frac{1}{\max \sqrt{\phi_x^{(1)} \phi_x^{(1)*} + \phi_r^{(1)} \phi_r^{(1)*}}} \begin{bmatrix} \phi_x^{(1)} \\ \phi_r^{(1)} \end{bmatrix}, \tag{3.32}$$

and from there derive the orthogonal forcing component

$$\phi_\perp = \left| \underline{\phi}_{2D} \cdot \underline{e}_\perp \right|. \tag{3.33}$$

This is the component that contributes to LU by moving fluid along shear directions. Close inspection of the nozzle tip in figure 3.19b suggests this component is very important where the gradients of the baseflow are strongest. LU is therefore expected to manifest at its maximum around the nozzle tip.

The presence of LU and streaks in non-swirling jets was established in [91] using both experimental data and the resolvent method side to side. It was also listed as a dominant mechanism at low frequency for all $|m| > 0$ in [101] also using resolvent analysis. Therefore, the presence of the same mechanism in a swirling jet at low frequencies is expected.

This explains why bending or axisymmetric modes appear less amplified then the others at low frequency in figure 3.13. Indeed, an $m = 0$ mode cannot generate streaks under constraints of incompressibility and therefore, it is impossible for these modes to exhibit LU. As seen in section 3.1.1, LU is not a phenomenon limited to swirling jets and can arise in straight jets as well. However, the underlying mechanisms for growth are expected to benefit from additional shear in a swirling jet and it stands to

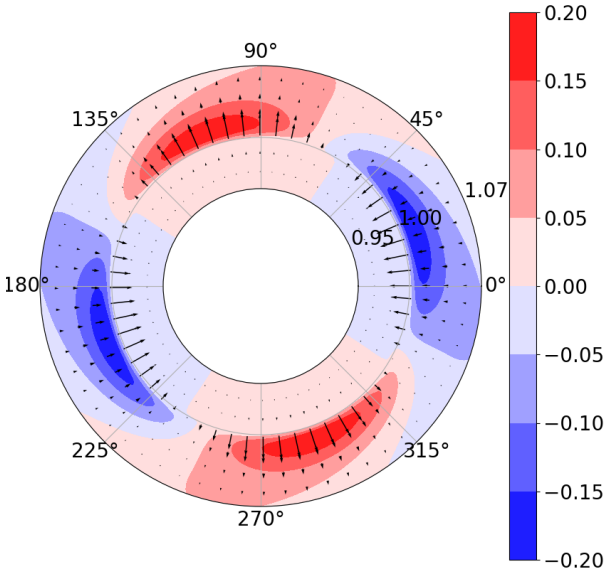

Figure 3.18: Cross plane of the forcing $\underline{\phi}^{(1)}$ at $x = 0$ around the nozzle for $(S; m; St) = (1; -2; 0.004)$. Contours are axial response $\psi_x^{(1)}$.

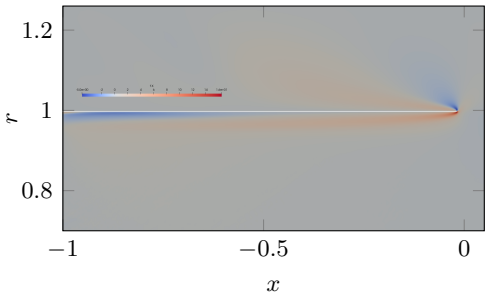

(a) Axial direction, nozzle in white,

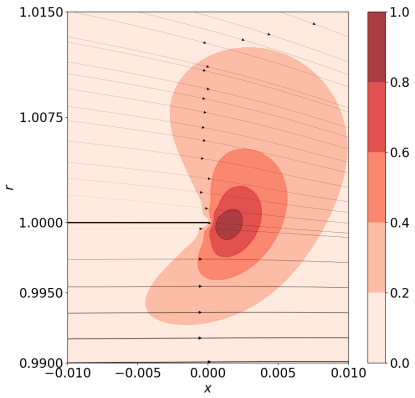

(b) Streamlines and orthogonal forcing component $\phi_\perp$ (close up, nozzle in black).

Figure 3.19: Forcing $\underline{\phi}^{(1)}$ at the nozzle for $(S; m; St) = (1; -2; 0.004)$.

reason that all things else being equal, a mode purely associated to LU would become more amplified as swirl increases.

Indeed, looking back in figure 3.17b, the $m = 2$ mode is similar to a pure streak, as in the figure 5 of [101] or figure 9 of [91]. However, the presence of LU does not shed light as to why modes with $m < 0$ are so much more favoured over $m > 0$ ones, or the presence of a frequency peak.

About Kelvin-Helmholtz

KH instabilities presented in section 3.1.1 are a major candidate to explain the phenomenal gain observed in figure 3.13. It is easier to think about KH by assuming a parallel flow. Writing $\underline{U} = U_x(r)\underline{e}_x + U_\theta(r)\underline{e}_\theta$ and periodicity, it becomes possible to write

$$\underline{q}(x,r,\theta,t) = \sum_{m=-\infty}^{\infty} \int_{-\infty}^{\infty}\int_{-\infty}^{\infty} \underline{\hat{q}}_{k,m,\omega}(r) e^{i(kx+m\theta-\omega t)} + \underline{\hat{q}}^*_{k,m,\omega}(r) e^{i(\omega t - m\theta - kx)} \mathrm{d}k\mathrm{d}\omega. \tag{3.34}$$

instead of equation (3.26). One can then define a wavevector $\underline{\Lambda} = k\underline{e}_x + m\underline{e}_\theta$ for the fluctuations and a principal shear vector $\underline{\Sigma} = \partial_r U_x \underline{e}_x + \partial_r(U_\theta/r)\underline{e}_\theta$ for the baseflow.

In this simplified configuration, consider a cylinder of constant radius r. It is possible to see this cylinder as the interface between two fluids of velocity $\underline{U}(r^-)$ and $\underline{U}(r^+)$. Instabilities on this surface may be studied in the $\underline{U} - \underline{e}_r$ plane. In the presence of shear and neglecting curvature, taking inspiration from [39, section B.2] which generalised results of [31, section 1.4], the growth rate of the KH mechanism on the surface of the cylinder goes like $\underline{\Lambda} \cdot \underline{\Sigma}$.

This scalar product may also be derived from the fluctuations phase along streamlines

$$\vartheta = kx + m\theta - \omega t. \tag{3.35}$$

By itself, the phase is not informative of fluctuations behaviour. Taking the derivative of relation (3.35) with respect to time yields the Doppler-shifted frequency

$$\gamma = kU_x + m\frac{U_\theta}{r} - \omega. \tag{3.36}$$

This quantity appears in [16, 17, 51, 66] and $i\gamma$ is called Doppler-shifted growth rate in [16] for a complex ω. Physically, this quantity relates to fluctuation variation along streamlines.

In a parallel flow, the shear is purely radial. Therefore the important feature of shear modes is not Doppler-shifted growth rate along streamlines *per se* but rather its radial distribution. If the local time-wise evolution of the mode is the same across r, then the mode cannot be labelled a shear mode in a parallel flow. On the contrary, if it is large in areas of high baseflow shear, this is a strong indication that the mode is feeding on shear.

Taking its derivative in the radial direction gives

$$\partial_r\gamma = k\partial_r U_x + m\partial_r\left(\frac{U_\theta}{r}\right) \Rightarrow \partial_r\gamma = \underline{\Lambda}\cdot\underline{\Sigma}. \tag{3.37}$$

It is proposed to use the dot criterion $\underline{\Lambda}\cdot\underline{\Sigma}$ as an indicator of the presence of a shear amplification mechanism. Coincidentally, this product is also of import to C instabilities, whose driving force is presented in section 3.1.2. $\exists r_0 \in \mathbb{R}^+ | (\underline{\Lambda}\cdot\underline{\Sigma})(r_0) = 0$ is a sufficient condition for C amplification in [66, equation (5.6)]. Its derivation in that work involves a Doppler-shifted frequency and looking for a stationary wave in the regime $\|\underline{\Lambda}\| \gg 1$. The same product appears again at leading order in the Wentzel-Kramers-Brillouin analysis of [16, equation (3.8)] also in the large wavenumber approximation. At first order, it would appear that the two mechanisms of KH and C work against each other.

However, for a pure LU mode, one would also expect to have $\underline{\Lambda}\cdot\underline{\Sigma} = 0$. Indeed, considering a non-swirling flow where $\underline{\Sigma} = \partial_r U_x \underline{e}_x$, and an idealised response made purely of very long streaks. The very long streaks mean $k \to 0$ which also leads to $\underline{\Lambda}\cdot\underline{\Sigma} = 0$. Therefore, there is no equivalence between a zero dot criterion and a C mechanism. Indeed, it is only a sufficient condition for its presence.

Of course, the method presented in section 3.3 is not local. So in order to exploit the dot criterion k must be approximated. Arbitrarily, it was chosen to use an average of the approximate of every component

$$k \approx \frac{1}{3}\Im\left(\frac{\partial_x u_x}{u_x} + \frac{\partial_x u_r}{u_r} + \frac{\partial_x u_\theta}{u_\theta}\right). \tag{3.38}$$

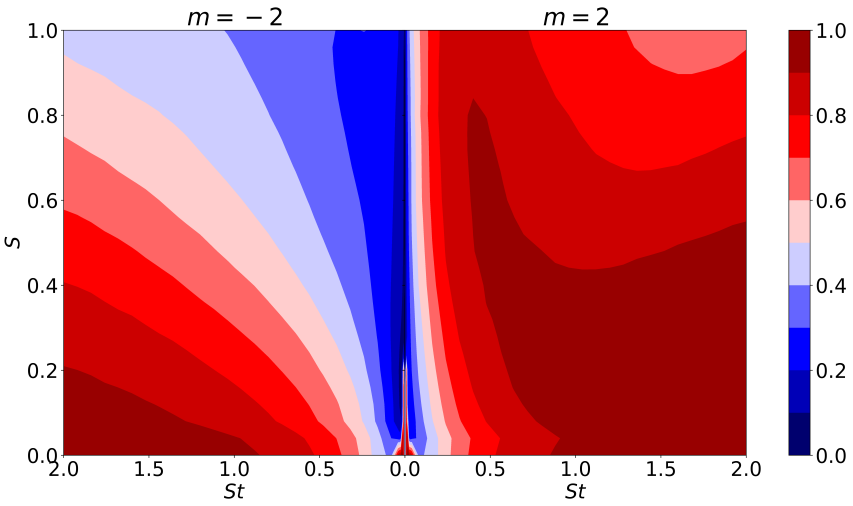

Figure 3.20: Contour of averaged wavenumber-principal shear relative alignment χ as a function of swirl intensity S and Strouhal number St for $m \in \{-2, 2\}$.

This approximation makes it possible to compute different criteria and to compare to LTSA results. For instance, the necessary condition relative to non-axisymmetric centrifugal growth from [51, equation (20)] rephrased from the sufficient stability criterion of equation (3.12) is written

$$\exists \underline{x} \in V | k^2 \frac{\partial_r (r^2 U_\theta^2)}{r^3} - \frac{2km}{r^2} U_r \partial_r U_x - \frac{(\underline{\Lambda} \cdot \underline{\Sigma})^2}{4} < 0. \tag{3.39}$$

This was verified to hold across all frequencies for $(S; |m|) = (1; 2)$, which is a hint to the presence of a C mechanism. Note that the dot criterion has a meaning opposite to [66, equation (5.6)] here. Indeed, for [51] having a high dot criterion is sufficient to lead to a C mechanism, whereas [66] considers this quantity should be zero instead.

The dot criterion exhibited in equation (3.37) was computed and averaged over the envelope of the modes. Said envelope was defined as the area where the square of mode amplitude $\|\underline{u}\|^2 = |u_x|^2 + |u_r|^2 + |u_\theta|^2$ was above ten percent of its maximum value. Taking this region as $\mathcal{A}_{10\%}$ and its surface area as $A(\mathcal{A}_{10\%})$, the quantity of interest becomes average alignment

$$\chi = \frac{1}{A(\mathcal{A}_{10\%})} \int_{\mathcal{A}_{10\%}} \frac{\underline{\Lambda} \cdot \underline{\Sigma}}{\|\underline{\Lambda}\| \, \|\underline{\Sigma}\|} \mathrm{d}A. \tag{3.40}$$

This quantity represents an average estimate of the alignment of the local wavevector $\underline{\Lambda}$ with respect to the principal shear direction $\underline{\Sigma}$. If this quantity is high, this is an indication of the predominance of shear instabilities in the mode. Conversely, if it is low, it indicates another mechanism might be at play.

In the case $(S; m; St) = (1; -2; 0.004)$, $\chi \approx 10^{-3}$. From this one can come to the conclusion that the observed dramatic amplification at low Strouhal numbers is not KH, and that it could be C.

This quantity is visible in figure 3.20 for a broader range of the parameter space. Overall, the alignment increases with St. This is expected as KH becomes the dominant mechanism for driving growth at high frequency. Conversely, χ remains low in a narrow regime around zero frequency, which is the region where LU is expected and C could exist, tightly clustered around zero. The region of lowest alignment $\chi = 0$ remains centred at low frequencies and even narrows down as swirl intensity S increases, even if low alignment persists for $m > 0$ up to $St = 0.4$.

Evolution of alignment relative to S is pretty straightforward in the $m = -2$ case, with region of low alignment growing with swirl. Behaviour for $m = 2$ is less intuitive, with KH instabilities quite quickly taking over the low frequencies up to $S \approx 0.5$. At higher S, there seems to be a valley forming, with KH receding in the high frequency, high swirl regime. The upper right corner of figure 3.20 is the only region where the previous observation that χ increases with St is shown wrong.

The bottom-centre region of the domain where $S < 0.4$ and $St < 0.05$ seems to be something of a limited outlier in a region of overall low orientation. In an effort to acquire additional information, a

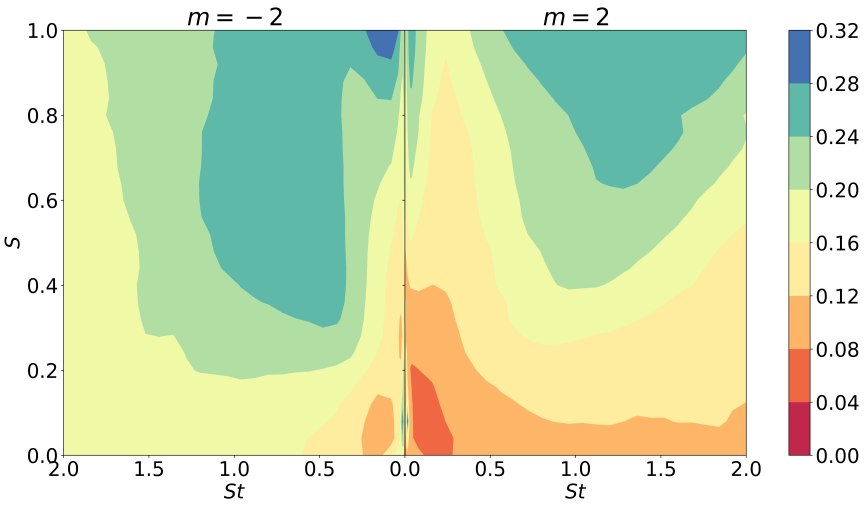

Figure 3.21: Contour of standard deviation of wavenumber-principal shear relative alignment Υ as a function of swirl intensity S and Strouhal number St for $m \in \{-2, 2\}$.

standard deviation was computed

$$\Upsilon = \sqrt{\frac{1}{A(\mathcal{A}_{10\%})} \int_{\mathcal{A}_{10\%}} \left(\frac{\underline{\Lambda} \cdot \underline{\Sigma}}{\|\underline{\Lambda}\| \, \|\underline{\Sigma}\|} - \chi \right)^2 \mathrm{d}A}. \tag{3.41}$$

and displayed in figure 3.21. Regions of high deviation are associated to a very noisy dot criterion over the mode envelope and therefore reduce confidence in a straightforward interpretation of figure 3.20. Indeed, if the dot criterion is high in a part of a mode and not in another, this probably means the same mode is making use of several mechanisms at once.

Overall the distribution of the dot criterion remains contained. For much of the parameter space, $\Upsilon < 0.2$, which could be rephrased as the associated regions have over 60% of their dot values within 0.2 of their average, assuming a Gaussian distribution. Minimum values are achieved in a high alignment regime decidedly associated to KH, when S is low and $m > 0$.

The deviation increases with swirl, and does so faster for frequencies around $St = 1$. This is probably due to the prevalence of KH in this high frequency regime - new mechanisms do not immediately replace KH but instead smoothly take over as swirl is increased. This leads to modes with coexisting regions of high and low alignment, increasing Υ. The standard deviation is maximal in the region of interest at low St, high S for $m < 0$, which reduces the confidence in the previous low value of average alignment χ for $(S; m; St) = (1; -2; 0.004)$.

As a point of reference to compare this dot criterion to, the first resolvent gain was also plotted as a contour plot in figure 3.22. The afore-mentioned drift of the gain peak associated with the KH mechanism at $S = 0$ to low frequencies for $m = -2$ and high frequencies for $m = 2$ is clearly visible, as the main peak appearing at high swirl, low frequency for $m = -2$.

Considering figures 3.20 and 3.22 side by side, their correlation is unclear. Extremes of alignment χ correspond to a fluctuation mode that could be understood as making the most of the C or KH amplification mechanism. But this does not seem to lead to higher gains over the entire parameter space. Indeed, the maximum gain at low swirl is not associated to any alignment maxima, and the drift of $\sigma^{(1)}$ with S is not clearly associated with a tendency in χ.

However, when taking figure 3.21 alongside figure 3.22, one can see that $\sigma^{(1)}$ tends to be maximal when Υ is maximal. The secret to maximal amplification could be to leverage all mechanisms at once instead of picking one and sticking to it. Indeed, it is possible for a global mode to exploit different mechanisms in different regions of the flow.

This seems to be the case for the most amplified mode, as figure 3.23 illustrates strong variation throughout space with respect to the dot criterion. The mode wavenumber is aligned with principal shear direction close to the potential core where shear is important, but the dot criterion decays, even

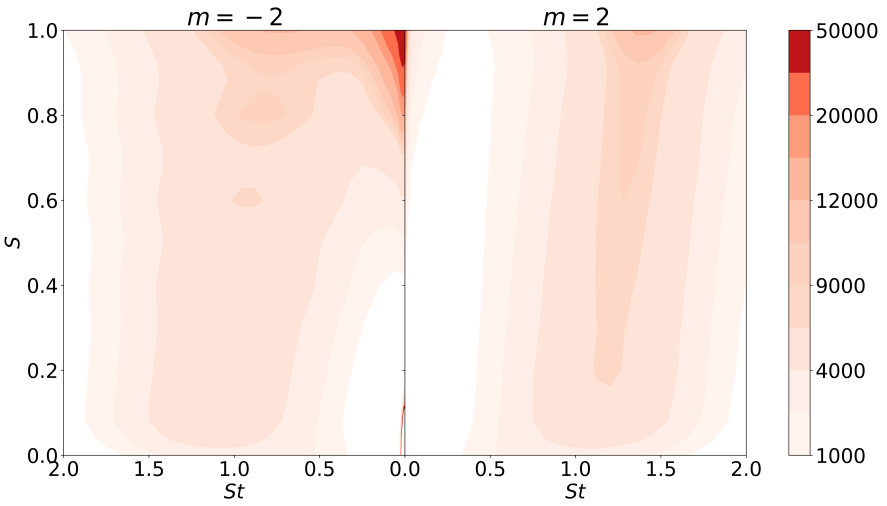

Figure 3.22: First resolvent gain $\sigma^{(1)}$ as a function of swirl intensity S and Strouhal number St for $m \in \{-2, 2\}$.

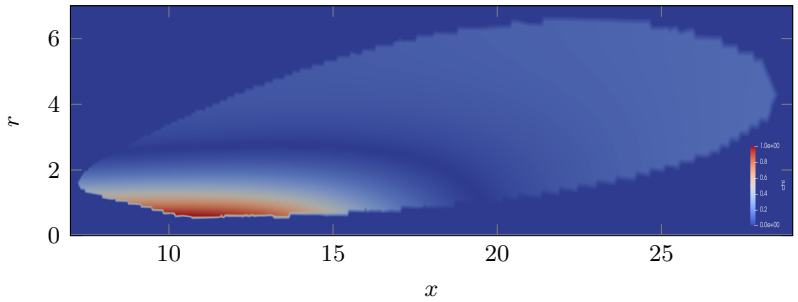

Figure 3.23: Local dot criterion for $(S; m; St) = (1; -2; 0.004)$.

presenting a clear zero arc, as distance to the core increases. Hence, this mode seems to make use of a combination of mechanisms to achieve amplification in different areas of the domain.

3.4.4 Outer mode

Another point in the parameter space worthy of attention is the $St = 0$ regime of figure 3.13a for $|m| > 1$. The choice of $m = 2$ makes for easier comparison with the modes of section 3.4.3. Isocontours of this mode are displayed in figure 3.24a.

Shear outside the nozzle

The response is strongly concentrated on top of the nozzle, latched onto a region of slow moving fluid. It is not allowed to wind or rotate because of the parameter $St = 0$ - it has to remain steady. This behaviour persists for all S. Previous calculations comparable to this one such as [86, 101] that had a

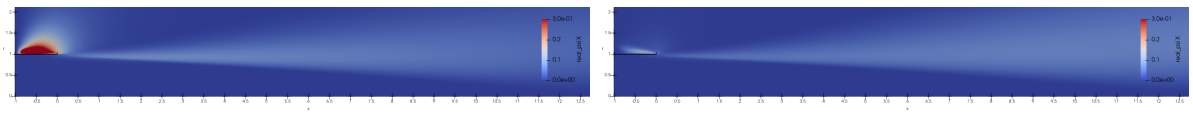

(a) No constrain, (b) Response constrained to $x > 1$.

Figure 3.24: Axial component of the response $\psi_x^{(1)}$ for $(S; m; St) = (0; 2; 0)$.

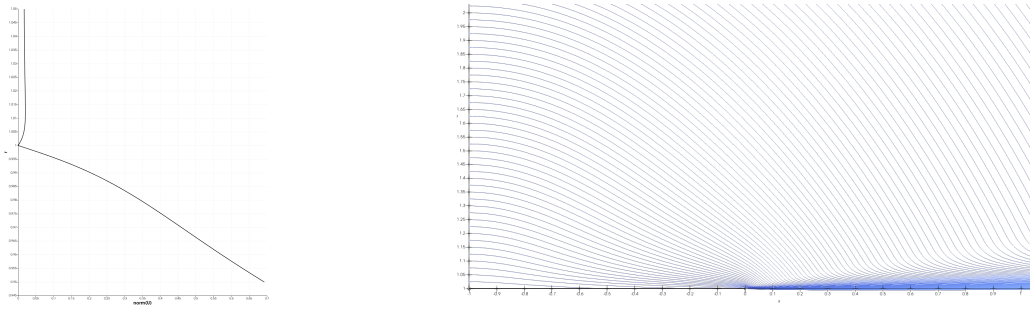

(a) Velocity norm at $x = -0.01$, (b) Streamlines.

Figure 3.25: Baseflow visualisations on top of the nozzle.

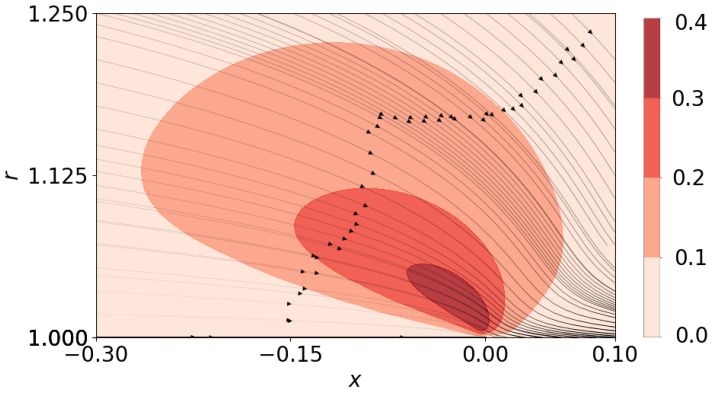

Figure 3.26: Streamlines and orthogonal response component $\psi_{\perp}^{(1)}$ (close up) for $(S; m; St) = (0; 2; 0)$.

wall on top of the nozzle outlet could not witness this. Similar phenomenon was exposed in a conference by [18] also using the resolvent analysis technique on a jet with fluid evolving atop the nozzle.

If one considers the usual definition of ensemble averaging as a time integral, taking $St = 0$ leads to a response mode no longer satisfying $\overline{q} = \underline{0}$, which leads to a breakdown of the RANS decomposition. However, this singularity is lifted here by the regularity of the problem - indeed in practice the resolvent process is found to be continuous around $St = 0$ for all m, so it is possible to define resolvent modes at zero frequency by continuation, as a limit case when $St \to 0$.

To explain the presence of response on top of the nozzle, the baseflow in this area was scrutinised in more detail. It turns out that the baseflow is subject to gradients only about ten times less intense above the nozzle compared to below it, see figure 3.25a. It seems these gradients close to the wall are not entirely generated by the coflow but rather by the significant entrainment induced by the jet visible on the streamlines of figure 3.25b. This contraction leads to a rapid radial increase in axial velocity atop the nozzle, and therefore strong shear.

There is evidence of LU to be found in the response structure on top of the nozzle, see figure 3.26. This figure was drawn in a similar manner as figure 3.19b, plotting the contour of the absolute value of the orthogonal component of the first response mode. This shows the formation of strong fluctuation rolls on top of the nozzle. This rolls are tilted compared to usual LU rolls in the case of plates, but they are still expected to produce streaks.

In the end, the overall slower pace of convection on top of the nozzle could play to the advantage of LU, since forcing mechanisms there have more time to "build-up" streaks before they get advected downstream compared to structures underneath. Contrary to the structures studied in section 3.4.3, here the forcing and response modes are co-located.

This phenomenon also explains the "rebound" of axisymmetric gain curves around $St = 0$ regardless of swirl intensity observed in figure 3.13. Since structures in this regime appear fixed on top of the nozzle

where they are able to leverage KH, they are unaffected by swirl inside it.

Spread-out streaks

Another clearly visible feature of this mode are the streaks created in the shear layer. Figure 3.24a presents a response concentrated on top of the nozzle, but also a diffuse, weak component of the response that exists throughout most of the shear layer. This should not be a surprise, as the LU mechanism detailed in section 3.4.4 is known to produce streaks. These structures are expected to be formed on top of the nozzle, but manifest downstream. In this process, the streaks are spread over the whole shear layer.

In order to measure the importance of these streaks in the final gain, the response mass matrix $\underline{\underline{W}}_\psi$ of equation (3.30) was weighted to only consider response in the region $x > 0$ and an extra resolvent calculation was performed for the same parameters. This process yields figure 3.24b, which is very similar to 3.24a.

Therefore, the streaks generated downstream are energetic - or simply spread out - enough to secure the most amplified position on their own, overtaking other structures even though they seem to require wasting fluctuations kinetic energy atop the nozzle. Moreover, the structure atop the nozzle is damped but not fully removed after the penalisation. This is significant because by relation (3.30), such a structure does not directly contribute to the gain yet still costs energy to produce. It seems that the outer structure response associated to rolls in figure 3.26 is essential to the creation of the streaks, otherwise it would not have survived the weighting process.

The modes only tell part of the story. Between the two modes in figure 3.24, who are associated to different operators, there is a gain variation of about sixteen percent. Thus, the streaks play a significant role in the overall gain even if at any given point in the shear layer their amplitude does not compare to the outer nozzle structures.

3.5 Conclusion

This study presented the resolvent analysis of a turbulent swirling jet. In section 3.2, the process of computation for a very stiff baseflow and its associated eddy viscosity was detailed. The use of an open source solver proved critical to achieve the desired Reynolds number of $Re = 200,000$. Section 3.3 briefly reviewed the theory behind the resolvent method and its implementation for this case. The latter is available online at this link.

The method yielded two significant results. Firstly, strong gain separation and large amplification of low frequency structures were noted in section 3.4.1 as swirl increased, which was explained by a detailed study of the most amplified mode in section 3.4.3. The associated coherent structure was very wide, taking almost all the shear layer, and manifested some distance away from the nozzle. This double spiral co-winding counter-rotating mode is amplified by a combination of LU, Orr mechanism and another amplification mechanism. As a response mode, this structure is associated to forcing and cannot arise or survive without sustained baseflow fluctuations at the nozzle.

A criterion based on relative alignment of fluctuation wavenumber and principal shear direction was presented as an indicator of KH predominance for a given response mode. This criterion shed a new light on the gains exhibited in section 3.4.1 by allowing for easier isolation of regimes where KH dominates. Taking the analysis further and looking at the dispersion of this criterion brought to light mixed behaviour for the most amplified mode as far as the shear amplification mechanism is concerned. Indeed, KH seems to be favoured in a certain region of the mode and negligible in another.

The second result of import coming from the resolvent analysis of the turbulent swirling jet considered stems from the choice to include a finite height nozzle inside the computational domain. This leads at zero frequency and in the absence of swirl to a most peculiar behaviour studied in section 3.4.4. This structure latched outside the nozzle, using entrainment as a source of shear to produce streaks. Contribution of these streaks to gain was shown to be significant, and the structures outside the nozzle were proved to be useful to their generation.

Amongst the drawbacks of the proposed approach, the choice of the SA eddy viscosity model in section 3.2 obviously influenced the final result to an unknown degree. However, inclusion of an eddy

viscosity model in the fluctuations has been shown to improve resolvent accuracy in other works such as [87].

The chosen grid size was expected to be more than sufficient yet structures of interest around the nozzle lip turned out to go all the way to the individual cell scale. This is bad news since it means these structures could be resolved better, but on the other hand there is physical motivation for an inflection point at the nozzle lip that will lead to cell-sized structures for any grid size. In other words, it could be that the chosen sharp tip leads to physically infinitesimal structures latched there.

Last but not least, the choice of an azimuthal Fourier decomposition limited dramatically computational costs, yet it came at the cost of a truly three-dimensional study. It is possible that the additional constraint imposed on the mode because of the azimuthal decomposition led to occlusion of certain physics involving interactions between different azimuthal wavenumbers at once.

Future work on the subject could include a more detailed analysis of the dot criterion, such as the impact of the envelope, limiting the computation of the dot product with regards to mode amplitude but also shear, evaluate different approximations of the axial wavenumber k, and find a similar criterion for centrifugal type of instabilities.

Another possible approach would be to reproduce behaviours presented here by experimental or numerical means other than LTSA, LSSA, or LSTSA. Indeed, these methods have already been extensively performed on swirling jets and are not expected to reproduce the observed behaviour, be it LU or the important amplification observed at low frequencies. GTSA, LES, DNS or experimental measurements in the parameter space considered here are probably better suited to reproducing the most amplified mode of section 3.4.3.

It is also paramount to include a fluid region on top of the nozzle in computations to capture the outer mode discussed in section 3.4.4 and its own LU mechanism at very low frequency. Such a mode could be easier to reproduce experimentally because of its even smaller frequency. Indeed, averaging fluctuations of an experiment reproducing section 3.2.1 is expected to be enough to reproduce this outer mode.

Chapter 4

Numerical considerations

> The devil is in the details.
>
> *Gustave Flaubert*

As could be expected, a PhD student doing CFD spends most of his time coding. Therefore, this thesis would not be complete without an overview of arguably the most important contribution of this thesis to global knowledge. The developed code was called "Swirling Parallel Yet another jet code" (`SPY`), as an homage to Chuhan Wang who provided "Yet Another Jet Code" (`YAJ`) the first building blocks for this code.

Chuhan's contribution was concerned with two-dimensional fluctuations for parallel flows. It was extended to global three dimensions for both baseflow as well as fluctuations and pushed to a parallel framework.

`SPY` deals with planar geometries in cylindrical coordinates and is able to handle arbitrary eddy viscosities as well as any Dirichlet, or stress-free boundary conditions on specified boundaries. The state vector built into the code holds three components of velocity which must satisfy incompressibility for baseflow and fluctuations.

The `SPY` code is available to all on GitHub under an Open Source licence. It is based on the `gmsh`, `FEniCSx`, `PETSc` and `SLEPc` libraries.

4.1 Appropriate meshing

4.1.1 Unstructured paradigm

There is an old saying in the CFD community that says "garbage in, garbage out". In other words, even for relatively simple geometries such as the ones this thesis is concerned with, it is paramount to feed into the code a mesh that is properly tailored to the case, or no numerical scheme will ever lead to any relevant result. As mentioned in section 3.2.2, this was done in this thesis using `gmsh` from [46]. This allowed for an unstructured, irregular triangular mesh.

The geometry was relatively simple, as can be seen in figure 4.1. An ill-fated attempt to include an infinitesimal nozzle led nowhere - although such a geometry can be handled by `gmsh` and `FEniCSx` just fine, this prevents the use of classical continuous basis functions, which makes writing the equations weak form and boundary conditions much harder.

The unstructured nature of the mesh made it very easy to increase resolution in a region, leading to a very refined mesh close to the nozzle that became rapidly coarse on the top edge where no phenomenon of interest is expected to occur. `OpenFOAM` turned out to be extremely sensitive to the mesh, whereas `FEniCSx`'s routines are more robust.

4.1.2 Best of both worlds

Baseflow calculations in `OpenFOAM` were performed on one mesh and interpolate on a second, smaller domain using `scipy.interpolate.griddata` routine with a linear method. This served several purposes:

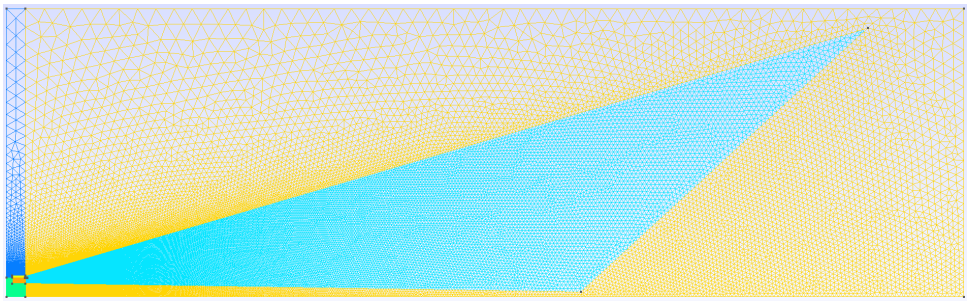

Figure 4.1: Mesh used in SPYP calculations in chapter 3.

1. Smoothing out small defects and oscillations from OpenFOAM outputs that turned out to be very damaging to subsequent linear analysis,
2. Reducing the computational domain for SPYP, since the region of interest for fluctuations is much smaller than the domain expected to be necessary for satisfying baseflow resolution,
3. Addressing different constraints of OpenFOAM and FEniCSx at the same time, the first favouring a very refined mesh, the second more stable on coarser meshes,
4. Because of the formalism chosen, much of the computational resources went into the final SPYP, which meant that there was appeal in resolving SPYP in a relatively coarse manner on the smallest domain possible,
5. OpenFOAM outputs .vtk file format which FEniCSx cannot natively read. Therefore a conversion was needed anyway.

Strictly speaking, OpenFOAM is also a finite volume code, not a finite element one. However the wedge boundary conditions are specifically provided to solve an axisymmetric problem on a small azimuthal slice. This is the solution that was favoured here, with a very small azimuthal angle of a single degree and enforcing a single cell in the θ direction in the mesh. Therefore the solution is expected to be close to an actual finite element two-dimensional calculation.

To reduce interpolation error, a custom Paraview routine was developed to extract the cell centres along the nodes of the OpenFOAM computation. Provided lists of OpenFOAM times, Reynolds numbers and swirl intensities, as well as paths to OpenFOAM face results in .vtm format and the SPY case, this macro will convert the relevant OpenFOAM files into something that the meshio library can read.

```
from paraview.simple import *

path_openFOAM='./'
path_SPY_case='SPY/cases/case/'
times,Res,Ss=[],[],[]

association_dict={}
for i,time in enumerate(times): association_dict[str(time)]={'Re':Res[i], 'S':Ss[i]}

for vtk in association_dict:
  # find source
  vtm = XMLMultiBlockDataReader(registrationName='case_'+vtk+'.vtm',
  FileName=[path_OpenFOAM+'VTK/case_'+vtk+'.vtm'])

  # create a new 'Append Location Attributes'
  vtm_with_loc = AppendLocationAttributes(registrationName='case_loc', Input=vtm)

  save_str=path_SPY_case+'baseflow/OpenFOAM/Re='+str(association_dict[vtk]['Re'])+\
  '_S='+str(round(association_dict[vtk]['S'],3)).replace('.',',')+'.xmf'
  # save data
  SaveData(save_str, proxy=vtm_with_loc, ChooseArraysToWrite=1, PointDataArrays=['U',
  'p', 'nut'], CellDataArrays=['CellCenters', 'U', 'p', 'nut'])
  # clear the pipeline
  for name in ('case_'+vtk+'.vtm','case_loc'):
  source = FindSource(name)
```

```
24      SetActiveSource(source)
25      Delete(source)
26      del source
27
28      with open(save_str, 'r+') as fp:
29        # Read all lines
30        lines = fp.readlines()
31        fp.seek(0) # Move file pointer to the beginning of a file
32        fp.truncate() # Erase the file
33        # Cut out clumsy Times and Grids
34        fp.writelines(lines[:3]+lines[5:12]+lines[15:37]+lines[39:])
35
36      print("Handled case_"+vtk+'.vtm')
```

After the `meshio` interpolation process, smoothing was performed using a pseudo-Laplace equation

$$f = f_{smooth} + \mu \Delta f_{smooth} \tag{4.1}$$

with small $\mu \approx 10^{-4}$ in `SPYB` routines. Equation (4.1) can be interpreted as a small regularisation of second derivatives. This process helped smooth the critical field ν_t, which was also cut-off at $\iota = 10^{-9}$, meaning that any $\nu_t < \iota$ was forced to zero. The intent behind this was to avoid problems in regions of eddy viscosity so small it can be neglected with respect to the molecular viscosity, but rapidly fluctuating nonetheless.

In the end, a third mesh was added which is really just a truncation of the previous one to cut off saturation at the boundary when switching between baseflow computation in `SPYB` and instability analysis in `SPYP`.

4.1.3 A naive saving scheme

Because of the choice to implement `SPY` in parallel and the absence of check-pointing options currently available in `FEniCSx`, a very naive and direct saving scheme was implemented in `src/helpers.py`. Every time a save is required for a given field, every processor takes the owned degrees of freedom and ghost cells and write them out directly into `.npy` files.

This saving scheme is simple but extremely useful and possesses numerous advantages:

1. High speed: a faster way to read and write to the disk than a fully parallel pickled scheme is difficult to imagine,
2. Ease of code and use: encapsulation is performed, the resulting code is largely independent of the `FEniCSx` version,
3. Independence of `PETSc` build: `FEniCSx` does most of its data management in `PETSc` which differentiates real and complex mode. Using `numpy` makes it easy to compute a baseflow in real mode, and read it back in complex mode.

However, it does mean that the saving scheme is not only number-of-processors dependent, but also requires meshes to always be read in the same order. Indeed, `FEniCSx` does the partitioning upon reading the mesh, and therefore reading meshes in a different order leads to a different partitioning and a `readStuff` failure.

4.1.4 Convergence relative to the grid

Many different meshes were tried over this PhD, trying various cell sizes, stretching ratios, different geometries for refined areas... There are so many parameters implied in the creation of an unstructured mesh that it would be impossible to exhaustively explore them all.

However, as every numerical physicist knows, studying the convergence of the employed scheme on the mesh is paramount. It is a necessary and important step in building confidence on produced results. Therefore a series of meshes with similar zones but differing smallest grid sizes were computed and ran through the code. In order to allow for better readability to the reader, these different meshes will be labelled by their number of elements, or triangles.

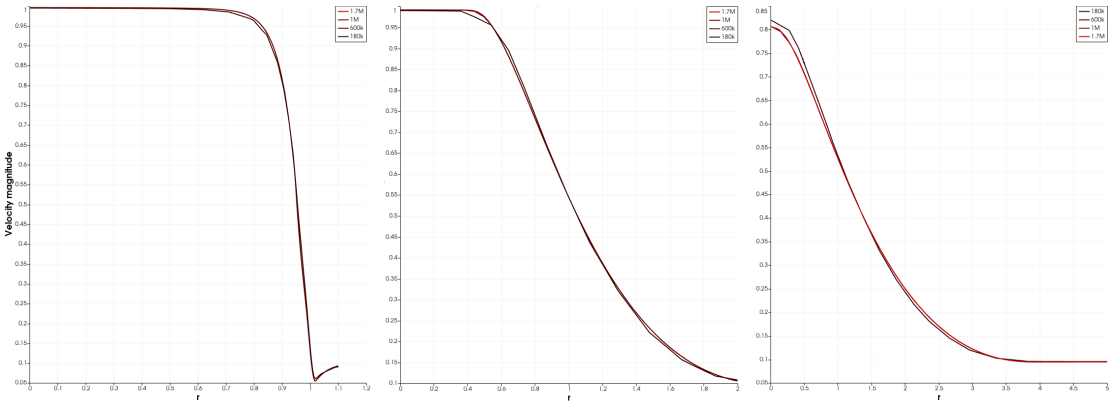

(a) $x = \epsilon$, (b) $x = 9$, (c) $x = 19$.

Figure 4.2: Velocity magnitude for a variety of slices at different numbers of elements.

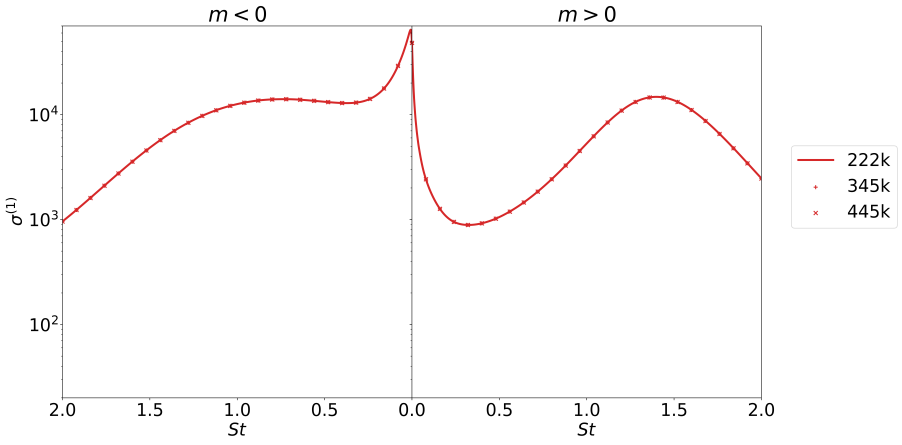

Figure 4.3: Gain curves for different number of elements for the case presented in section 3.2.1 and parameters $(Re; S; m) = (200,000; 1; -2)$.

Baseflow

For baseflow computations, convergence with respect to mesh refinement was verified at $S = 0$. In the usual manner, a very refined mesh was taken as reference, and it was checked on a few flow slices at constant x that results do converge quite quickly to the fine mesh as the number of elements increases, see figure 4.2. The number of elements considered here vary by almost a full order of magnitude.

An attempt was made at implementing a naive form of adaptive mesh refinement remains in the `SPYB` code as a work in progress.

Fluctuations

The choice was made to focus on gains instead to study fluctuations convergence, as this quantity was more accessible but also allowed for easier exploration of the parameter space. This time, swirl was maximised, and an azimuthal wavenumber of interest was chosen to compare at a range of frequencies. Results are displayed in figure 4.3 for a number of elements up to twice more than the mesh used for most of this study.

This brief analysis clearly demonstrates that the mesh used throughout chapter 3 at 222,000 elements is well converged.

σ_{ν_t}	C_{b1}	C_{b2}	C_{w1}	C_{w2}	C_{w3}	C_{v1}	C_S	κ
2/3	0.1355	0.622	$\frac{C_{b1}}{\kappa^2}+\frac{1+C_{b2}}{\sigma_{\nu_t}}$	0.3	2	7.1	0.3	0.41

Table 4.1: SA parameters in `OpenFOAM`.

4.2 Baseflow computation

`SPYB` was developed for an axisymmetric and steady baseflow, satisfying equations (3.19).

4.2.1 `OpenFOAM`

The Open Source code `OpenFOAM` was used to obtain the eddy viscosity field ν_t using the SA model as detailed in 3.2. To that end, the `simpleFoam` solver was used. This solver makes use of the canonical *SIMPLEC* algorithm introduced in [137], a consistent variant of the *SIMPLE* method presented in [98]. This algorithm will be presented in 1.

Using the Rhie-Chow interpolation, the momentum equation of (3.19) may be reformulated as $\underline{\underline{F}}\,\underline{U} = \underline{\underline{H}}(\underline{U}) - \underline{\nabla} P$. $\underline{\underline{F}}$ is diagonal, and one defines $\underline{\underline{H}}_1$ as its average in a neighbourhood $[H_1]_{ij} = \delta^i_j \sum_{k\in\mathcal{B}(i)} [F]_{kk}$.

Algorithm 1 Pseudo-code for the algorithm *SIMPLEC*.

$\underline{Q}_{BC} \leftarrow$ Boundary conditions
$\underline{Q} \leftarrow$ Initial conditions
$\underline{Q}^* \leftarrow \underline{Q}$
$\underline{Q}' \leftarrow \underline{Q} + \eta\underline{1}$
while $\left\|\underline{Q} - \underline{Q}'\right\| > \eta$ **do**
  $\underline{Q}' \leftarrow \underline{Q}$
  $\underline{U}^* \leftarrow$ solution of $\frac{1}{\alpha}\underline{\underline{F}}\,[\underline{U}^* - (1-\alpha)\underline{U}] = \underline{\underline{H}}(\underline{U}^*) - \underline{\nabla} P$ under U_{BC}
  $P \leftarrow$ solution of $\underline{\nabla}\cdot\left\{\underline{\underline{F}}^{-1}\underline{\underline{H}}(\underline{U}^*) - \left[\underline{\underline{F}}^{-1} - \left(\underline{\underline{F}} - \underline{\underline{H}}_1\right)^{-1}\right]\underline{\nabla} P^* - \left(\underline{\underline{F}} - \underline{\underline{H}}_1\right)^{-1}\underline{\nabla} P\right\} = 0$ under P_{BC}
  $\underline{U} \leftarrow \underline{\underline{F}}^{-1}\underline{\underline{H}}(\underline{U}^*) - \left[\underline{\underline{F}}^{-1} - \left(\underline{\underline{F}} - \underline{\underline{H}}_1\right)^{-1}\right]\underline{\nabla} P^* - \left(\underline{\underline{F}} - \underline{\underline{H}}_1\right)^{-1}\underline{\nabla} P$ under U_{BC}
  $P^* \leftarrow P$
end while
return $\underline{Q}$

Notice the use of a relaxation parameter α for velocity, but not for pressure. That is a hallmark of the *SIMPLEC* method. To resume the spirit of this algorithm, it uses a pseudo-time-march with a pressure-correction step, which implies setting boundary conditions for the pressure. The only difference with *SIMPLE* lies in the pressure correction. However, this single term change turns out to have a great effect on stability for the case of interest.

Since the eddy viscosity is the only result kept from these calculations, let us remind the SA equations instead as implemented in `OpenFOAM`

$$
\begin{aligned}
\nu_t &= \tilde{\nu} f_{v1},\\
\partial_t(\rho\tilde{\nu}) + U_i\partial_i(\rho\tilde{\nu}) &= \underline{\nabla}\cdot[\rho(\nu+\tilde{\nu})\underline{\nabla}\tilde{\nu}] + \frac{C_{b2}}{\sigma_{\nu_t}}\rho\left\|\underline{\nabla}\tilde{\nu}\right\|^2 + C_{b1}\rho\tilde{S}\tilde{\nu} - C_{w1}f_w\rho\frac{\tilde{\nu}^2}{\tilde{d}^2},\\
\tilde{S} &= \|\underline{\nabla}\times\underline{U}\| + \tfrac{\tilde{\nu}}{\kappa^2 d^2}f_{v2}, \qquad f_w = g\left(\tfrac{1+C_{w3}^6}{g^6+C_{w3}^6}\right)^{1/6},\\
f_{v2} &= 1 - \tfrac{\chi}{1+\chi f_{v1}}, \qquad g = r + C_{w2}(r^6 - r),\\
f_{v1} &= \tfrac{\chi^3}{\chi^3+C_{v1}^3}, \qquad r = \min\left(\tfrac{\tilde{\nu}}{\tilde{S}\kappa^2 d^2}, 10\right),\\
\chi &= \tilde{\nu}/\nu,
\end{aligned}
\tag{4.2}
$$

d being the local minimum distance to wall. The coefficients of the model are detailed in table 4.1. A few alternatives are reviewed in section 1.1.2.

To obtain the desired Reynolds number, it was increased gradually with logarithmic steps. Absolute as well as relative tolerance and relaxation parameter were decreased as well to improve performance, all the way to final relation parameter $\alpha = 0.97$, absolute tolerance $\eta = 10^{-12}$ and relative tolerance $\iota = 10^{-9}$. Because `OpenFOAM` accepts snippets of `C++` as boundary conditions of type `codedFixedValue`, a changing swirl intensity S was written as a function of `OpenFOAM` pseudo-time.

Critically, the presence of a non-negligible co-flow and a Dirichlet condition at the top boundary are necessary for convergence of the `OpenFOAM` pipeline. Fortunately, the co-flow can be reduced as iterations progress in the same manner that swirl intensity S is increased, using `codedFixedValue`. Because of the different meshes used as detailed in section 4.1.2, it was possible to pick a smaller domain for `SPYB` and limit the spurious influence from the top boundary.

As mentioned in section 3.2.2, the `OpenFOAM` setup is also available on GitHub.

4.2.2 `SPYB`

Because of small defects in the output from `OpenFOAM` invisible to the naked eye, the resulting flow could not be used as is in instability computations. A Newton solver was thus employed to obtain a baseflow satisfying (3.19) given the eddy-viscosity field ν_t provided by `OpenFOAM`, appropriately smoothed and truncated as detailed in 4.1.2.

`SPY` makes use of Taylor-Hood P2-P1 elements, which means that velocity is decomposed onto *Basix* polynomials of degree two, whereas as pressure is written as a sum of linear hat functions. The eddy viscosity is interpolated on a P1 element similarly to pressure.

This Newton solver also involved a relaxation parameter which was kept at $\alpha = 0.97$. Convergence occurred in under 10 steps for an absolute tolerance $\eta = 10^{-12}$ and a relative tolerance $\iota = 10^{-9}$ just like the rest of the calculation in both `OpenFOAM` and `SPYP`.

Another continuation scheme was used for the baseflow computation in `SPYB`, increasing first Reynolds number Re then swirl intensity S. A lower-upper solver was used with *MUMPS* as a preconditioner. The Navier-Stokes equations were solved in `FEniCSx` using a finite element framework in the weak form formulation of (3.19), writing real inner product $\langle \cdot, \cdot \rangle$ taking $\underline{v}$ and s as test functions of momentum equations and pressure

$$\forall \underline{y} \in \underline{\mathcal{H}}^1_Q, \underline{y} = \begin{bmatrix} \underline{v} \\ s \end{bmatrix}, \langle \underline{\nabla} \cdot \underline{U}, s \rangle + \left\langle \underline{\underline{\nabla U}}\ \underline{U}, \underline{v} \right\rangle - \langle P, \underline{\nabla} \cdot \underline{v} \rangle + \left\langle \nu \left(\underline{\underline{\nabla U}} + \underline{\underline{\nabla U}}^T \right), \underline{\underline{\nabla v}} \right\rangle = 0. \tag{4.3}$$

Here, $\underline{\nabla}$ is implemented in `helpers` as the axisymmetric operator in cylindrical coordinates.

See [56] for more details on finite elements methods for incompressible CFD. The weak form in equation (4.3) naturally gives the stress-free boundary condition at all boundaries Γ as defined in section 3.2.1 $P\underline{n} = \nu \left(\underline{\underline{\nabla U}} + \underline{\underline{\nabla U}}^T \right) \underline{n}$. Indeed, this quantity appears when performing an integration by parts on equation (4.3):

$$\begin{aligned} \forall \underline{y} \in \underline{\mathcal{H}}^1_Q, \underline{y} = \begin{bmatrix} \underline{v} \\ s \end{bmatrix}, 0 = \langle \underline{\nabla} \cdot \underline{U}, s \rangle + \left\langle \underline{\underline{\nabla U}}\ \underline{U} + \underline{\nabla} P - \underline{\nabla} \cdot \left[\nu \left(\underline{\underline{\nabla U}} + \underline{\underline{\nabla U}}^T \right) \right], \underline{v} \right\rangle \\ + \int_\Gamma \left[\nu \left(\underline{\underline{\nabla U}} + \underline{\underline{\nabla U}}^T \right) \underline{n} - P\underline{n} \right] \underline{v}^H \mathrm{d}l. \end{aligned} \tag{4.4}$$

Looking at equation (4.4), it becomes clear that it is impossible to satisfy this equation for any $\underline{v}$ without enforcing the boundary integral as well as the surface terms. As in section 3.2, the total viscosity $\nu = 1/Re + \nu_t$ accommodates an eddy viscosity and therefore varies in space, which prevents the usual elimination of the second term of the viscous stress as is usual when doing incompressible CFD.

Dirichlet boundary conditions are enforced using geometric indicator functions, collapsed subspaces and arbitrary interpolated profiles in `setup.py` files. `dolfinx.fem.locate_dofs_geometrical` provides degrees of freedom associated with a particular boundary and a particular collapsed subspace, `dolfinx.fem.dirichletbc` allows a specific boundary condition to be computed and stored in a `SPY` object using the encapsulation routine `SPY.applyBCs`. These boundary conditions are then passed to the `dolfinx.nls.petsc.NewtonSolver` in `SPYB`.

Should arbitrary Neumann or mixed boundary conditions be desired, it becomes necessary to change the weak form in equation (4.3). This was done over the course of this PhD but not retained in the final version of the `SPY` code.

There are several advantages to write matrices as complex forms over setting them up in the code explicitly:

- Compacity and clarity of the weak form,
- Ease to mix objects of different types, `int`, `dolfinx.fem.Function`, `ufl.TestFunction`...
- Automated handling of boundary conditions,
- Sparsity patterns and distribution amongst processors handled by `FEniCSx`,
- Natural `FEniCSx` syntax.

`FEniCSx` makes the difference between `ufl.TestFunctions` and `ufl.TrialFunctions` - test functions are the usual right hand side of inner products in weak forms, see [56] for more information on finite-element methods. Trial functions correspond to the space on which the solution is decomposed - after all, there is no mathematical requirement for these two spaces to be identical. This being said, in `SPY` the usual finite element paradigm of having identical test and trial function spaces and decomposition is retained.

In the code, `ufl.TestFunctions` and `ufl.TrialFunctions` are simply used as a shortcut to make it easier to write and assemble complex forms correctly. In the baseflow case, specifying $\underline{y}$ as a `ufl.TestFunction` is enough to ensure that the solution of a `dolfinx.fem.petsc.NonlinearProblem` solver is put into $\underline{Q}$. The difference between `ufl.TestFunctions` and `ufl.TrialFunctions` is more important when solving for the fluctuations, see 4.3.

Another subtlety in the weak form computation regards the volume element inside the inner product. Indeed, `FEniCSx` currently handles only Cartesian geometries, with a volume element `ufl.dx` formulated as $\mathrm{d}V = \mathrm{d}x\mathrm{d}y\mathrm{d}z$. This is not suited for cylindrical geometries that instead have $\mathrm{d}V = r\mathrm{d}x\mathrm{d}r\mathrm{d}\theta$. Therefore for all of the weak forms in `SPY`, the surface element underwent a multiplication by r to make it a volume element in the cylindrical sense `r*ufl.dx`. This multiplication is done after integration by parts, since the mathematics of this operation are independent of the coordinate system.

Even after the Newton calculations, it was found beneficial to undergo smoothing once again using equation (4.1) with a small coefficient $\mu = 10^{-4}$, specifically for the component U_r which regularly appears to be quite noisy.

At this point, it is legitimate to put into question the relevance of even using `OpenFOAM` in the first place. Only the turbulent viscosity field ν_t were used from its computations, and even then smoothed before being fed into another Newton solver... In the end though, looking at figure 4.4, differences between the `OpenFOAM` and `SPYB` results are undeniable but remain slim. Most importantly, the flow retains a short potential core reminiscent of an actual turbulent jet, a feature that might be lost if eddy viscosity was included in the Newton solver directly.

A more detailed comparison on specific slices is presented in 4.5. There are differences, but they remain contained to few percent.

4.2.3 Performance

A few speed-ups were implemented to improve performance and reduce computation time for abseflow computations. Since the linearised NSE is the basis for the linear methods of interest in `SPYP` as detailed in section 1.2, the Jacobian of the baseflow equations is computed explicitly and passed to the solver. It takes the form of equation (4.14) with a real inner product and $m = 0$.

Another implemented feature is the change of boundary conditions according to the required swirl intensity S which avoids recomputing boundary conditions every time. Instead, only the inlet boundary condition for the θ component is computed at every iteration.

The usual trade-off between stability and convergence speed for a Newton solver made it necessary to use a relaxation parameter $\alpha = 0.97$.

4.3 Numerical linear instability analysis

A quick word about dimensions is needed here. Whenever modelling, there is a strong case to be made in favour of reducing the problem to its substantial core. Making use of symmetry, using a computational

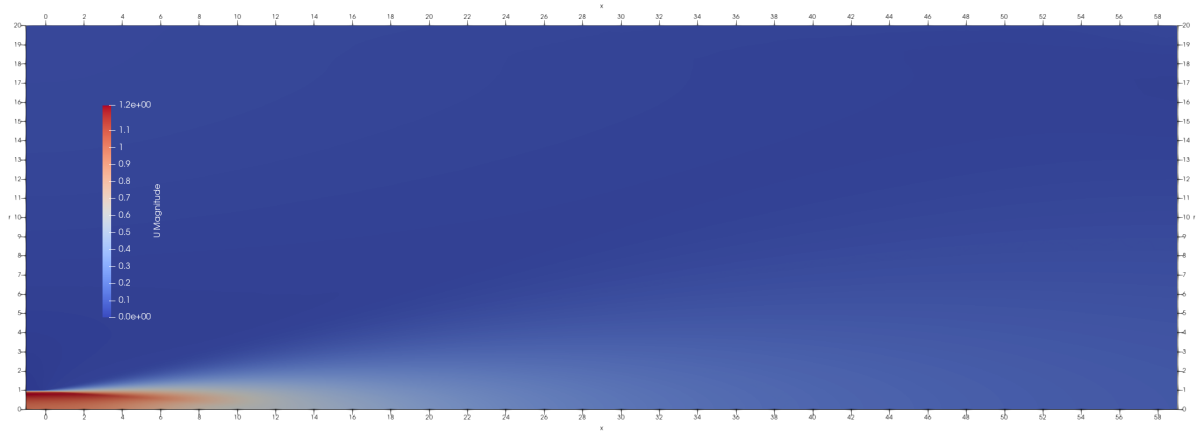

(a) `OpenFOAM`,

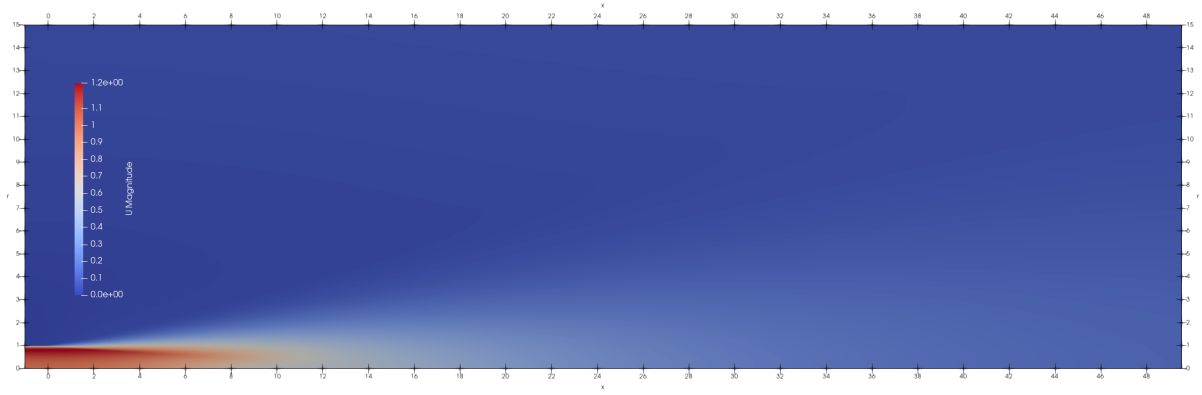

(b) `SPYP`.

Figure 4.4: Baseflow magnitudes for the $(Re; S) = (200,000; 1)$ case studied in 3.4.3.

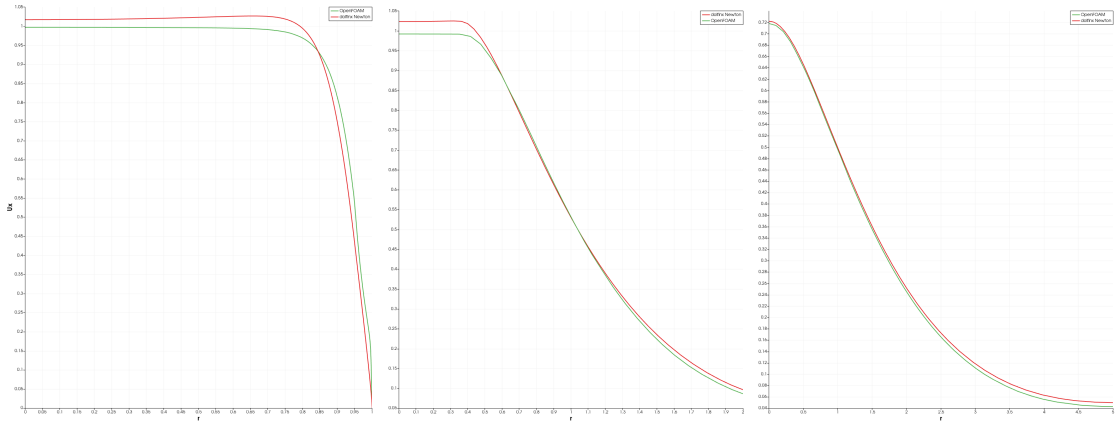

(a) $x = \epsilon$, (b) $x = 9$, (c) $x = 19$.

Figure 4.5: Axial velocity for a variety of slices from `OpenFOAM` and `SPYB`'s Newton computation using the `FEniCSx` library `dolfinx`.

domain with varying resolution, and cutting out unnecessary dimensions can be understood in the same spirit as the choice of RANS methods over the alternatives as discussed in section 1.1.1, namely to get the most insight out of limited computational resources. However, it seems that the three dimensions of fluctuations are crucial even on a two-dimensional flow in order to capture all phenomena, as established in [34] even for the simplest flow by LTSA.

Indeed, the well-known Squire theorem established in [127] states that the most unstable perturbations of an incompressible shear flow are two-dimensional, but that statement only hold true for a very simple baseflow $\underline{U} = U(y)\underline{e}_x$ and is not expected to be relevant for the general flows considered here. Furthermore, it considers only the most amplified mode in the stability analysis sense and misses out on constructive interactions between non-orthogonal modes, as argued in [22].

Notice that there is no contradiction between the existence of lift-up and Squire's theorem. Both these results apply to inviscid baseflows written as $U(y)\underline{e}_x$. [34] states that there exists a three-dimensional instability growing linearly in time in such a flow, which exploits LU. Squire's theorem establishes that the most unstable perturbation is two-dimensional in a LTSA framework. Therefore, LU is simply not the way to obtain the fastest growing perturbation for such flows in a LTSA sense.

Even without this shortfall, Squire's theorem does not apply to a general flow. Therefore, three-dimensional fluctuations are considered in `SPYP`.

4.3.1 A word on matrices

The mathematics of resolvent analysis have been presented in section 1.2.4. Recall that the method hinges on the formulation of the operator of the same name

$$\underline{\underline{R}} = \underline{\underline{H}} \left(\underline{\underline{L}} - i\omega \underline{\underline{M}} \right)^{-1} \underline{\underline{B}} \tag{4.5}$$

or more precisely on the computation of $\underline{\underline{R}}^H \underline{\underline{W}}_\psi \underline{\underline{R}}$, see section 3.3.2. Most of the matrices are implemented as assembled weak forms using the complex form of `PETSc`, using the Hermitian inner product $[\cdot,\cdot]$.

Indeed, the matrix $\underline{\underline{M}}$ amounts to assembling over the space of the entire Taylor-Hood element

$$\forall (\underline{q},\underline{y}) \in \underline{\mathcal{H}}^1_Q \times \underline{\mathcal{H}}^1_Q, \underline{q} = \begin{bmatrix} \underline{u} \\ p \end{bmatrix}, \underline{y} = \begin{bmatrix} \underline{v} \\ s \end{bmatrix}, [\underline{u},\underline{v}] = \underline{q}^H \underline{\underline{M}}\, \underline{y}. \tag{4.6}$$

Similarly, $\underline{\underline{W}}_\phi$ is written as an inner product over a smaller space containing only the P2 elements associated to velocity

$$\forall (\underline{w},\underline{z}) \in \underline{\mathcal{H}}^1_U \times \underline{\mathcal{H}}^1_U, [\underline{w},\underline{z}] = \underline{w}^H \underline{\underline{W}}_\phi \underline{z}. \tag{4.7}$$

Constraints and indicator functions

$\underline{\underline{W}}_\psi$ and $\underline{\underline{W}}_\phi$ would be identical except if an indicator function `indic_u` is provided. Such a function once interpolated onto the mesh is denoted $\mathbb{1}_\psi$ and appears in the hermitian product. In practice, matrices $\underline{\underline{H}}^H \underline{\underline{W}}_\psi \underline{\underline{H}}$ were bundled together with a weak form more similar to that of $\underline{\underline{M}}$

$$\forall (\underline{q},\underline{y}) \in \underline{\mathcal{H}}^1_Q \times \underline{\mathcal{H}}^1_Q, \underline{q} = \begin{bmatrix} \underline{u} \\ p \end{bmatrix}, \underline{y} = \begin{bmatrix} \underline{v} \\ s \end{bmatrix}, [\mathbb{1}_\psi \underline{u},\underline{v}] = \underline{q}^H \underline{\underline{H}}^H \underline{\underline{W}}_\psi \underline{\underline{H}}\, \underline{y}. \tag{4.8}$$

In the absence of `indic_u`, $\underline{\underline{H}}^H \underline{\underline{W}}_\psi \underline{\underline{H}}$ is stored as a pointer to $\underline{\underline{M}}$ to save memory. This is the case for most of the computations presented in chapter 3 with the exception of section 3.4.4 where the importance of streaks was quantified using constraints on $\underline{\underline{W}}_\psi$.

Because of the choice of a compact `HHWpsiH` matrix, the `R_class` object does not implement $\underline{\underline{R}}$ as present in relation (4.5) but instead a version without an extractor $\tilde{\underline{\underline{R}}} = \left(\underline{\underline{L}} - i\omega \underline{\underline{M}} \right)^{-1} \underline{\underline{B}}$. $\underline{\underline{B}}$ may also be weighted according to `indic_f` interpolated as $\mathbb{1}_\phi$

$$\forall (\underline{q},\underline{z}) \in \underline{\mathcal{H}}^1_Q \times \underline{\mathcal{H}}^1_U, \underline{q} = \begin{bmatrix} \underline{u} \\ p \end{bmatrix}, [\mathbb{1}_\phi \underline{u},\underline{z}] = \underline{q}^H \underline{\underline{B}}\, \underline{z}. \tag{4.9}$$

Indicator functions `indic_f` are useful to prevent spurious forcing. As stated in section 3.3.2, a region with the indicator function `indic_f` going to zero is not forced. This turned out to be critical

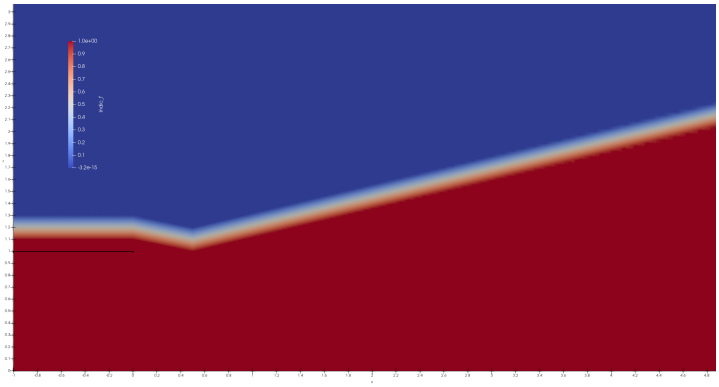

Figure 4.6: Indicator function `indic_f` used for the calculations in chapter 3. The nozzle walls are shown in black.

in the calculations, as restricting the forcing turned out to be necessary to obtain physically meaningful resolvent modes. Indeed, with no constraints on the forcing, oscillations arose on the top left corner even when increasing mesh refinement or cutting off eddy viscosity in that region.

The current interpretation of this is that the SA model produces an eddy viscosity ν_t that is strongly oscillating as it grows in the almost quiescent region, and this leads to an opportunity for forcing to grow on the top of the shear layer in a very unstructured and unphysical manner.

The only solution that worked in practice was introducing a constraint on the forcing relatively close to the nozzle. Such an approach has been followed in other studies such as [44], where forcing was only allowed to exist in the nozzle. The mathematical formulation of the chosen function goes

$$l(\underline{x}_a, \underline{x}_b, \underline{x}) = \frac{y_b - y_a}{x_b - x_a}(x - x_a) + y_a - y, \tag{4.10}$$

$$s(d) = \min(\max(5d + 1, 0), 1), \tag{4.11}$$

$$\mathbb{1}_\phi(\underline{x}) = \begin{cases} s(y_0 - y) & \text{if } x < x_0, \\ s(l(\underline{x}_0, \underline{x}_1, \underline{x})) & \text{if } x_0 \leq x \leq x_1, \\ s(l(\underline{x}_1, \underline{x}_2, \underline{x})) & \text{else,} \end{cases} \tag{4.12}$$

using constants

$$\underline{x}_0 = \begin{bmatrix} 1 \\ 1.1 \end{bmatrix}, \quad \underline{x}_1 = \begin{bmatrix} 1.5 \\ 1 \end{bmatrix}, \quad \underline{x}_2 = \begin{bmatrix} 12 \\ 3.5 \end{bmatrix} \tag{4.13}$$

In effect, equation (4.10) simply gives the signed distance to a line between $\underline{x}_a$ and $\underline{x}_b$. Equation (4.11) scales such a distance d by a factor of five and saturates it at zero and one. The resulting forcing function in equation (4.12) is defined piecewise as these saturated slopes, leading to figure 4.6. This masking allows forcing to exist in a small region above the nozzle but cut inside the shear layer before going up again, preventing forcing from existing at the interface between the coflow and the shear layer.

Thus, the indicator function enforces that forcing only exists in regions where the eddy-viscosity is relatively smooth, and leaves some space around the nozzle tip for perturbations to grow. Even though forcing was allowed to exist father from the nozzle, in practice forcing structures were always found clustered around the nozzle, which makes sense given this is where the strongest baseflow gradients are located.

The final weighting of forcing takes effect quite close to the structures observed in section 3.4.4. However, the results are resilient to small changes to the forcing mask, and the modes do not appear cut-off by the weighting. Any significant radial increase of the forcing envelope was observed to lead to spurious oscillations, so a fine balance had to be struck between over-restricting the forcing and abandoning the low frequencies to noise.

It must be stressed that the choice of the system 4.12 was a constraint of the numerical pipeline, an arbitrary choice that seemed to remove the numerical issues while not affecting the resulting structures too much. There is an argument to be made to make the forcing box more physical, basing it for instance

on eddy-viscosity or another indicator of turbulence. Such a box would be more restrictive which could complicate interpretative of the response modes, but it would also allow for a much smaller resolvent system which could improve performance.

The linearised Navier-Stokes operator

The most physically meaningful matrix remains $\underline{\underline{L}}$, of course. The linearisation of Navier-Stokes is by far the most challenging one. It was implemented as a matrix-free `PETSc` object to avoid ever inverting it directly. The weak form of $\underline{\underline{L}}$ goes

$$\forall(\underline{q},\underline{y}) \in \underline{\mathcal{H}}^1_Q \times \underline{\mathcal{H}}^1_Q, \underline{q} = \begin{bmatrix} \underline{u} \\ p \end{bmatrix}, \underline{y} = \begin{bmatrix} \underline{v} \\ s \end{bmatrix}, [\underline{\nabla}_m \cdot \underline{u}, s] + \left[\underline{\underline{\nabla_0 U}}\ \underline{u} + \underline{\underline{\nabla_m u}}\ \underline{U}, \underline{v} \right] - [p, \underline{\nabla}_m \cdot \underline{v}] + \left[\nu \left(\underline{\underline{\nabla_m u}} + \underline{\underline{\nabla_m u}}^T \right), \underline{\underline{\nabla_m v}} \right] = \underline{q}^H \underline{\underline{L}}\, \underline{y}. \tag{4.14}$$

It is critical to enforce $m = 0$ on the baseflow gradient as it is axisymmetric. The test function $\underline{v}$ however is also expected to have an azimuthal decomposition. The $\underline{\nabla}_m$ operator accounts for derivatives in the azimuthal direction and handles complex numbers, which is the main draw of `FEniCSx` compared to its predecessor `FEniCs` that was used in Chuhan's `SPY` code.

Here the previous comment about `ufl.TrialFunctions` in section 4.2.2 becomes critical. In order to ensure that the $\underline{\underline{L}}$ operator is properly formed, with $\underline{Q}$ appearing as a constant and the solution associated to $\underline{q}$, the latter is prescribed as a `ufl.TrialFunction`.

Boundary conditions are handled as `dolfinx.fem.dirichletBC` objects, which are provided by the user and subsequently enforced on the $\underline{\underline{L}}$ and $\underline{\underline{M}}$ matrices.

To stabilise and regularise, or not ?

When computing modes at higher and higher Reynolds number, the quality of obtained resolvent modes degrades, and spurious oscillations appear. These oscillations are most marked inside the nozzle for the case detailed in section 3.2.1. It was hypothesised that the problem originated from the centred finite difference scheme implemented in `FEniCSx`, and an attempt was made to address this using the Streamline Upwind Petrov-Galerkin (SUPG) formulation detailed in [21], as well as the "grad-div" method perused in [37].

Indeed, it is known that centred finite difference schemes have a tendency to produce when convection becomes strong and the grid Peclet number becomes large. This is illustrated in figure 4.7 for the toy problem

$$U\partial_x u = \nu \partial_x^2 u, \quad \text{with} \quad \begin{cases} u(0) = 0, \\ u(1) = 1. \end{cases} \tag{4.15}$$

Both these techniques involve changing the test functions in relation (4.14). SUPG amounts to the operation $\underline{v} \leftrightarrow \underline{v} + \tau_{SUPG}\, \underline{\underline{\nabla v}}\, \underline{u}$ which can be understood as introducing a bias in centred finite difference methods to better handle strongly convective flows.

On the other hand, "grad-div" performs a substitution more akin to $s \leftrightarrow s + \tau_{GD} \underline{\nabla} \cdot \underline{v}\, \underline{\nabla} \cdot \underline{u}$, which can be understood as a stricter enforcement of fluctuations incompressibility. Both these methods involve quite complicated prefactors τ_{SUPG} and τ_{GD}. More information on these two methods may be found in [29].

In the end, it turned out that a `FEniCSx` update removed these oscillations as long as the naive weak form proposed in (4.3) was not multiplied by r. This multiplication was introduced as a way to remove the $r = 0$ singularity in the equations, however with the update this precaution proved to be unnecessary. No special treatment of the axis of symmetry is therefore performed in $\underline{\underline{L}}$ at the time of writing.

4.3.2 Temporal stability analysis

`SPYP` is capable of performing the procedure described in section 1.2.2 as GTSA. Because of the choice to keep $\underline{\underline{L}}$ as a matrix-free object, this severely constrains the possibilities for eigenpair selection in the `slepc4py.SLEPc.EPS` object, basically imposing a shift and `EPS.Which.TARGET_MAGNITUDE` or

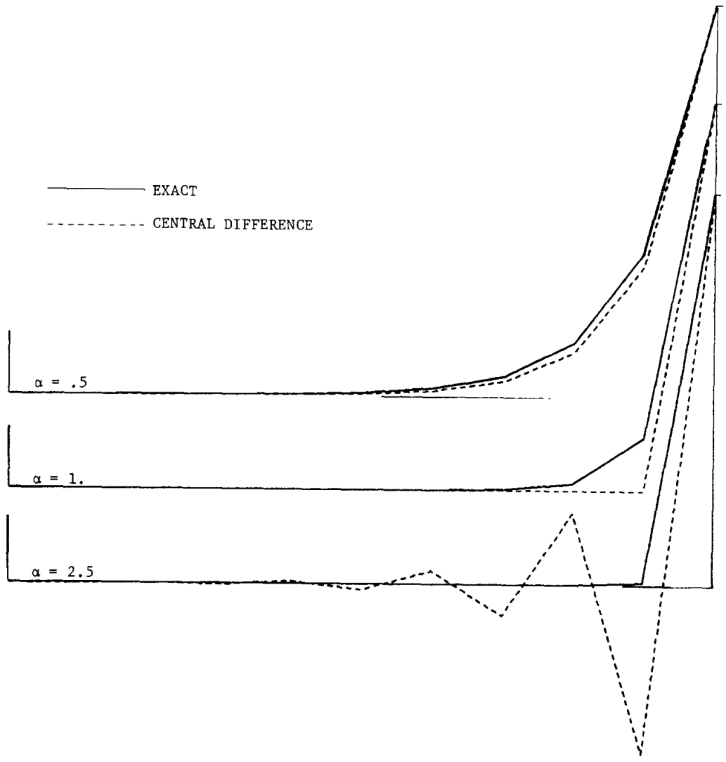

Figure 4.7: Figure 2.1 in [21] representing exact and approximate centred finite difference solutions to problem (4.15) for different grid Péclet number $\alpha = Uh/2\nu$.

`EPS.Which.TARGET_REAL`. In its current version, `SPYP` therefore requires a shift to compute eigenvalues around.

In other words, a Spectral Transform of type `shift-invert` is a requirement of previous design choices. The focus was put on computations around zero with a tiny positive shift $\varepsilon = 10^{-6}$ to look for the most unstable modes in the flow. Indeed, the flow was expected to be modally stable for all the regimes considered in chapter 3 and an extensive eigenvalue search yielded no unstable mode.

Problem type was specified as an `EPS.ProblemType.PGNHEP`, which means that the solver is encouraged to leverage the semi-definite symmetric nature of $\underline{\underline{M}}$. It turns out this does not lead to the eigensolver treating $\underline{\underline{M}}$ as a mass matrix for a new hermitian product in which the Rayleigh quotient would be computed as [112, section 3.4.3] could lead to believe. Instead the eigenvalue problem is finally formulated as

$$\begin{aligned} \Omega\, \underline{\underline{M}}\, \underline{x} &= \underline{\underline{L}}\, \underline{x}, \\ \Rightarrow (\Omega - \varepsilon)\, \underline{\underline{M}}\, \underline{x} &= (\underline{\underline{L}} - \varepsilon\, \underline{\underline{M}})\underline{x}, \\ \Rightarrow \left(\underline{\underline{L}} - \varepsilon\, \underline{\underline{M}}\right)^{-1} \underline{\underline{M}}\, \underline{x} &= \frac{1}{\Omega - \varepsilon} \underline{x} \end{aligned} \tag{4.16}$$

according to [112, equation (3.7)].

A lower-upper decomposition was used as a pre-conditioner for the `KSP` object associated to the `EPS` object which is concerned with the matrix $\underline{\underline{L}} - \varepsilon\, \underline{\underline{M}}$. This drives up computational costs significantly. `MUMPS` was leveraged to make the most of parallelism. The same absolute and relative tolerance $\eta = 10^{-12}$ and $\iota = 10^{-9}$ were imposed as elsewhere.

4.3.3 Resolvent analysis

The setup of the `slepc4py.SLEPc.EPS` object was similar to section 4.3.2, with the important difference that `shift-invert` was no longer necessary here. Because of the choice to operate on the $\underline{\underline{R}}^H\, \underline{\underline{W}}_\psi\, \underline{\underline{R}}$

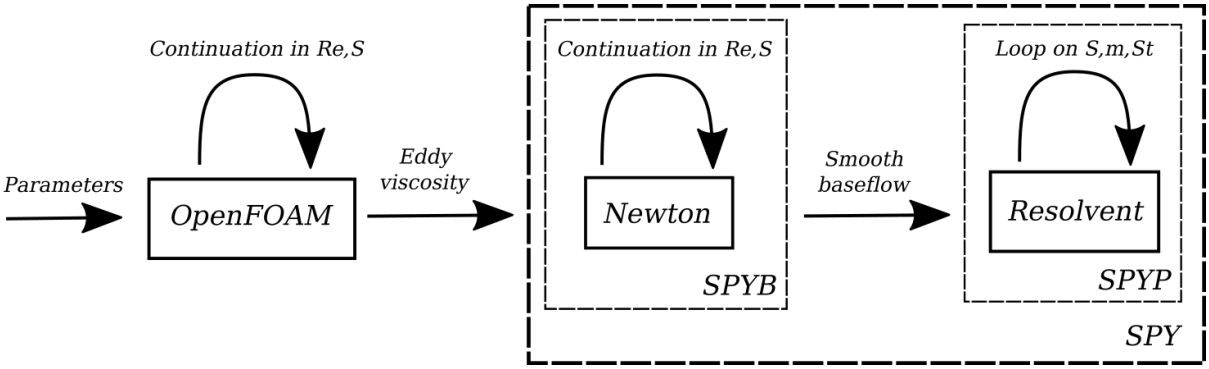

Figure 4.8: Schematics of the full computational process.

matrix instead of $\underline{\underline{R}}$ directly, the left-hand side of the eigenvalue problem is by design hermitian and its type could be specified as `EPS.ProblemType.GHEP`, opening the door to faster algorithms. Viewed from the machine, resolvent analysis was performed as

$$\underline{\underline{W}}_{\phi}^{-1}\,\underline{\underline{R}}^{H}\,\underline{\underline{W}}_{\psi}\,\underline{\underline{R}}\,\underline{x} = \sigma^2\underline{x} \tag{4.17}$$

according to [112, equation (3.4)]. See section 3.3 for the associated reasoning.

The inverse of $\underline{\underline{W}}_{\phi}$ was performed using a Conjugate Gradient method, making use of its symmetric definite positive nature. The response modes $\underline{\psi}^{(i)}$ were simply obtained as

$$\underline{\psi}^{(i)} = \frac{1}{\sigma^{(i)}}\,\underline{\underline{R}}\,\underline{\phi}^{(i)} \tag{4.18}$$

4.3.4 Post-processing

Most of the figures presented in chapter 3 were produced directly using visualisation routines, which are available for two-dimensional cuts at constant x or in the $x-r$ plane as well as in three dimensions.

Three-dimensional visualisation was performed using the `Plotly` library and isosurfaces. The latter cannot handle irregular meshes and thus coarse regular meshes were devised for visualisation purposes in `cases/nozzle/print/grids_3d.py`. Designed with a specific regime in mind, these Cartesian grids were then projected onto the $\theta = 0$ plane to be evaluation on the $x-r$ plane using the usual coordinate transform $r^2 = y^2 + z^2$, and enriched with azimuthal information using $\theta = \arctan_2(z/y)$. Animations were devised to visualise modes rotation as well.

4.3.5 Performance

The entire process to obtain resolvent modes is schematically presented in figure 4.8. Overall, the most time-consuming part of the process is clearly the last one involving `SPYP`, if only because every meaningful resolvent analysis involves a handful of azimuthal wave-numbers as well as easily dozens of different frequencies. For every one of these points in figures such as 3.13 or 3.20 `SPYP` must compute a lower-upper decomposition of the matrix $\underline{\underline{L}} - i\omega\,\underline{\underline{M}}$ using a `KSP` object of the `petsc4py` library. The Kolmogorov complexity of the general lower-upper algorithm goes like $O(n^3)$, with n numbering in the hundreds of thousands of points for the case detailed in chapter 3. Every such operation may take a full minute even using a large number of processors.

It goes without saying that as many operations as possible were kept out of the main loop on S, m and St. The matrices $\underline{\underline{B}}$, $\underline{\underline{W}}_{\phi}$, $\underline{\underline{H}}^{H}\,\underline{\underline{W}}_{\psi}\,\underline{\underline{H}}$ and $\underline{\underline{M}}$ can be assembled only once for a given mesh, and the matrix $\underline{\underline{L}}$ only depends on the azimuthal wave-number not on frequency, though the full resolvent does.

To mitigate costs further, a memoisation approach was thoroughly followed at all steps of the process, exchanging disk space for computation time. Every time `SPYB` computes a baseflow or `SPYP` computes a mode, it is written to file. If at a later time the library is required to compute it again, it will instead read the saved file.

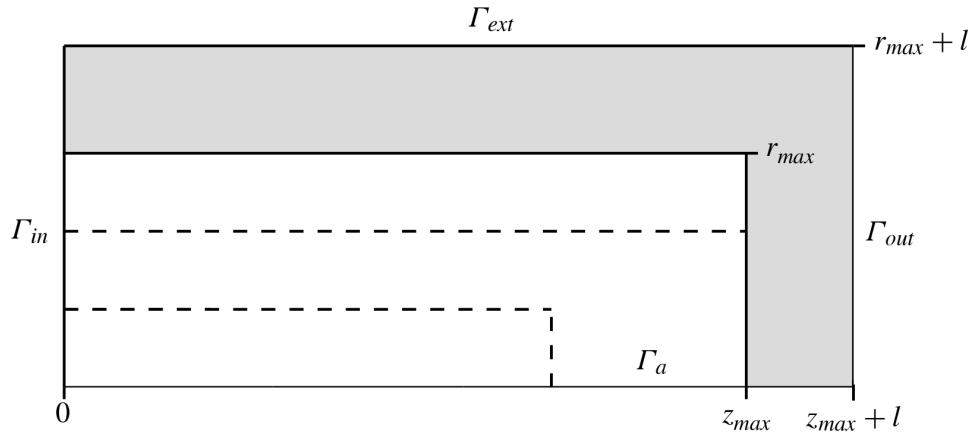

Figure 4.9: Figure 1 of [80] with case schematics.

Another attempt at improving performance was made using `FEniCSx`'s *Just in Time Compiler*. Even though `FEniCSx` is a `python` library, it implements matrices and vectors on the fly as `C` objects to enable faster executions of vector product operations. It is possible to tweak that compilation in order to increase performance, by specifying the correct parameters to the compiler.

4.4 Validation cases

In this section results from the developed code will be compared to known publications. This section aims to prove the validity of design choices outlined in sections 3.2.1, 3.2.2, 3.3.2 and chapter 4 as a whole, not introducing new phenomena. The relevance of `SPY` will be demonstrated iteratively, by considering cases of increasing complexity.

4.4.1 Baseflow

The first, simplest validation case concerned the Newton solver of `SPYB`. An axisymmetric flow as simple as the Grabowski-Berger vortex was taken as a first reference from [80]. This usual baseflow may be written at the input as

$$\underline{U}(r) = \underline{e}_x + S\underline{e}_\theta \begin{cases} r(2-r^2) & \text{if } r \leq 1 \\ 1/r & \text{else} \end{cases} \tag{4.19}$$

with the swirl intensity S as a parameter.

This case is simple, with a rectangular domain presented in figure 4.9 including sponge zones of varying Reynolds numbers with a minimum of $Re = 200$. Boundary conditions are stress-free at the right border Γ_{out}, and a conveyor belt at the top Γ_{ext}. The axis of symmetry was handled in the same way as in section 3.3.2.

As one can see in figure 4.10, `SPYB` is capable of reproducing the chosen indicator of vortex breakdown, namely minimum axial velocity. Furthermore, it finds a critical swirl within 0.01 of $S_c = 0.89$ from [80]. This grants confidence in `SPYB` and its Newton solver when it comes to computing swirling flows.

4.4.2 Eigensolver

The second validation case is the natural continuation of the previous one and concerns the GTSA routines. This is not directly linked with the reasoning developed in section 3.3, but it relates to proper construction of the $\underline{\underline{L}}$ operator.

The case is identical to the one presented in the previous section 4.4.1. Figure 4.11 reproduces part of the spectrum presented in [80] and most importantly captures the same unstable eigenvalue. Indeed, the only difference between the two graphs seems to be undersampled by `SPY`, which performs eigenvalue calculations around a series of shifts to efficiently compute a spectrum. This means that the values

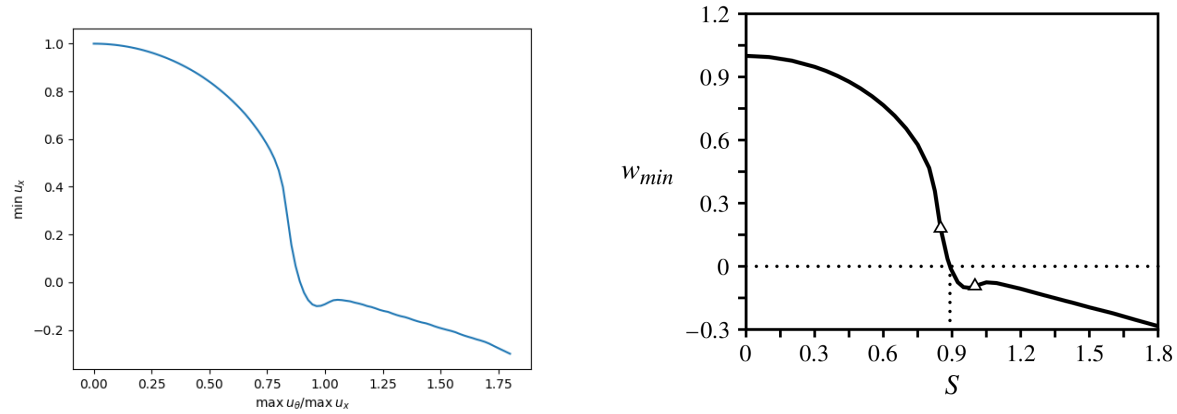

(a) SPYB result, (b) Figure 3.(a) of [80].

Figure 4.10: Graph of minimum axial velocity as a function of swirl intensity S for $Re = 200$.

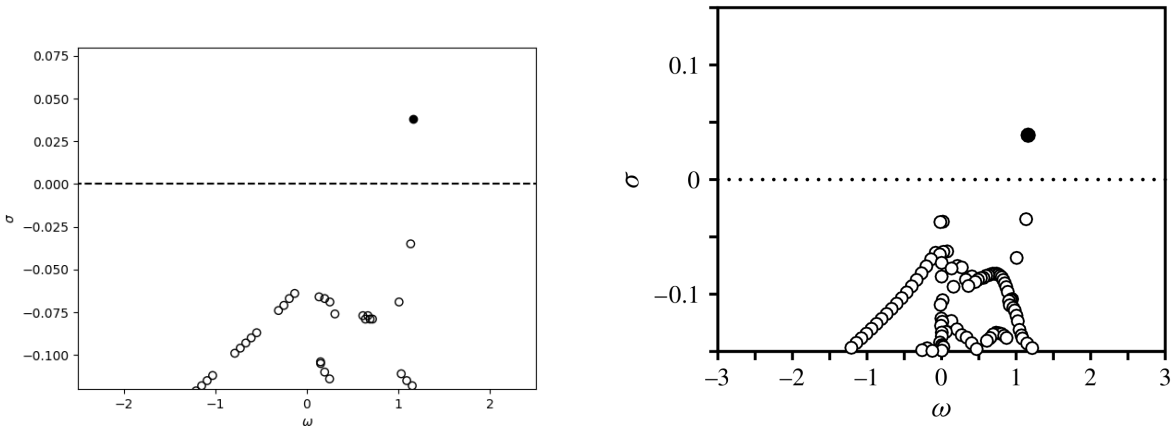

(a) SPYP result, (b) Figure 7.(a) of [80].

Figure 4.11: Eigenvalues plot for the Grabowski-Berger vortex, $(Re; S; m) = (200; 1; -1)$.

computed on figure 4.11a are naturally clustered around shifted points, especially for $\sigma < 0$ where a continuum of very close eigenvalues exist.

The Grabowski-Berger configuration is also studied in [43, 96, 97, 105, 115]. Indeed, the last study performed a DNS of this configuration, which made its analysis all the more convenient for other researchers.

The clustering of SPYP values around points regularly spaced in a grid across the domain is a natural consequence of the shift-invert scheme presented in section 4.3.2. This was considered sufficient proof that SPYP constructs $\underline{\underline{L}}$ and performs GTSA convincingly on swirling flows.

4.4.3 Resolvent

As an intermediate step towards the turbulent jet, the next case features a straight laminar jet. This case includes a wall on the left-hand side, as presented in figure 4.12. For this reference case, the focus will be on the laminar part of the study [44] at $Re = 10^3$ with an inflow profile $\underline{U} = \tanh[5(1-r)]\underline{e}_x$ at Γ_i. The wall Γ_w has no-slip boundary condition attached, Γ_o and Γ_t are considered stress-free boundaries.

A resolvent calculation on the same domain with the same baseflow produced an almost identical gain curve, as is readily visible in figure 4.13. This establishes that SPYP is capable of handling resolvent analysis on laminar straight jets.

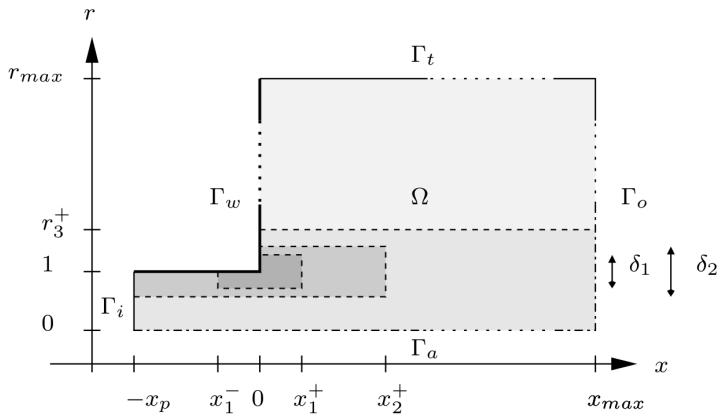

Figure 4.12: Figure 1 of [44] with case schematics.

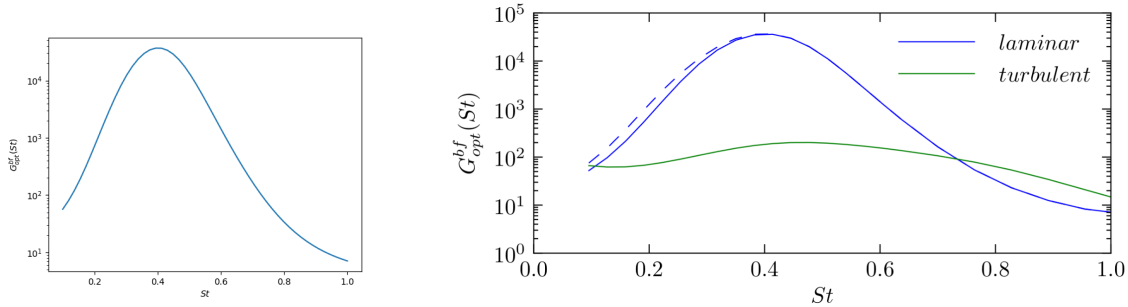

(a) `SPYP` result, (b) Figure 6.6 of [45].

Figure 4.13: Gains plot for a laminar jet for $(Re; m) = (10^3; 0)$.

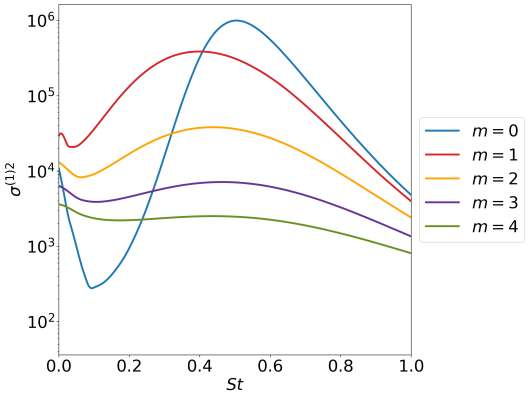

(a) SPYP result,

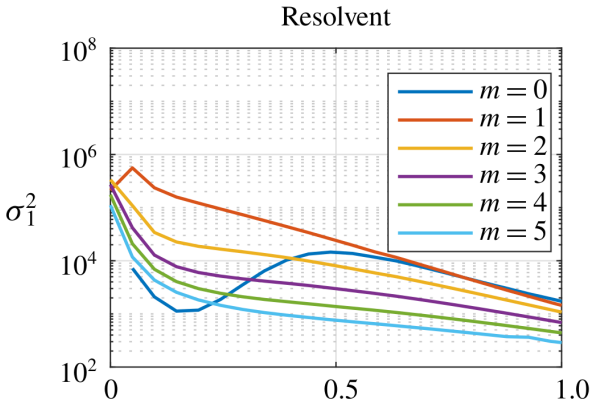

(b) Figure 4 b) of [101].

Figure 4.14: Squared gains plot for a turbulent straight jet with eddy viscosity $Re = 4 \cdot 10^5$.

4.4.4 Turbulent jet

The closest validation case to the one described in section 3.2.1 is the straight jet based on [101]. Here, the full computational chain described in figure 4.8 was used, making use of OpenFOAM, smoothing, *et caetera*. Computation were done similarly to chapter 3 with $S = 0$ but to better compare with the reference, the nozzle was cut out and calculations performed on $x \in [0; 49]$.

Figure 4.14 compares the two gain curves. This graph differs notably from the reference - gains are lower than expected, the peak of the $m = 0$ curve happens at a higher frequency, and the other curves show a marked increase before the expected monotonic decrease.

A qualitative comparaison of response and forcing modes was also performed in figure 4.15, which is to be compared to figure 4.16. These structures are qualitatively very close to the reference, though somewhat shorter.

There are several points where our model substantially differs from the reference:

- Baseflows come from different methods - one is the mean flow result of a LES calculation, the other a RANS process,
- Eddy viscosity models also differ, one being a length scale model and the other being the SA model. The fields are similar overall with comparable amplitude, but SA does not decays with x like the lengthscale model of [101] does, see figure 4.17,
- Flow profiles are dissimilar, with a much thinner shear layer in this work - see figure 3.10 for a quantitative comparaison.

The OpenFOAM results presented in chapter 3 are made dimensionless with respect to R. In figure 4.17 the reference length scale is taken to be D instead to allow for easier comparison.

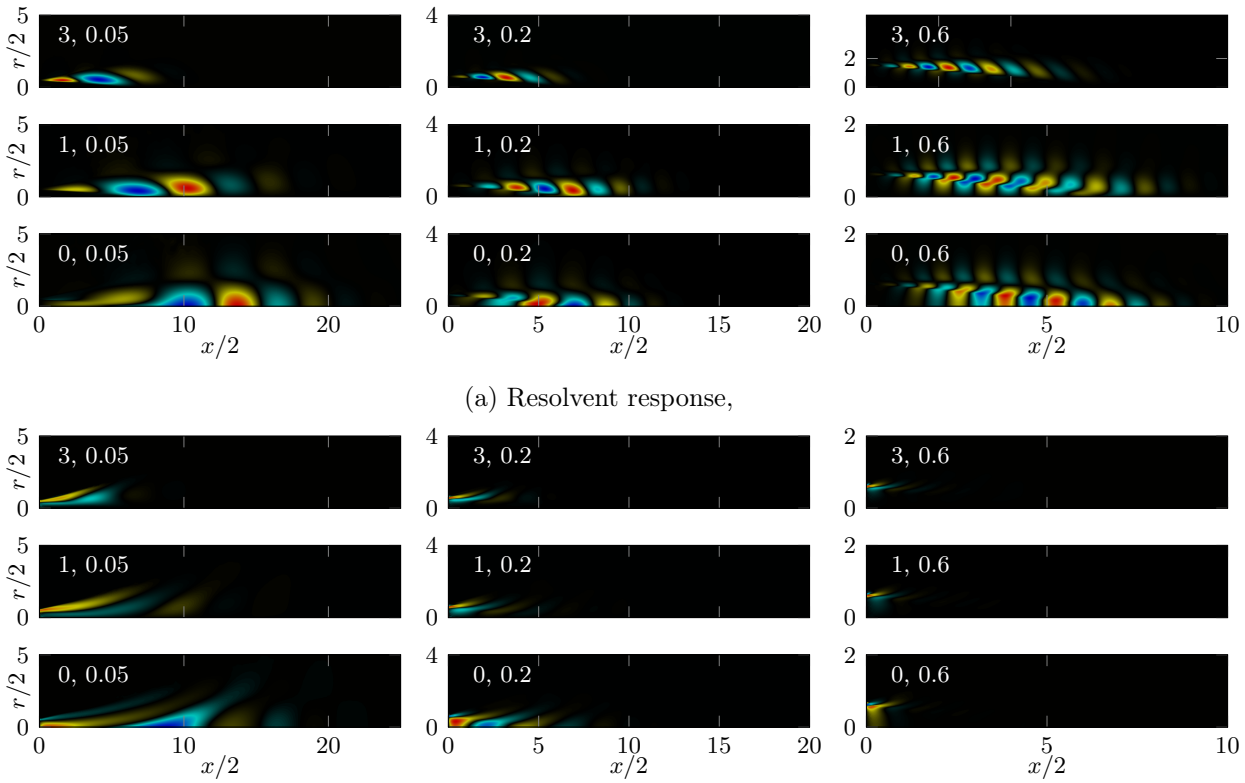

(a) Resolvent response,

(b) Resolvent forcing.

Figure 4.15: Resolvent modes for $(Re; m; St) \in \{4 \cdot 10^5\} \times \{0; 1; 3\} \times \{0.05; 0.2; 0.6\}$ obtained using `SPYP`. Parameters m and St are provided for every graph at the top left. Scaling is adjusted to ease comparaison to figure 4.16.

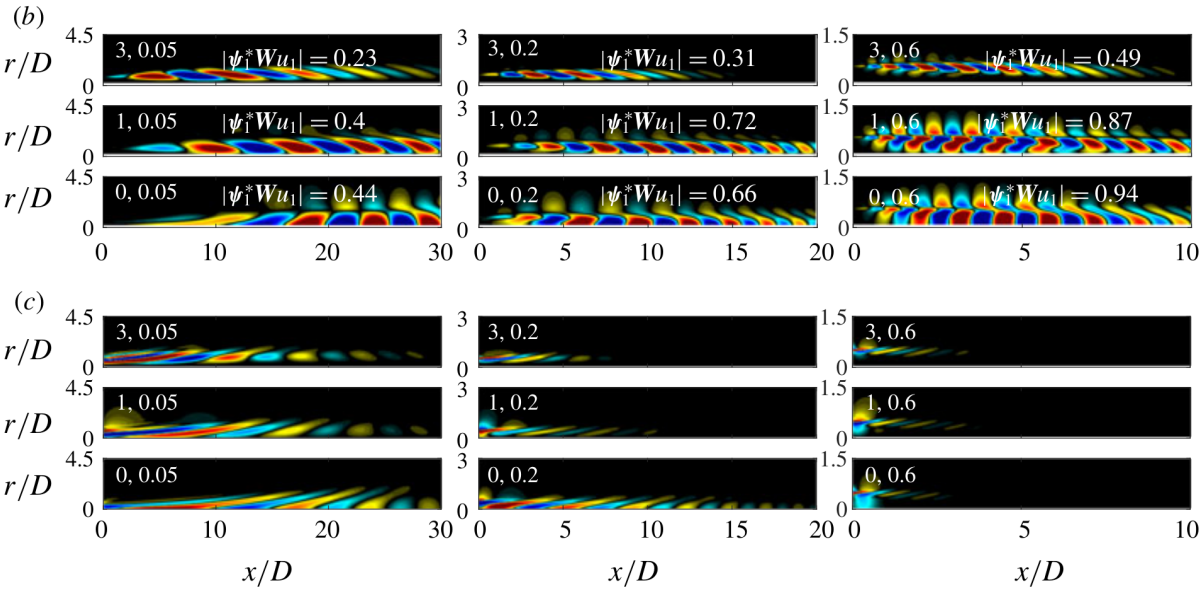

Figure 4.16: Excerpt of figure 9 of [101] showing resolvent response *(b)* and forcing *(c)* modes for a turbulent straight jet with eddy viscosity $Re = 4 \cdot 10^5$.

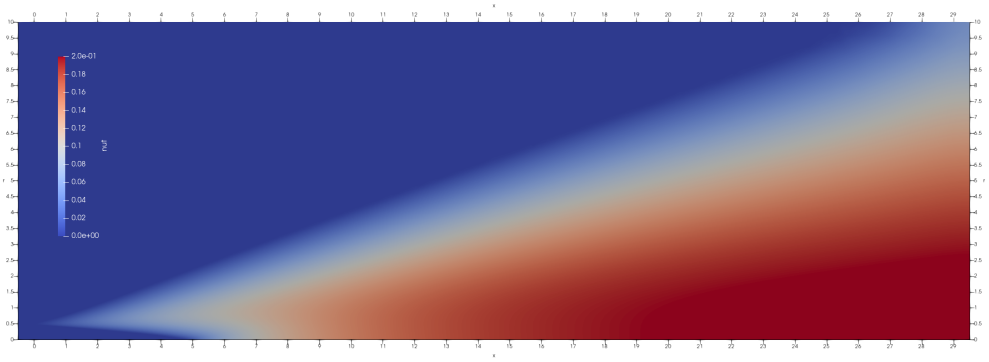

(a) `OpenFOAM` result,

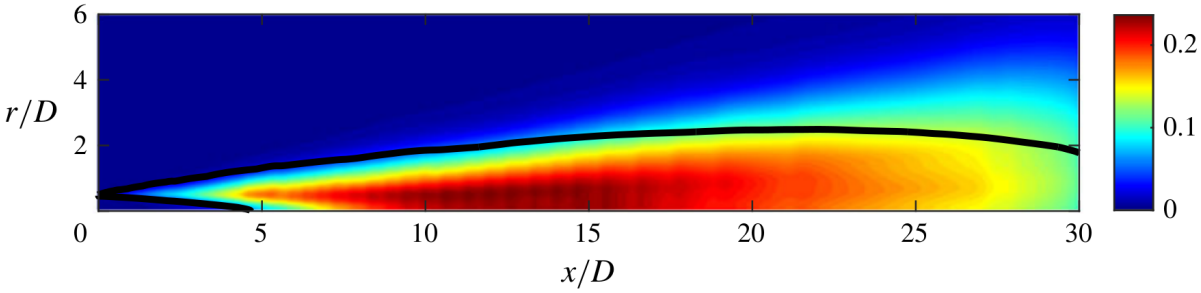

(b) Figure 2 of [101] displaying eddy viscosity, black line is 10% of turbulent kinetic energy.

Figure 4.17: Eddy viscosities.

Chapter 5

Final word

The rest is silence.

Shakespeare (Hamlet)

This thesis started with an overview of the Computational Fluid Dynamics field in general, and how resolvent analysis, the preferred method for the rest of this thesis, fits in the hierarchy of methods available to model turbulent flows. The differences with other Reynolds-Averaged Navier-Stokes methods were particularly emphasised, especially with regards to the canonical temporal and spatial stability approaches. It was established that resolvent analysis is a method that gives up on an exact description of turbulence and only describes instability behaviour around a baseflow. However in such a regime, the method does provide modes that can be compared to experimental results and reproduce a large part of the turbulent flow fluctuations energy for a very controlled computational cost, as established in [13]. Chapter 1 concluded with an overview of this thesis objectives and outline. The former will be reproduced here for convenience:

1. **Improve** resolvent accuracy and relevance at low frequencies,
2. **Investigate** the influence of swirl in a turbulent jet using resolvent analysis.

The following will briefly review results attained in this regard, and propositions relative to future work in the field will follow.

5.1 Summary of contributions

5.1.1 Second order resolvent

In chapter 2, a generalisation of the resolvent method to include correlations of velocity in the state vector was developed. Motivated by algebraic considerations and feeding on Reynolds Stress Modelling literature, the approach succeeded at integrating additional physics into the resolvent and to better reproduce some turbulent stresses present in real flows.

When compared with Spectral Proper Orthogonal Decomposition modes extracted from a DNS, this method was found to improve accuracy of the resolvent approach for a few select regimes. It notably improves the predictive performance of resolvent analysis in the main direction and close to the wall, and it also yields better approximation of fluctuation nonlinear terms for specific wavelengths. However, it turned out to be less precise overall than traditional 'first degree' resolvent enriched with turbulent eddy viscosity across the parameter space.

Therefore, the results of this thesis align with the current literature as outlined in [87–89, 129] in saying that the most straightforward way to improve resolvent performance is to include the same eddy viscosity in the resolvent operator than the one used in computing the baseflow equations. This amounts to viewing the fluctuations equations in a perturbative manner to the baseflow equations and strays a little from Navier-Stokes, but it has been established to work better in real conditions.

These results have led to a publication in the peer-reviewed journal *Comptes Rendus Mécanique*. They have also been presented at the European Mechanics Society (EUROMECH) colloquium 611, Jet Noise Modelling and Control, in September 2021 under the name "Reynolds-stress modelling for linear resolvent analysis".

5.1.2 Resolvent analysis on a swirling turbulent jet

The main contributions of this thesis can be found in chapter 3, where a swirling turbulent jet was explored using resolvent analysis. The introduction of swirl and a nozzle were both shown to have dramatic influence on results at low frequencies, bringing new behaviour to light.

Indeed, strong amplification of the low frequency regime was observed. This gain peak was further explained as interplay between Orr, lift-up and another amplification mechanism. Kelvin-Helmholtz was disqualified as the sole explanation for this regime through the use of the dot criterion, a new approach to discriminate shear instabilities motivated by local linear temporal stability analysis.

Quantifying alignment of fluctuations wavevector with principal shear directions, the dot criterion is a simple and straighforward way to quantify *a posteriori* the importance of a Kelvin-Helmholtz type instability for the most amplified resolvent response mode. Directly linked to a growth rate in an idealised setting, as present in [39, section B.2], it can also be derived from a double derivative of the Doppler-shifted frequency in time and in the radial direction. This quantity also appears in literature related to centrifugal instability such as [66, equation (5.6)] or [16, equation (3.8)].

Through the use of the dot criterion, it was possible to map the importance of Kelvin-Helmholtz type instabilities throughout the swirl-frequency domain and isolate drastically different behaviour between co-rotating and counter-rotating co-winding bi-spiral modes. Even if the pattern of average Kelvin-Helmholtz prevalence not correlated with the gains in any meaningful way, the dispersion of this criterion seems to be. This could mean that the most amplified modes throughout the parameter space are those that manage to leverage the Kelvin-Helmholtz and centrifugal phenomena simultaneously.

Because of the inclusion of a nozzle in the calculations, the computations performed in this thesis brought to light instabilities happening atop of the nozzle. Resolvent analysis outlined structures levering lift-up and baseflow entrainment to create energetically significant streaks all across the shear layer. These 'outer modes' are not expected to appear in temporal stability analysis which is unable to reproduce lift-up, or in geometries that do not allow for entrainment atop the nozzle.

These results were put together in a draft that will be submitted as soon as possible. They were also presented at the American Physics Society (APS) 75th Annual Meeting of the Division of Fluid Dynamics (DFD) on November 2022 under the name "Effect of swirl on linear formation of streaks in jets", as well as at the 15th European Community on Flow, Turbulence and Combustion (ERCOFTAC) SIG33 workshop called Progress in Flow Instability, Transition and Control under the name "Resolvent analysis of a round swirling turbulent jet".

5.1.3 `SPY` library

The swirling turbulent jet contribution was made possible due to extensive development of the `SPY` library now available to all on GitHub. This library makes extensive use of parallelism and unstructured meshes, features three-dimensional azimuthally decomposed perturbations and handles any arbitrary Dirichlet boundary conditions.

Through the use of finite-elements techniques, a Newton non-linear solver was implemented to obtain a smooth baseflow on which to perform instability analysis. Various eigenvalue solvers were leveraged to obtain both temporal stability routines and resolvent ones.

Numerical details may be found in chapter 4, including four validation cases to establish the relevance of `SPY` as a tool capable of handling swirling flows, linear stability problems, resolvent analysis and eddy viscosities. The tool has also demonstrated its stability at high Reynolds numbers.

5.2 Recommendation for future work

5.2.1 Second order resolvent

Regarding second order resolvent, it is probable that considering a case more favourable to a general method, such as one with more complex boundary conditions and/or geometry, would lead to a more favourable comparison with eddy viscosity models. In a channel flow case, eddy viscosity models such as that of Cess, the one used in chapter 2, are very well tailored to the case and reproduce fluctuations quite convincingly.

Another avenue to making the second order method more predictive is improving turbulent modelling. This remains an ongoing research subject, and the resolvent formalism is constrained by the fact that a nonlinear model for problematic terms such as the velocity-pressure gradient tensor is not that straightforward to implement.

Recent advances in computer science such as machine learning could be put to use here, yielding a linear model that is costly to train, but cheap to evaluate. Though such an approach would undoubtedly lose generality as any machine learning model would have to be fitted on data, and it will be difficult to give a precise validity range for such a model, it might still remain more general than the handful of eddy viscosity models available today.

5.2.2 Resolvent analysis on a swirling turbulent jet

On the subject of swirling turbulent flows, a number of important questions remain to be addressed. The counter-rotating co-winding double spiral that arises from resolvent analysis as the most amplified mode of the swirling turbulent flow considered for low frequencies has already been observed experimentally. This straightens the case for the relevance of resolvent analysis in addressing this complex problem, even though it may not be the best tool to point out underlying mechanisms driving the instability.

However, the outer mode feeding on entrainment outside the nozzle is not a widespread observation. Similar modes were presented at [18] obtained by another numerical study. Since this configuration is also of interest to many engineers, it seems desirable to perform experiments tailored specifically around this mode to try and single it out.

The prevalence of counter-rotating modes over co-rotating ones is observed but not explained. It remains unclear to the author at the time of writing why this is the case, or why gains experience such a sharp drop across zero frequency when moving from counter-winding to co-winding. Some authors have stopped at saying that more amplification for counter-winding modes is a feature of centrifugal modes, but it has never been clearly demonstrated to the author.

Open issues such as the influence of inertial waves warrant further study. This phenomenon seems familiar to part of the fluid mechanics community, especially researchers concerned with ocean waves where such inertial phenomena play an important role, but the situation of Kelvin waves in jets seems somewhat less mature. The geometry of a potential core is complex, which greatly complicates things when trying to evaluate the frequency of inertial waves theoretically. One approach to mitigate this would be to conduct experiments trying to capture the phenomenon of resonant collapse in a jet as [78] captured it in a cylinder.

Many applications relative to swirling flows have geometries more complex than the one presented in section 3.2.1. It could be fruitful to try more complex geometries inside the numerical domain, for instance including a convergent nozzle.

Bibliography

[1] Leandra I. Abreu et al. "Resolvent modelling of near-wall coherent structures in turbulent channel flow". en. In: *International Journal of Heat and Fluid Flow* 85 (Oct. 2020), p. 108662. ISSN: 0142-727X. DOI: 10.1016/j.ijheatfluidflow.2020.108662. URL: https://www.sciencedirect.com/science/article/pii/S0142727X20305580 (visited on 03/30/2021).

[2] M. A. Ahmed et al. "Resolvent analysis of stratification effects on wall-bounded shear flows". In: *Physical Review Fluids* 6.8 (Aug. 2021). Publisher: American Physical Society, p. 084804. DOI: 10.1103/PhysRevFluids.6.084804. URL: https://link.aps.org/doi/10.1103/PhysRevFluids.6.084804 (visited on 06/07/2022).

[3] Espen Åkervik et al. "Global two-dimensional stability measures of the flat plate boundary-layer flow". In: *European Journal of Mechanics - B/Fluids* 27.5 (Sept. 2008), pp. 501–513. ISSN: 0997-7546. DOI: 10.1016/j.euromechflu.2007.09.004. URL: https://www.sciencedirect.com/science/article/pii/S0997754607000908 (visited on 09/07/2023).

[4] Martin S. Alnæs et al. "Unified form language: A domain-specific language for weak formulations of partial differential equations". In: *ACM Transactions on Mathematical Software* 40.2 (Mar. 2014), 9:1–9:37. ISSN: 0098-3500. DOI: 10.1145/2566630. URL: https://doi.org/10.1145/2566630 (visited on 06/02/2023).

[5] Filipe R. Amaral et al. "Resolvent-based estimation of turbulent channel flow using wall measurements". en. In: *Journal of Fluid Mechanics* 927 (Nov. 2021). Publisher: Cambridge University Press. ISSN: 0022-1120, 1469-7645. DOI: 10.1017/jfm.2021.764. URL: https://www.cambridge.org/core/journals/journal-of-fluid-mechanics/article/resolventbased-estimation-of-turbulent-channel-flow-using-wall-measurements/8549636BFD23DEC5BE92C5D68BE9071C (visited on 06/03/2022).

[6] P. R. Amestoy et al. "A Fully Asynchronous Multifrontal Solver Using Distributed Dynamic Scheduling". In: *SIAM Journal on Matrix Analysis and Applications* 23.1 (2001), pp. 15–41.

[7] P. R. Amestoy et al. "Hybrid scheduling for the parallel solution of linear systems". In: *Parallel Computing* 32.2 (2006), pp. 136–156.

[8] Satish Balay et al. "Efficient Management of Parallelism in Object-Oriented Numerical Software Libraries". en. In: *Modern Software Tools for Scientific Computing*. Ed. by Erlend Arge, Are Magnus Bruaset, and Hans Petter Langtangen. Boston, MA: Birkhäuser, 1997, pp. 163–202. ISBN: 978-1-4612-1986-6. DOI: 10.1007/978-1-4612-1986-6_8. URL: https://doi.org/10.1007/978-1-4612-1986-6_8 (visited on 06/02/2023).

[9] Satish Balay et al. *PETSc Web page*. https://petsc.org/. 2023. URL: https://petsc.org/.

[10] Satish Balay et al. *PETSc/TAO Users Manual*. Tech. rep. ANL-21/39 - Revision 3.19. Argonne National Laboratory, 2023.

[11] Benedikt Barthel. "On the variational principles of linear and nonlinear resolvent analysis". en. PhD thesis. 2022.

[12] G. K. Batchelor and A. E. Gill. "Analysis of the stability of axisymmetric jets". en. In: *Journal of Fluid Mechanics* 14.4 (Dec. 1962). Publisher: Cambridge University Press, pp. 529–551. ISSN: 1469-7645, 0022-1120. DOI: 10.1017/S0022112062001421. URL: https://www.cambridge.org/core/journals/journal-of-fluid-mechanics/article/analysis-of-the-stability-of-axisymmetric-jets/AA68EA9CE4714C50B8B087ECA1E2E67B (visited on 08/17/2023).

[13] Samir Beneddine et al. "Conditions for validity of mean flow stability analysis". en. In: *Journal of Fluid Mechanics* 798 (July 2016). Publisher: Cambridge University Press, pp. 485–504. ISSN: 0022-1120, 1469-7645. DOI: 10.1017/jfm.2016.331. URL: https://www.cambridge.org/core/journals/journal-of-fluid-mechanics/article/conditions-for-validity-of-mean-flow-stability-analysis/2B42614C79F7EE9860AA56FB3DF1AB3 (visited on 08/17/2023).

[14] A. Bers. *Space-time evolution of plasma instabilities - absolute and convective*. INIS Reference Number: 15068895. Netherlands: North-Holland, 1983. ISBN: 978-0-444-86427-7.

[15] Paul Billant, Jean-Marc Chomaz, and Patrick Huerre. "Experimental study of vortex breakdown in swirling jets". en. In: *Journal of Fluid Mechanics* 376 (Dec. 1998). Publisher: Cambridge University Press, pp. 183–219. ISSN: 1469-7645, 0022-1120. DOI: 10.1017/S0022112098002870. URL: https://www.cambridge.org/core/journals/journal-of-fluid-mechanics/article/experimental-study-of-vortex-breakdown-in-swirling-jets/E78D382E75210292513FBEAD98551D75 (visited on 07/28/2023).

[16] Paul Billant and François Gallaire. "A unified criterion for the centrifugal instabilities of vortices and swirling jets". en. In: *Journal of Fluid Mechanics* 734 (Nov. 2013). Publisher: Cambridge University Press, pp. 5–35. ISSN: 0022-1120, 1469-7645. DOI: 10.1017/jfm.2013.460. URL: https://www.cambridge.org/core/journals/journal-of-fluid-mechanics/article/abs/unified-criterion-for-the-centrifugal-instabilities-of-vortices-and-swirling-jets/7DF5272AD53C8552615C36CE2D41C7B6 (visited on 08/02/2023).

[17] Paul Billant and François Gallaire. "Generalized Rayleigh criterion for non-axisymmetric centrifugal instabilities". en. In: *Journal of Fluid Mechanics* 542 (Nov. 2005). Publisher: Cambridge University Press, pp. 365–379. ISSN: 1469-7645, 0022-1120. DOI: 10.1017/S0022112005006464. URL: https://www.cambridge.org/core/journals/journal-of-fluid-mechanics/article/generalized-rayleigh-criterion-for-nonaxisymmetric-centrifugal-instabilities/EBD5A1C0273A1D8616C5F1FC75085DCF (visited on 08/17/2023).

[18] J Daniel Bodony, Alexandru Fikl, and Sandeep Murthy. "ADJOINT-BASED SENSITIVITY OF SHOCK-LADEN FLOWS". In: 15th ERCOFTAC. Progress in Flow Instability, Transition and Control, 2023.

[19] P. Brancher and J. M. Chomaz. "Absolute and Convective Secondary Instabilities in Spatially Periodic Shear Flows". In: *Physical Review Letters* 78.4 (Jan. 1997). Publisher: American Physical Society, pp. 658–661. DOI: 10.1103/PhysRevLett.78.658. URL: https://link.aps.org/doi/10.1103/PhysRevLett.78.658 (visited on 09/04/2023).

[20] Guillaume A. Brès et al. "Unstructured Large-Eddy Simulations of Supersonic Jets". en. In: *AIAA Journal* 55.4 (Apr. 2017), pp. 1164–1184. ISSN: 0001-1452, 1533-385X. DOI: 10.2514/1.J055084. URL: https://arc.aiaa.org/doi/10.2514/1.J055084 (visited on 06/28/2022).

[21] Alexander N. Brooks and Thomas J. R. Hughes. "Streamline upwind/Petrov-Galerkin formulations for convection dominated flows with particular emphasis on the incompressible Navier-Stokes equations". en. In: *Computer Methods in Applied Mechanics and Engineering* 32.1 (Sept. 1982), pp. 199–259. ISSN: 0045-7825. DOI: 10.1016/0045-7825(82)90071-8. URL: https://www.sciencedirect.com/science/article/pii/0045782582900718 (visited on 09/01/2022).

[22] Kathryn M. Butler and Brian F. Farrell. "Three-dimensional optimal perturbations in viscous shear flow". In: *Physics of Fluids A: Fluid Dynamics* 4.8 (Aug. 1992), pp. 1637–1650. ISSN: 0899-8213. DOI: 10.1063/1.858386. URL: https://doi.org/10.1063/1.858386 (visited on 09/08/2023).

[23] Hubert Chanson. *Hydraulics of Open Channel Flow*. en. Google-Books-ID: VCNmKQI6GiEC. Elsevier, May 2004. ISBN: 978-0-08-047297-3.

[24] Quentin Chevalier, Lesshafft Lutz, and André V. G. Cavalieri. "A second-order resolvent formulation for the analysis of turbulent flow structures". In: *Comptes Rendus. Mécanique* 351.G2 (2023), pp. 355–371. ISSN: 1873-7234. DOI: 10.5802/crmeca.193. URL: https://comptes-rendus.academie-sciences.fr/mecanique/articles/10.5802/crmeca.193/ (visited on 10/23/2023).

[25] Christopher Douglas. "Dynamics of swirling jets and flames". PhD thesis. 2021. URL: https://repository.gatech.edu/entities/publication/053f9ea7-43b3-439e-a19c-ce19635bb198 (visited on 05/15/2023).

[26] R. Courant, K. Friedrichs, and H. Lewy. "Über die partiellen Differenzengleichungen der mathematischen Physik". de. In: *Mathematische Annalen* 100.1 (Dec. 1928), pp. 32–74. ISSN: 1432-1807. DOI: 10.1007/BF01448839. URL: https://doi.org/10.1007/BF01448839 (visited on 08/15/2023).

[27] Lisandro D. Dalcin et al. "Parallel distributed computing using Python". en. In: *Advances in Water Resources*. New Computational Methods and Software Tools 34.9 (Sept. 2011), pp. 1124–1139. ISSN: 0309-1708. DOI: 10.1016/j.advwatres.2011.04.013. URL: https://www.sciencedirect.com/science/article/pii/S0309170811000777 (visited on 05/03/2022).

[28] Ivan Delbende, Jean-Marc Chomaz, and Patrick Huerre. "Absolute/convective instabilities in the Batchelor vortex: a numerical study of the linear impulse response". en. In: *Journal of Fluid Mechanics* 355 (Jan. 1998). Publisher: Cambridge University Press, pp. 229–254. ISSN: 1469-7645, 0022-1120. DOI: 10.1017/S0022112097007787. URL: https://www.cambridge.org/core/journals/journal-of-fluid-mechanics/article/absoluteconvective-instabilities-in-the-batchelor-vortex-a-numerical-study-of-the-linear-impulse-response/5C97626350FE1528D85E50CCD0392C99 (visited on 09/04/2023).

[29] Diogo Ferreira Sabino. "Aeroelastic instabilities of an airfoil in transitional flow regimes". PhD thesis. 2022.

[30] Christopher M. Douglas, Benjamin L. Emerson, and Timothy C. Lieuwen. "Nonlinear dynamics of fully developed swirling jets". en. In: *Journal of Fluid Mechanics* 924 (Oct. 2021). Publisher: Cambridge University Press, A14. ISSN: 0022-1120, 1469-7645. DOI: 10.1017/jfm.2021.615. URL: https://www.cambridge.org/core/journals/journal-of-fluid-mechanics/article/nonlinear-dynamics-of-fully-developed-swirling-jets/FE28A6F2254BAE7A97058457F4C9E3E5 (visited on 01/12/2023).

[31] P. G. Drazin and W. H. Reid. *Hydrodynamic Stability*. en. Google-Books-ID: GDDhso7XjngC. Cambridge University Press, 1982. ISBN: 978-0-521-52541-1.

[32] P. W. Duck. "The inviscid stability of swirling flows: Large wavenumber disturbances". en. In: *Zeitschrift für angewandte Mathematik und Physik ZAMP* 37.3 (May 1986), pp. 340–360. ISSN: 1420-9039. DOI: 10.1007/BF00946755. URL: https://doi.org/10.1007/BF00946755 (visited on 07/31/2023).

[33] P. A. Durbin. "A Reynolds stress model for near-wall turbulence". en. In: *Journal of Fluid Mechanics* 249.-1 (Apr. 1993), p. 465. ISSN: 0022-1120, 1469-7645. DOI: 10.1017/S0022112093001259. URL: http://www.journals.cambridge.org/abstract_S0022112093001259 (visited on 04/28/2021).

[34] T. Ellingsen and E. Palm. "Stability of linear flow". In: *The Physics of Fluids* 18.4 (Apr. 1975), pp. 487–488. ISSN: 0031-9171. DOI: 10.1063/1.861156. URL: https://doi.org/10.1063/1.861156 (visited on 08/16/2023).

[35] Kerry A. Emanuel. "A note on the stability of columnar vortices". en. In: *Journal of Fluid Mechanics* 145 (Aug. 1984). Publisher: Cambridge University Press, pp. 235–238. ISSN: 1469-7645, 0022-1120. DOI: 10.1017/S0022112084002895. URL: https://www.cambridge.org/core/journals/journal-of-fluid-mechanics/article/note-on-the-stability-of-columnar-vortices/7FC0E2325B21CD9D5C915E3E8CBBDA6C (visited on 08/04/2023).

[36] B. F. Farrell, D. F. Gayme, and P. J. Ioannou. "A statistical state dynamics approach to wall turbulence". In: *Philosophical Transactions of the Royal Society A: Mathematical, Physical and Engineering Sciences* 375.2089 (Mar. 2017). Publisher: Royal Society, p. 20160081. DOI: 10.1098/rsta.2016.0081. URL: https://royalsocietypublishing.org/doi/full/10.1098/rsta.2016.0081 (visited on 11/30/2022).

[37] Leopoldo P Franca and Thomas JR Hughes. "Two classes of mixed finite element methods". In: *Computer Methods in Applied Mechanics and Engineering* 69.1 (1988), pp. 89–129.

[38] Ivar Fredholm. "Sur une classe d'équations fonctionnelles". In: *Acta Mathematica* 27.none (Jan. 1903). Publisher: Institut Mittag-Leffler, pp. 365–390. ISSN: 0001-5962, 1871-2509. DOI: 10.1007/BF02421317. URL: https://projecteuclid.org/journals/acta-mathematica/volume-27/issue-none/Sur-une-classe-d%c3%a9quations-fonctionnelles/10.1007/BF02421317.full (visited on 08/11/2023).

[39] F. Gallaire and J.-M. Chomaz. "Instability mechanisms in swirling flows". en. In: *Physics of Fluids* 15.9 (Sept. 2003), pp. 2622–2639. ISSN: 1070-6631, 1089-7666. DOI: 10.1063/1.1589011. URL: http://aip.scitation.org/doi/10.1063/1.1589011 (visited on 03/17/2023).

[40] F. Gallaire, S. Rott, and J.-M. Chomaz. "Experimental study of a free and forced swirling jet". In: *Physics of Fluids* 16.8 (July 2004), pp. 2907–2917. ISSN: 1070-6631. DOI: 10.1063/1.1758171. URL: https://doi.org/10.1063/1.1758171 (visited on 07/31/2023).

[41] François Gallaire. "Instabilités dans les jets tournants et contrôle de l'éclatement tourbillonnaire". These de doctorat. Palaiseau, Ecole polytechnique, Jan. 2002. URL: https://www.theses.fr/2002EPXX0058 (visited on 09/04/2023).

[42] François Gallaire and Jean-Marc Chomaz. "Mode selection in swirling jet experiments: a linear stability analysis". en. In: *Journal of Fluid Mechanics* 494 (Nov. 2003). Publisher: Cambridge University Press, pp. 223–253. ISSN: 1469-7645, 0022-1120. DOI: 10.1017/S0022112003006104. URL: https://www.cambridge.org/core/journals/journal-of-fluid-mechanics/article/mode-selection-in-swirling-jet-experiments-a-linear-stability-analysis/0AD01253D869A87CE781CCEF66C9958A (visited on 12/08/2022).

[43] François Gallaire et al. "Spiral vortex breakdown as a global mode". en. In: *Journal of Fluid Mechanics* 549 (Feb. 2006). Publisher: Cambridge University Press, pp. 71–80. ISSN: 1469-7645, 0022-1120. DOI: 10.1017/S0022112005007834. URL: https://www.cambridge.org/core/journals/journal-of-fluid-mechanics/article/spiral-vortex-breakdown-as-a-global-mode/851820130A43F3FF792FBBDD4FACE6D0 (visited on 08/21/2023).

[44] X. Garnaud et al. "The preferred mode of incompressible jets: linear frequency response analysis". en. In: *Journal of Fluid Mechanics* 716 (Feb. 2013). Publisher: Cambridge University Press, pp. 189–202. ISSN: 0022-1120, 1469-7645. DOI: 10.1017/jfm.2012.540. URL: https://www.cambridge.org/core/journals/journal-of-fluid-mechanics/article/preferred-mode-of-incompressible-jets-linear-frequency-response-analysis/ADB24D98759281E33495286BC5810397 (visited on 12/08/2022).

[45] Xavier Garnaud. "Modes, transient dynamics and forced response of circular jets". en. PhD thesis. Ecole Polytechnique X, June 2012.

[46] Christophe Geuzaine and Jean-François Remacle. "Gmsh: A 3-D finite element mesh generator with built-in pre- and post-processing facilities". en. In: *International Journal for Numerical Methods in Engineering* 79.11 (2009). _eprint: https://onlinelibrary.wiley.com/doi/pdf/10.100 pp. 1309–1331. ISSN: 1097-0207. DOI: 10.1002/nme.2579. URL: https://onlinelibrary.wiley.com/doi/abs/10.1002/nme.2579 (visited on 06/05/2023).

[47] Flavio Giannetti and Paolo Luchini. "Structural sensitivity of the first instability of the cylinder wake". en. In: *Journal of Fluid Mechanics* 581 (June 2007). Publisher: Cambridge University Press, pp. 167–197. ISSN: 1469-7645, 0022-1120. DOI: 10.1017/S0022112007005654. URL: https://www.cambridge.org/core/journals/journal-of-fluid-mechanics/article/abs/structural-sensitivity-of-the-first-instability-of-the-cylinder-wake/020BE9D060A70BD7FE0301965AC81DB3 (visited on 09/15/2023).

[48] Greenspan. *The Theory of Rotating Fluids*. en. Google-Books-ID: 2R47AAAAIAAJ. CUP Archive, July 1968. ISBN: 978-0-521-05147-7.

[49] Vicente Hernandez, Jose E. Roman, and Vicente Vidal. "SLEPc: A scalable and flexible toolkit for the solution of eigenvalue problems". In: *ACM Transactions on Mathematical Software* 31.3 (Sept. 2005), pp. 351–362. ISSN: 0098-3500. DOI: 10.1145/1089014.1089019. URL: https://doi.org/10.1145/1089014.1089019 (visited on 09/18/2023).

[50] Dylan Christopher House. "Resolvent Analysis Techniques for Turbulent Flows: Application to an SUV Wake". en. PhD thesis. 2021.

[51] Louis N. Howard and A. S. Gupta. "On the hydrodynamic and hydromagnetic stability of swirling flows". en. In: *Journal of Fluid Mechanics* 14.3 (Nov. 1962). Publisher: Cambridge University Press, pp. 463–476. ISSN: 1469-7645, 0022-1120. DOI: 10.1017/S0022112062001366. URL: https://www.cambridge.org/core/journals/journal-of-fluid-mechanics/article/on-the-hydrodynamic-and-hydromagnetic-stability-of-swirling-flows/045686729B6B3B5D746510AA8042AA4E (visited on 08/17/2023).

[52] Patrick Huerre and Peter A Monkewitz. "Local and global instabilities in spatially developing flows". In: *Annual review of fluid mechanics* 22.1 (1990), pp. 473–537.

[53] Yongyun Hwang and Carlo Cossu. "Linear non-normal energy amplification of harmonic and stochastic forcing in the turbulent channel flow". en. In: *Journal of Fluid Mechanics* 664 (Dec. 2010). Publisher: Cambridge University Press, pp. 51–73. ISSN: 1469-7645, 0022-1120. DOI: 10.1017/S0022112010003629. URL: https://www.cambridge.org/core/journals/journal-of-fluid-mechanics/article/abs/linear-nonnormal-energy-amplification-of-harmonic-and-stochastic-forcing-in-the-turbulent-channel-flow/915E5F08F0462D1161D1B4E9745AE29D (visited on 01/12/2022).

[54] The MathWorks Inc. *MATLAB version: 9.13.0 (R2022b)*. Natick, Massachusetts, United States, 2022. URL: https://www.mathworks.com.

[55] Arne V. Johansson and Magnus Hallbäck. "Modelling of rapid pressure—strain in Reynolds-stress closures". en. In: *Journal of Fluid Mechanics* 269 (June 1994), pp. 143–168. ISSN: 0022-1120, 1469-7645. DOI: 10.1017/S0022112094001515. URL: https://www.cambridge.org/core/product/identifier/S0022112094001515/type/journal_article (visited on 02/18/2021).

[56] Volker John. *Finite Element Methods for Incompressible Flow Problems*. Vol. 51. Jan. 2016. ISBN: 978-3-319-45749-9. DOI: 10.1007/978-3-319-45750-5.

[57] W. P Jones and B. E Launder. "The prediction of laminarization with a two-equation model of turbulence". In: *International Journal of Heat and Mass Transfer* 15.2 (Feb. 1972), pp. 301–314. ISSN: 0017-9310. DOI: 10.1016/0017-9310(72)90076-2. URL: https://www.sciencedirect.com/science/article/pii/0017931072900762 (visited on 08/22/2023).

[58] U. Karban et al. "Self-similar mechanisms in wall turbulence studied using resolvent analysis". en. In: *Journal of Fluid Mechanics* 939 (May 2022). Publisher: Cambridge University Press, A36. ISSN: 0022-1120, 1469-7645. DOI: 10.1017/jfm.2022.225. URL: https://www.cambridge.org/core/journals/journal-of-fluid-mechanics/article/selfsimilar-mechanisms-in-wall-turbulence-studied-using-resolvent-analysis/193DC564F96967A452582918C6A42908 (visited on 08/16/2023).

[59] Mehdi R. Khorrami. "On the viscous modes of instability of a trailing line vortex". en. In: *Journal of Fluid Mechanics* 225 (Apr. 1991). Publisher: Cambridge University Press, pp. 197–212. ISSN: 1469-7645, 0022-1120. DOI: 10.1017/S0022112091002021. URL: https://www.cambridge.org/core/journals/journal-of-fluid-mechanics/article/on-the-viscous-modes-of-instability-of-a-trailing-line-vortex/1187C024D013542C16B467272A726788 (visited on 07/24/2023).

[60] Mehdi R. Khorrami. "Stability of a compressible axisymmetric swirling jet". In: *AIAA Journal* 33.4 (1995). Publisher: American Institute of Aeronautics and Astronautics _eprint: https://doi.org/10.2514/3.12627, pp. 650–658. ISSN: 0001-1452. DOI: 10.2514/3.12627. URL: https://doi.org/10.2514/3.12627 (visited on 07/24/2023).

[61] J Knoell. "A Nonlinear Stress-Strain Model for Wall-Bounded Turbulent Flows". en. In: (1999), p. 10.

[62] Sungho Ko. "A near-wall reynolds stress model for backward-facing step flows". en. In: *KSME International Journal* 13.2 (Feb. 1999), pp. 200–210. ISSN: 1226-4865. DOI: 10.1007/BF02943672. URL: http://link.springer.com/10.1007/BF02943672 (visited on 05/07/2021).

[63] Kolmogorov, N. A. "Definition of center of dispersion and measure of accuracy from a finite number of observations (in Russian)". In: *Izv. Akad. Nauk S. S. S. R. Ser. Mat.* 6 (1942), pp. 3–32. URL: https://cir.nii.ac.jp/crid/1571417125440162048 (visited on 08/09/2023).

[64] B E Launder and B I Sharma. "APPLICATION OF THE ENERGY-DISSIPATION MODEL OF TURBULENCE TO THE CALCULATION OF FLOW NEAR A SPINNING DISC". en. In: 1.2 (1974).

[65] B. E. Launder, G. J. Reece, and W. Rodi. "Progress in the development of a Reynolds-stress turbulence closure". en. In: *Journal of Fluid Mechanics* 68.3 (Apr. 1975). Publisher: Cambridge University Press, pp. 537–566. ISSN: 1469-7645, 0022-1120. DOI: 10.1017/S0022112075001814. URL: https://www.cambridge.org/core/journals/journal-of-fluid-mechanics/article/abs/progress-in-the-development-of-a-reynoldsstress-turbulence-closure/796DDAC14EF54A84A36100565D3420D5 (visited on 02/16/2021).

[66] S. Leibovich and K. Stewartson. "A sufficient condition for the instability of columnar vortices". en. In: *Journal of Fluid Mechanics* 126 (Jan. 1983). Publisher: Cambridge University Press, pp. 335–356. ISSN: 1469-7645, 0022-1120. DOI: 10.1017/S0022112083000191. URL: https://www.cambridge.org/core/journals/journal-of-fluid-mechanics/article/sufficient-condition-for-the-instability-of-columnar-vortices/1D9BBD70FF45F18D5D5561C9153C2528 (visited on 05/11/2023).

[67] Martin Lessen and Frederick Paillet. "The stability of a trailing line vortex. Part 2. Viscous theory". en. In: *Journal of Fluid Mechanics* 65.4 (Oct. 1974). Publisher: Cambridge University Press, pp. 769–779. ISSN: 1469-7645, 0022-1120. DOI: 10.1017/S0022112074001649. URL: https://www.cambridge.org/core/journals/journal-of-fluid-mechanics/article/stability-of-a-trailing-line-vortex-part-2-viscous-theory/3A330105F65E90DE510E6E96000C9712 (visited on 07/24/2023).

[68] Martin Lessen, Pawan Jit Singh, and Frederick Paillet. "The stability of a trailing line vortex. Part 1. Inviscid theory". en. In: *Journal of Fluid Mechanics* 63.4 (May 1974). Publisher: Cambridge University Press, pp. 753–763. ISSN: 1469-7645, 0022-1120. DOI: 10.1017/S0022112074002175. URL: https://www.cambridge.org/core/journals/journal-of-fluid-mechanics/article/stability-of-a-trailing-line-vortex-part-1-inviscid-theory/5247D9EC899DB3A37379D626C6FD6B87 (visited on 07/24/2023).

[69] Hanzhuang Liang and T. Maxworthy. "An experimental investigation of swirling jets". en. In: *Journal of Fluid Mechanics* 525 (Feb. 2005). Publisher: Cambridge University Press, pp. 115–159. ISSN: 1469-7645, 0022-1120. DOI: 10.1017/S0022112004002629. URL: https://www.cambridge.org/core/journals/journal-of-fluid-mechanics/article/an-experimental-investigation-of-swirling-jets/3852557C98F04A0D5925F6F1738213BA (visited on 08/01/2023).

[70] T. Loiseleux, J. M. Chomaz, and P. Huerre. "The effect of swirl on jets and wakes: Linear instability of the Rankine vortex with axial flow". In: *Physics of Fluids* 10.5 (May 1998). Publisher: American Institute of Physics, pp. 1120–1134. ISSN: 1070-6631. DOI: 10.1063/1.869637. URL: https://aip.scitation.org/doi/abs/10.1063/1.869637 (visited on 03/14/2023).

[71] Thomas Loiseleux, Ivan Delbende, and Patrick Huerre. "Absolute and convective instabilities of a swirling jet/wake shear layer". In: *Physics of Fluids* 12.2 (Feb. 2000). Publisher: American Institute of Physics, pp. 375–380. ISSN: 1070-6631. DOI: 10.1063/1.870315. URL: https://aip.scitation.org/doi/abs/10.1063/1.870315 (visited on 04/04/2023).

[72] Ganyu Lu and Sanjiva K. Lele. "Inviscid instability of compressible swirling mixing layers". In: *Physics of Fluids* 11.2 (Feb. 1999), pp. 450–461. ISSN: 1070-6631. DOI: 10.1063/1.869861. URL: https://doi.org/10.1063/1.869861 (visited on 05/11/2023).

[73] J. B. Marston, G. P. Chini, and S. M. Tobias. "Generalized Quasilinear Approximation: Application to Zonal Jets". In: *Physical Review Letters* 116.21 (May 2016). Publisher: American Physical Society, p. 214501. DOI: 10.1103/PhysRevLett.116.214501. URL: https://link.aps.org/doi/10.1103/PhysRevLett.116.214501 (visited on 11/29/2022).

[74] J. E. Martin and E. Meiburg. "Nonlinear axisymmetric and three-dimensional vorticity dynamics in a swirling jet model". In: *Physics of Fluids* 8.7 (July 1996), pp. 1917–1928. ISSN: 1070-6631. DOI: 10.1063/1.868971. URL: https://doi.org/10.1063/1.868971 (visited on 08/21/2023).

[75] J. E. Martin and E. Meiburg. "On the stability of the swirling jet shear layer". In: *Physics of Fluids* 6.1 (Jan. 1994), pp. 424–426. ISSN: 1070-6631. DOI: 10.1063/1.868041. URL: https://doi.org/10.1063/1.868041 (visited on 08/21/2023).

[76] Eduardo Martini et al. "Accurate Frequency Domain Identification of ODEs with Arbitrary Signals". en. In: *arXiv:1907.04787 [physics]* (Apr. 2020). arXiv: 1907.04787. URL: http://arxiv.org/abs/1907.04787 (visited on 11/06/2020).

[77] Eduardo Martini et al. "Resolvent-based optimal estimation of transitional and turbulent flows". In: *Journal of Fluid Mechanics* 900 (2020), A2. DOI: 10.1017/jfm.2020.435.

[78] A. D. McEwan. "Inertial oscillations in a rotating fluid cylinder". en. In: *Journal of Fluid Mechanics* 40.3 (Feb. 1970). Publisher: Cambridge University Press, pp. 603–640. ISSN: 1469-7645, 0022-1120. DOI: 10.1017/S0022112070000344. URL: https://www.cambridge.org/core/journals/journal-of-fluid-mechanics/article/abs/inertial-oscillations-in-a-rotating-fluid-cylinder/256A3FA760DBD0526B01F01E690E6535 (visited on 09/08/2023).

[79] B. J. McKeon and A. S. Sharma. "A critical-layer framework for turbulent pipe flow". en. In: *Journal of Fluid Mechanics* 658 (Sept. 2010). Publisher: Cambridge University Press, pp. 336–382. ISSN: 1469-7645, 0022-1120. DOI: 10.1017/S002211201000176X. URL: https://www.cambridge.org/core/journals/journal-of-fluid-mechanics/article/criticallayer-framework-for-turbulent-pipe-flow/9F24E435E35F63E8D2A8BC20E8EE2C9 (visited on 08/23/2023).

[80] Philippe Meliga, François Gallaire, and Jean-Marc Chomaz. "A weakly nonlinear mechanism for mode selection in swirling jets". en. In: *Journal of Fluid Mechanics* 699 (May 2012). Publisher: Cambridge University Press, pp. 216–262. ISSN: 1469-7645, 0022-1120. DOI: 10.1017/jfm.2012.93. URL: https://www.cambridge.org/core/journals/journal-of-fluid-mechanics/article/weakly-nonlinear-mechanism-for-mode-selection-in-swirling-jets/9C383EFFD22327805E07B6C7355F4C3E (visited on 10/06/2021).

[81] F. R. Menter, A. V. Garbaruk, and Y. Egorov. "Explicit algebraic reynolds stress models for anisotropic wall-bounded flows". en. In: *Progress in Flight Physics*. Vol. 3. EDP Sciences, 2012, pp. 89–104. ISBN: 978-2-7598-0674-4 978-2-7598-0717-8. DOI: 10.1051/eucass/201203089. URL: https://www.eucass-proceedings.eu/articles/eucass/abs/2012/02/eucass3p089/eucass3p089.html (visited on 02/18/2021).

[82] R. Moarref et al. "A low-order decomposition of turbulent channel flow via resolvent analysis and convex optimization". en. In: *Physics of Fluids* 26.5 (May 2014), p. 051701. ISSN: 1070-6631, 1089-7666. DOI: 10.1063/1.4876195. URL: http://aip.scitation.org/doi/10.1063/1.4876195 (visited on 05/10/2021).

[83] B. Mohammadi and O. Pironneau. *Analysis of the K-epsilon turbulence model*. INIS Reference Number: 26037421. France: Editions MASSON, 1993. ISBN: 978-2-225-84391-4.

[84] Pradeep Moise and Joseph Mathew. "Hysteresis and turbulent vortex breakdown in transitional swirling jets". en. In: *Journal of Fluid Mechanics* 915 (May 2021). Publisher: Cambridge University Press, A94. ISSN: 0022-1120, 1469-7645. DOI: 10.1017/jfm.2021.118. URL: https://www.cambridge.org/core/journals/journal-of-fluid-mechanics/article/hysteresis-and-turbulent-vortex-breakdown-in-transitional-swirling-jets/5D312B03D1820CCE9A9F75C916A0D666 (visited on 07/31/2023).

[85] Antonios Monokrousos. "Optimisation and control of boundary layer flows". en. PhD thesis. 2009.

[86] D. Montagnani and F. Auteri. "Non-modal analysis of coaxial jets". en. In: *Journal of Fluid Mechanics* 872 (Aug. 2019). Publisher: Cambridge University Press, pp. 665–696. ISSN: 0022-1120, 1469-7645. DOI: 10.1017/jfm.2019.356. URL: https://www.cambridge.org/core/journals/journal-of-fluid-mechanics/article/nonmodal-analysis-of-coaxial-jets/C633433D304F1E8E64EFE849874B8349 (visited on 11/14/2022).

[87] P. Morra et al. "Resolvent Analysis: With or Without Eddy Viscosity?" en. In: *ERCOFTAC Bulletin* 118 (2019), p. 20. URL: https://hal.science/hal-02348082 (visited on 06/05/2023).

[88] Pierluigi Morra et al. "On the relevance of Reynolds stresses in resolvent analyses of turbulent wall-bounded flows". en. In: *Journal of Fluid Mechanics* 867 (May 2019). arXiv: 1901.04356, pp. 969–984. ISSN: 0022-1120, 1469-7645. DOI: 10.1017/jfm.2019.196. URL: http://arxiv.org/abs/1901.04356 (visited on 05/04/2021).

[89] Pierluigi Morra et al. "The colour of forcing statistics in resolvent analyses of turbulent channel flows". en. In: *Journal of Fluid Mechanics* 907 (Jan. 2021). Publisher: Cambridge University Press. ISSN: 0022-1120, 1469-7645. DOI: 10.1017/jfm.2020.802. URL: https://www.cambridge.org/core/journals/journal-of-fluid-mechanics/article/colour-of-forcing-statistics-in-resolvent-analyses-of-turbulent-channel-flows/CBB737704F659C39772EB1637750E687 (visited on 12/02/2020).

[90] M. Mory. "Inertial Waves". en. In: *Rotating Fluids in Geophysical and Industrial Applications*. Ed. by E. J. Hopfinger. International Centre for Mechanical Sciences. Vienna: Springer, 1992, pp. 175–184. ISBN: 978-3-7091-2602-8. DOI: 10.1007/978-3-7091-2602-8_8. URL: https://doi.org/10.1007/978-3-7091-2602-8_8 (visited on 09/08/2023).

[91] Petrônio A. S. Nogueira et al. "Large-scale streaky structures in turbulent jets". en. In: *Journal of Fluid Mechanics* 873 (Aug. 2019). Publisher: Cambridge University Press, pp. 211–237. ISSN: 0022-1120, 1469-7645. DOI: 10.1017/jfm.2019.365. URL: https://www.cambridge.org/core/journals/journal-of-fluid-mechanics/article/abs/largescale-streaky-structures-in-turbulent-jets/B37B6DA58363B19F2DB49B9026D6A40F (visited on 04/29/2022).

[92] K. Oberleithner, C. O. Paschereit, and I. Wygnanski. "On the impact of swirl on the growth of coherent structures". en. In: *Journal of Fluid Mechanics* 741 (Feb. 2014). Publisher: Cambridge University Press, pp. 156–199. ISSN: 0022-1120, 1469-7645. DOI: 10.1017/jfm.2013.669. URL: https://www.cambridge.org/core/journals/journal-of-fluid-mechanics/article/on-the-impact-of-swirl-on-the-growth-of-coherent-structures/3A7F8E35D4213EE83CBD2E07788F1AF7 (visited on 06/26/2023).

[93] L. Onsager. "Statistical hydrodynamics". en. In: *Convegno Internazionale di Meccanica Statistica* (1949).

[94] *OpenFOAM | Free CFD Software | The OpenFOAM Foundation*. URL: https://openfoam.org/ (visited on 04/29/2022).

[95] J. Panda and D. K. McLaughlin. "Experiments on the instabilities of a swirling jet". en. In: *Physics of Fluids* 6.1 (Jan. 1994), pp. 263–276. ISSN: 1070-6631, 1089-7666. DOI: 10.1063/1.868074. URL: https://pubs.aip.org/pof/article/6/1/263/259492/Experiments-on-the-instabilities-of-a-swirling-jet (visited on 08/03/2023).

[96] S. Pasche, F. Gallaire, and F. Avellan. "Predictive control of spiral vortex breakdown". en. In: *Journal of Fluid Mechanics* 842 (May 2018). Publisher: Cambridge University Press, pp. 58–86. ISSN: 0022-1120, 1469-7645. DOI: 10.1017/jfm.2018.124. URL: https://www.cambridge.org/core/journals/journal-of-fluid-mechanics/article/abs/predictive-control-of-spiral-vortex-breakdown/17A9860BD57A3B884BE0330EA2A9E86E (visited on 09/13/2023).

[97] Simon Pasche, F. Avellan, and F. Gallaire. "Onset of chaos in helical vortex breakdown at low Reynolds number". In: *Physical Review Fluids* 3.6 (2018). Publisher: APS, p. 064701.

[98] Suhas V. Patankar. "A CALCULATION PROCEDURE FOR TWO-DIMENSIONAL ELLIPTIC SITUATIONS". en. In: *Numerical Heat Transfer* 4.4 (Oct. 1981), pp. 409–425. ISSN: 0149-5720. DOI: 10.1080/01495728108961801. URL: http://www.tandfonline.com/doi/abs/10.1080/01495728108961801 (visited on 07/26/2022).

[99] Virendra C. Patel, Wolfgang Rodi, and Georg Scheuerer. "Turbulence models for near-wall and low Reynolds number flows - A review". In: *AIAA Journal* 23.9 (1985). Publisher: American Institute of Aeronautics and Astronautics _eprint: https://doi.org/10.2514/3.9086, pp. 1308–1319. ISSN: 0001-1452. DOI: 10.2514/3.9086. URL: https://doi.org/10.2514/3.9086 (visited on 07/27/2021).

[100] Ethan Pickering. "Resolvent modeling of turbulent jets". en. PhD thesis. 2021.

[101] Ethan Pickering et al. "Lift-up, Kelvin-Helmholtz and Orr mechanisms in turbulent jets". In: *Journal of Fluid Mechanics* 896 (Aug. 2020). arXiv: 1909.09737, A2. ISSN: 0022-1120, 1469-7645. DOI: 10.1017/jfm.2020.301. URL: http://arxiv.org/abs/1909.09737 (visited on 10/23/2020).

[102] Ethan M. Pickering et al. "Eddy viscosity for resolvent-based jet noise models". en. In: *25th AIAA/CEAS Aeroacoustics Conference*. Delft, The Netherlands: American Institute of Aeronautics and Astronautics, May 2019. ISBN: 978-1-62410-588-3. DOI: 10.2514/6.2019-2454. URL: https://arc.aiaa.org/doi/10.2514/6.2019-2454 (visited on 11/09/2022).

[103] Stephen B. Pope. *Turbulent Flows*. en. Cambridge University Press, Aug. 2000. ISBN: 978-0-511-84053-1. DOI: 10.1017/CBO9780511840531. URL: https://www.cambridge.org/highereducation/books/turbulent-flows/C58EFF59AF9B81AE6CFAC9ED16486B3A (visited on 05/23/2022).

[104] Gregory Pujals et al. "A note on optimal transient growth in turbulent channel flows". In: *Physics of Fluids* 21.1 (Jan. 2009). Publisher: American Institute of Physics, p. 015109. ISSN: 1070-6631. DOI: 10.1063/1.3068760. URL: https://aip.scitation.org/doi/full/10.1063/1.3068760 (visited on 03/20/2023).

[105] Ubaid Ali Qadri, Dhiren Mistry, and Matthew P. Juniper. "Structural sensitivity of spiral vortex breakdown". en. In: *Journal of Fluid Mechanics* 720 (Apr. 2013), pp. 558–581. ISSN: 0022-1120, 1469-7645. DOI: 10.1017/jfm.2013.34. URL: https://www.cambridge.org/core/product/identifier/S0022112013000347/type/journal_article (visited on 09/13/2023).

[106] Matthias Rauter et al. "Granular porous landslide tsunami modelling – the 2014 Lake Askja flank collapse". en. In: 13.1 (Feb. 2022). Number: 1 Publisher: Nature Publishing Group, p. 678. ISSN: 2041-1723. DOI: 10.1038/s41467-022-28296-7. URL: https://www.nature.com/articles/s41467-022-28296-7 (visited on 09/05/2023).

[107] Rayleigh. "On the Dynamics of Revolving Fluids on JSTOR". en. In: *Proceedings of the Royal Society of London*. Vol. 93. Containing Papers of a Mathematical and Physical Character A. Royal Society, Mar. 1917, pp. 148–154. URL: https://www.jstor.org/stable/93794 (visited on 08/17/2023).

[108] Lord Rayleigh. "VIII. On the question of the stability of the flow of fluids". In: *The London, Edinburgh, and Dublin Philosophical Magazine and Journal of Science* 34.206 (July 1892). Publisher: Taylor & Francis _eprint: https://doi.org/10.1080/14786449208620167, pp. 59–70. ISSN: 1941-5982. DOI: 10.1080/14786449208620167. URL: https://doi.org/10.1080/14786449208620167 (visited on 08/17/2023).

[109] S. C. Reddy and J. A. C. Weideman. "The Accuracy of the Chebyshev Differencing Method for Analytic Functions". In: *SIAM Journal on Numerical Analysis* 42.5 (2005). Publisher: Society for Industrial and Applied Mathematics, pp. 2176–2187. ISSN: 0036-1429. URL: https://www.jstor.org/stable/4101382 (visited on 02/08/2023).

[110] Osborne Reynolds. "IV. On the dynamical theory of incompressible viscous fluids and the determination of the criterion". In: *Philosophical Transactions of the Royal Society of London. (A.)* 186 (1895). Publisher: Royal Society, pp. 123–164. DOI: 10.1098/rsta.1895.0004. URL: https://royalsocietypublishing.org/doi/10.1098/rsta.1895.0004 (visited on 08/22/2023).

[111] W. C. Reynolds and W. G. Tiederman. "Stability of turbulent channel flow, with application to Malkus's theory". en. In: *Journal of Fluid Mechanics* 27.2 (Feb. 1967), pp. 253–272. ISSN: 0022-1120, 1469-7645. DOI: 10.1017/S0022112067000308. URL: https://www.cambridge.org/core/product/identifier/S0022112067000308/type/journal_article (visited on 11/29/2022).

[112] J E Roman et al. "SLEPc Users Manual". en. In: ().

[113] Kevin Rosenberg. "Resolvent-based modeling of flows in a channel". en. PhD thesis. 2018.

[114] Kevin Rosenberg and Beverley J. McKeon. "Computing exact coherent states in channels starting from the laminar profile: A resolvent-based approach". In: *Physical Review E* 100.2 (Aug. 2019). Publisher: American Physical Society, p. 021101. DOI: 10.1103/PhysRevE.100.021101. URL: https://link.aps.org/doi/10.1103/PhysRevE.100.021101 (visited on 06/03/2022).

[115] M. R. Ruith et al. "Three-dimensional vortex breakdown in swirling jets and wakes: direct numerical simulation". en. In: *Journal of Fluid Mechanics* 486 (June 2003). Publisher: Cambridge University Press, pp. 331–378. ISSN: 1469-7645, 0022-1120. DOI: 10.1017/S0022112003004749. URL: https://www.cambridge.org/core/journals/journal-of-fluid-mechanics/article/threedimensional-vortex-breakdown-in-swirling-jets-and-wakes-direct-numerical-simulation/6AB7F50FBF65A5DED546C613E3B29895 (visited on 08/21/2023).

[116] P. G. Saffman. *Vortex Dynamics*. en. Google-Books-ID: FyxqMmCPu4AC. Cambridge University Press, Feb. 1995. ISBN: 978-0-521-47739-0.

[117] R. D. Sandberg, N. D. Sandham, and V. Suponitsky. "DNS of compressible pipe flow exiting into a coflow". en. In: *International Journal of Heat and Fluid Flow*. 7th Symposium on Turbulence & Shear Flow Phenomena (TSFP7) 35 (June 2012), pp. 33–44. ISSN: 0142-727X. DOI: 10.1016/j.ijheatfluidflow.2012.01.006. URL: https://www.sciencedirect.com/science/article/pii/S0142727X12000148 (visited on 08/05/2022).

[118] Peter J. Schmid. "Nonmodal Stability Theory". en. In: *Annual Review of Fluid Mechanics* 39.1 (Jan. 2007), pp. 129–162. ISSN: 0066-4189, 1545-4479. DOI: 10.1146/annurev.fluid.38.050304.092139. URL: https://www.annualreviews.org/doi/10.1146/annurev.fluid.38.050304.092139 (visited on 12/07/2022).

[119] Peter J. Schmid and Dan S. Henningson. "Transition to Turbulence". en. In: *Stability and Transition in Shear Flows*. Ed. by Peter J. Schmid and Dan S. Henningson. Applied Mathematical Sciences. New York, NY: Springer, 2001, pp. 401–475. ISBN: 978-1-4613-0185-1. DOI: 10.1007/978-1-4613-0185-1_9. URL: https://doi.org/10.1007/978-1-4613-0185-1_9 (visited on 08/28/2023).

[120] Oliver T. Schmidt and Tim Colonius. "Guide to Spectral Proper Orthogonal Decomposition". In: *AIAA Journal* 58.3 (Mar. 2020). Publisher: American Institute of Aeronautics and Astronautics, pp. 1023–1033. ISSN: 0001-1452. DOI: 10.2514/1.J058809. URL: https://arc.aiaa.org/doi/10.2514/1.J058809 (visited on 10/12/2021).

[121] Oliver T. Schmidt et al. "Spectral analysis of jet turbulence". en. In: *Journal of Fluid Mechanics* 855 (Nov. 2018), pp. 953–982. ISSN: 0022-1120, 1469-7645. DOI: 10.1017/jfm.2018.675. URL: https://www.cambridge.org/core/product/identifier/S0022112018006754/type/journal_article (visited on 08/03/2021).

[122] Matthew W. Scroggs et al. "Basix: a runtime finite element basis evaluation library". en. In: *Journal of Open Source Software* 7.73 (May 2022), p. 3982. ISSN: 2475-9066. DOI: 10.21105/joss.03982. URL: https://joss.theoj.org/papers/10.21105/joss.03982 (visited on 06/02/2023).

[123] Matthew W. Scroggs et al. "Construction of Arbitrary Order Finite Element Degree-of-Freedom Maps on Polygonal and Polyhedral Cell Meshes". In: *ACM Transactions on Mathematical Software* 48.2 (May 2022), 18:1–18:23. ISSN: 0098-3500. DOI: 10.1145/3524456. URL: https://dl.acm.org/doi/10.1145/3524456 (visited on 06/02/2023).

[124] Onofrio Semeraro et al. "Modeling of coherent structures in a turbulent jet as global linear instability wavepackets: Theory and experiment". en. In: *International Journal of Heat and Fluid Flow* 62 (Dec. 2016), pp. 24–32. ISSN: 0142-727X. DOI: 10.1016/j.ijheatfluidflow.2016.10.010. URL: https://www.sciencedirect.com/science/article/pii/S0142727X16307056 (visited on 06/15/2023).

[125] J. Smagorinsky. "GENERAL CIRCULATION EXPERIMENTS WITH THE PRIMITIVE EQUATIONS: I. THE BASIC EXPERIMENT". EN. In: *Monthly Weather Review* 91.3 (Mar. 1963). Publisher: American Meteorological Society Section: Monthly Weather Review, pp. 99–164. ISSN: 1520-0493, 0027-0644. DOI: 10.1175/1520-0493(1963)091<0099:GCEWTP>2.3.CO;2. URL: https://journals.ametsoc.org/view/journals/mwre/91/3/1520-0493_1963_091_0099_gcewtp_2_3_co_2.xml (visited on 08/09/2023).

[126] P. Spalart and S. Allmaras. "A one-equation turbulence model for aerodynamic flows". In: *30th Aerospace Sciences Meeting and Exhibit*. _eprint: https://arc.aiaa.org/doi/pdf/10.2514/6.1992-439. American Institute of Aeronautics and Astronautics, 1992. DOI: 10.2514/6.1992-439. URL: https://arc.aiaa.org/doi/abs/10.2514/6.1992-439 (visited on 01/25/2022).

[127] Herbert Brian Squire and Richard Vynne Southwell. "On the stability for three-dimensional disturbances of viscous fluid flow between parallel walls". In: *Proceedings of the Royal Society of London. Series A, Containing Papers of a Mathematical and Physical Character* 142.847 (Jan. 1997). Publisher: Royal Society, pp. 621–628. DOI: 10.1098/rspa.1933.0193. URL: https://royalsocietypublishing.org/doi/abs/10.1098/rspa.1933.0193 (visited on 08/31/2023).

[128] Sean Symon, Simon J. Illingworth, and Ivan Marusic. "Energy transfer in turbulent channel flows and implications for resolvent modelling". en. In: *Journal of Fluid Mechanics* 911 (Mar. 2021). Publisher: Cambridge University Press. ISSN: 0022-1120, 1469-7645. DOI: 10.1017/jfm.2020.929. URL: https://www.cambridge.org/core/journals/journal-of-fluid-mechanics/article/energy-transfer-in-turbulent-channel-flows-and-implications-for-resolvent-modelling/396400E03514B3646E50122394FE7BE8 (visited on 06/07/2022).

[129] Sean Symon et al. *On the use of eddy viscosity in resolvent analysis of turbulent channel flow*. Tech. rep. arXiv:2205.11216. arXiv:2205.11216 [physics] type: article. arXiv, May 2022. DOI: 10.48550/arXiv.2205.11216. URL: http://arxiv.org/abs/2205.11216 (visited on 06/07/2022).

[130] Sean Pearson Symon. "Reconstruction and Estimation of Flows Using Resolvent Analysis and Data-Assimilation". en. PhD thesis. 2018.

[131] L J. Synge. "The stability of heterogeneous liquids". In: *Trans. R. Soc. Canada* 27 (1938), p. 1. URL: https://cir.nii.ac.jp/crid/1570572700002381952 (visited on 08/25/2023).

[132] Kunihiko Taira et al. "Modal Analysis of Fluid Flows: An Overview". In: *AIAA Journal* 55.12 (Dec. 2017). Publisher: American Institute of Aeronautics and Astronautics, pp. 4013–4041. ISSN: 0001-1452. DOI: 10.2514/1.J056060. URL: https://arc.aiaa.org/doi/10.2514/1.J056060 (visited on 08/11/2023).

[133] Nikitas Thomareis and George Papadakis. "Resolvent analysis of separated and attached flows around an airfoil at transitional Reynolds number". en. PhD thesis. July 2018. URL: https://link.aps.org/doi/10.1103/PhysRevFluids.3.073901 (visited on 08/11/2023).

[134] Aaron Towne, Guillaume A. Brès, and Sanjiva K. Lele. "A statistical jet-noise model based on the resolvent framework". en. In: *23rd AIAA/CEAS Aeroacoustics Conference*. Denver, Colorado: American Institute of Aeronautics and Astronautics, June 2017. ISBN: 978-1-62410-504-3. DOI: 10.2514/6.2017-3706. URL: https://arc.aiaa.org/doi/10.2514/6.2017-3706 (visited on 08/03/2021).

[135] Aaron Towne, Oliver T. Schmidt, and Tim Colonius. "Spectral proper orthogonal decomposition and its relationship to dynamic mode decomposition and resolvent analysis". en. In: *Journal of Fluid Mechanics* 847 (July 2018), pp. 821–867. ISSN: 0022-1120, 1469-7645. DOI: 10.1017/jfm.2018.283. URL: https://www.cambridge.org/core/product/identifier/S0022112018002835/type/journal_article (visited on 08/03/2021).

[136] Aaron Towne et al. "Stochastic and nonlinear forcing of wavepackets in a Mach 0.9 jet". en. In: *21st AIAA/CEAS Aeroacoustics Conference*. Dallas, TX: American Institute of Aeronautics and Astronautics, June 2015. ISBN: 978-1-62410-367-4. DOI: 10.2514/6.2015-2217. URL: https://arc.aiaa.org/doi/10.2514/6.2015-2217 (visited on 08/03/2021).

[137] J. P. Van Doormaal and G. D. Raithby. "ENHANCEMENTS OF THE SIMPLE METHOD FOR PREDICTING INCOMPRESSIBLE FLUID FLOWS". en. In: *Numerical Heat Transfer* 7.2 (Apr. 1984), pp. 147–163. ISSN: 0149-5720. DOI: 10.1080/01495728408961817. URL: http://www.tandfonline.com/doi/abs/10.1080/01495728408961817 (visited on 07/26/2022).

[138] B. Zang et al. "An assessment of OpenFOAM solver on RANS simulations of round supersonic free jets". en. In: *Journal of Computational Science* 28 (Sept. 2018), pp. 18–31. ISSN: 18777503. DOI: 10.1016/j.jocs.2018.07.002. URL: https://linkinghub.elsevier.com/retrieve/pii/S1877750318303958 (visited on 01/27/2022).

[139] Junchao Zhang et al. "The PetscSF Scalable Communication Layer". In: *IEEE Transactions on Parallel and Distributed Systems* 33.4 (2022), pp. 842–853.

ECOLE DOCTORALE

Titre : Structures cohérentes dans des écoulements turbulents

Mots clés : Méthode résolvante, Instabilité, Modélisation linéaire, Jet, Turbulence, Fluides tournants

Résumé : Cette thèse s'intéresse à un formalisme récent, le formalisme résolvent, pour proposer une modélisation à ordre faible d'écoulements turbulents. Cette approche linéaire a un intérêt académique en permettant une meilleure compréhension des mécanismes concernés, mais aussi pour l'industrie en permettant des cycles de recherche et développement moins coûteux en calcul. Les travaux réalisés incluent une approche résolvante enrichie du tenseur de Reynolds appliquée dans le cas de l'écoulement canal, et une étude en profondeur du comportement d'un jet turbulent en rotation. Purement numérique, cette contribution s'appuie sur la méthode éléments finis et le formalisme Reynolds-Averaged-Navier-Stokes. Parmi les résultats obtenus, on notera la découverte de nouveaux comportements des jets à basse fréquence ainsi que leur interprétation. Certains de ces effets ne sont pas à portée des méthodes précédemment employées.

Title : Coherent structures in turbulent flows

Keywords : Resolvant method, Instability, Linear modelling, Jet, Turbulence, Swirling fluids

Abstract : This thesis is focused on a recent formalism called resolvent formalism, in order to put forward a low rank model of turbulent flows. This linear approach is of interest from an academical perspective as a way to better understand the mechanisms at play, as well as from an industry perspective by allowing for cheaper development cycles. Works detailed in this thesis include a resolvent approach enriched by the Reynolds stress tensor applied in the channel flow case, and an in depth study of a swirling turbulent jet. Based on purely numerical endeavours, this contribution is making ample use of finite element methods and Reynolds-Averaged–Navier-Stokes formalism. Amongst the obtained results, new jet behaviours at low frequency were brought to light as well as interpreted. Some of these effects are simply out of reach of traditional linear analysis methods.

Institut Polytechnique de Paris
91120 Palaiseau, France